SISSA
Scuola
Internazionale
Superiore di
Studi Avanzati

Physics Area – PhD course in

Theory and Numerical Simulation of Condensed Matter

# Markov State Modeling of 2D Nanofrictional Sliding, on Smooth and Rough Surfaces

*Thesis submitted for the degree of Philosophiæ Doctor.*

Candidate:

Martina Teruzzi

Advisor:

Giuseppe Santoro

Co-advisors:

Erio Tosatti

Alessandro Laio

Academic Year 2018-19

*Alla mia famiglia*

# Contents

# Introduction

Friction is a well-known and studied phenomenon, that takes place across many different scales. Besides everyone's daily life, it is of great concern to both pure and applied sciences, as well as to many technological problems like adhesion, lubrication, wear and many others. Due to continuing device miniaturization, friction imposes serious constraints and limitations on the performance and lifetime of advanced technological microdevices.
Although significant progress in understanding some factors that determine the response of confined system under shear has been achieved during the last decades, and much historical and recent insight obtained into the basic mechanisms that control tribological phenomena, a fundamental and thermodinamically based theoretical description of friction is still lacking.

The idea of modeling the sliding between two surfaces dates back to the 30s [8, 27, 44], with the renowned Prandtl-Tomlinson and Frenkel-Kontorova models. On the experimental side, interfacial phenomena have developed over the last two decades thanks to the advent of new meso- and nano-scale instruments like Surface Force Apparatus (SFA) [23], Atomic Force Microscope (AFM) or Quartz Crystal Microbalance (QCM) [4, 22, 28]. Finally, the development of modern computers has lead the way to a rich variety of non-equilibrium Molecular Dynamics (MD) simulations [18,33].

Despite these studies from several perspectives, friction still lacks a general theory or approach, mainly due to the complexity in identifying few relevant variables for the frictional dynamics, among a macroscopic number of degrees of freedom, suitable for the description of the main slow modes of the system.
The main goal of the following PhD research project is to try to fill this gap using statistically based techniques developed in the fields of data science and biomolecular simulations, like clustering algorithms and Markov State Modeling, here extended to non-equilibrium phenomena. Their combined effect is to reduce the dimensionality of the system, by singling out a few, slow, and most relevant time scales and the observables that best describe them.
The method we have developed comprises three main steps: a long atomistic Molecular Dynamics (MD) simulation of steady-state frictional sliding, a dimensional reduction [14, 46, 47] and finally an analysis of the time scales that underlie the transitions between the main events.
To develop the new method, systems of increasing complexity were successfully considered, from a 1D model [38, 50] to a realistic three-dimensional (3D) system of an island of graphene sliding on a rough substrate of gold.

# Chapter 1

# Theoretical background

In this chapter we are going to give a description of the main features of Nanotribology. This science is devoted to the study of friction at meso- and nano-scale. A lot of efforts have been made both on the experimental and on the computational side in the last decades, to analyze a lot of different phenomena, including adhesion, lubrication, wear, contact formation and many others [52, 54]. Moreover, remarkable development in nanotechnology and in computing hardware has provided the possibility to study tribological processes, supplying very detailed information on the atomic scale for realistic interfaces.
In the following, we are going to give a brief presentation of the two main minimalistic models describing friction: the Prandtl-Tomlinson model [8, 44] and the Frenkel-Kontorova model [27]. Even such essential toys will make the reader able to appreciate the key aspects of tribology at the nanoscale.
The last part will be instead devoted to the introduction of sliding on rough surfaces and to the description of the realistic model of a circular-shaped island of graphene sliding on a rough substrate of gold that has been the subject of our final study.

## 1.1 Friction models

### 1.1.1 Prandtl-Tomlinson model

The Prandtl-Tomlinson model [8, 44] is the simplest model of friction able to address all the problems of nanoscale tribology. Moreover, it captures the core of Friction Force Microscopy (FFM), where friction forces are measured by dragging an AFM tip along a surface.
The Prandtl-Tomlinson model is constituted by a mass $m$, mimicking the AFM tip, sliding over a sinusoidal potential, which plays instead the role of the crystalline substrate, like in Figure 1.1. The point tip is pulled by a spring of constant $K$, extending between the mass and the microscope support stage, that is driven with a constant velocity $v$ relative to the substrate. The total potential experienced by the tip is the following:

$$U(x,t) = -U_0 \cos\left(\frac{2\pi}{a}x\right) + \frac{K}{2}(x - vt)^2 \,, \tag{1.1}$$

where $U_0$ is the amplitude of the potential, $a$ its periodicity. The instantaneous lateral friction measured in experiments is $F_L = -K(x - vt)$, and the kinetic friction $F_k$ is the time average of $F$. The tip is localized in the first position $x = x_{tip}$ where the first derivative of $U(x,t)$ with respect to $x$ is zero [13]:

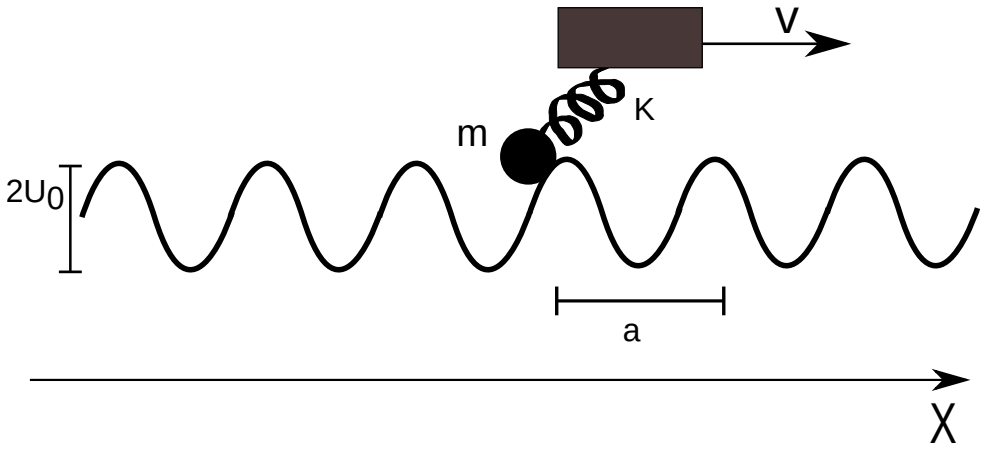


Figure 1.1: Prandtl-Tomlinson model.

$$\frac{\partial U(x,t)}{\partial x} = \frac{2\pi U_0}{a} \sin\left(\frac{2\pi}{a} x_{tip}\right) + K(x_{tip} - vt) = 0 \,. \tag{1.2}$$

Expanding the sinusoidal term to the first order in Equation 1.2, we obtain the initial velocity of the tip: $v_{tip}(0) = \frac{dx_{tip}}{dt}|_{t\to 0} = v/(1+\eta)$, where we have introduced the dimensionless parameter $\eta = 4\pi^2 U_0/(Ka^2)$, which represents the ratio between the stiffnesses of the tip-substrate potential and the pulling spring.
Figure 1.2 shows a numerical solution of Equation 1.2, where $x_{tip} = x_{min}(t)$ is represented as a function of time $t$. The time dependence of the first local maximum of $U(x,t)$, $x_{max}(t)$, is also shown in the figure. The first-order expansion we have used remains valid as far as the tip velocity does not change significantly. At a certain time, however, the tip velocity increases sharply, and a critical value $x_c$ is reached, where $x_{tip} = x_{max}$, the equilibrium is lost, and the tip suddenly jumps out of equilibrium. When $x_{min} \to x_c$ the velocity of the tip tends to infinite.
The critical position $x_{tip} = x_c$ is obtained from the condition that the second derivative of the total potential $U(x,t)$ with respect to $x$ is zero:

$$\frac{\partial^2 U(x,t)}{\partial x^2} = -\frac{4\pi^2 U_0}{a^2} \cos\left(\frac{2\pi}{a} x_c\right) + K = 0 \,, \tag{1.3}$$

which gives as a result $x_c = a \cdot \arccos(-1/\eta)/2\pi$. The absolute value of the lateral force revealed by the AFM at the critical position $F_c$ is obtained from Equations 1.2 and Equation 1.3:

$$F_c = \frac{Ka}{2\pi}\sqrt{\eta^2 - 1} \,. \tag{1.4}$$

When $\eta < 1$, the total potential $U(x)$ exhibits only one minimum and the time-dependent sliding motion is smooth; for $\eta > 1$, two or more minima appear in $U(x)$, and the sliding is discontinuous, characterized by stick-slip transitions; the value $\eta = 1$ represents the transition from smooth sliding to slips by one lattice site (single-slip regime), see Figure 1.3.
In experiments, the effective value of the PT parameter $\eta$ can be controlled by the variation of the normal load on the contact, which changes the corrugation of the potential.
The energy amount $\Delta U = |\Delta F_L| \cdot a$ released in each tip jump can be evaluated numerically as a function of the friction parameter $\eta$ (see Figure 1.4). If $\eta < 1$, i.e. when the contact is stiff or

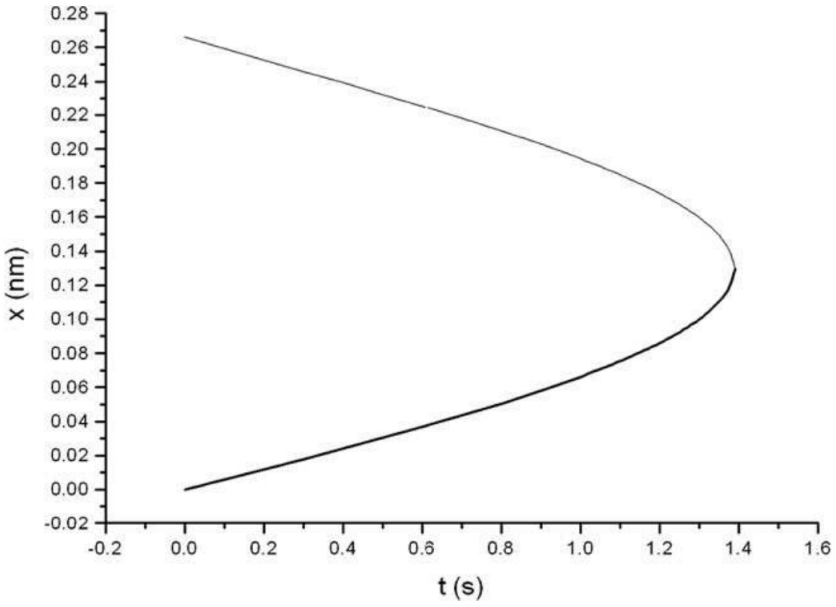


Figure 1.2: First minimum (thicker line) and maximum (thinner line) of the potential $U(x,t)$ as a function of time, Prandtl-Tomlinson model. From [13].

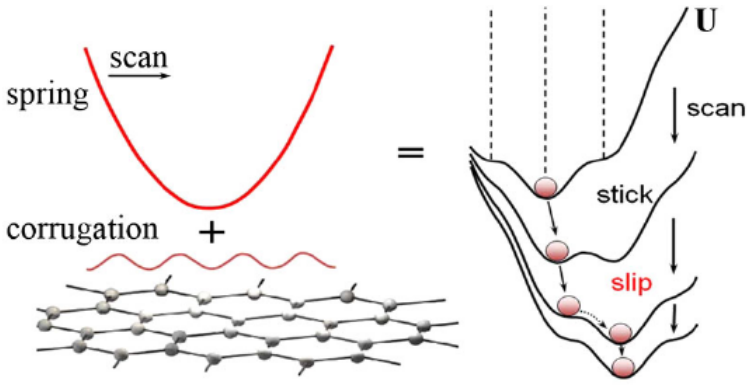


Figure 1.3: Prandtl-Tomlinson model: different stick-lip regimes. From [54].

the tip–sample interaction is very weak, the equations for the critic force and the critic position have no solutions. In such case, the instabilities are completely canceled, so that no abrupt release of energy occurs, and $\Delta U = 0$. In what follows, we will refer to this case as the superlubric regime. Figure 1.4 shows that the transition from stick-slip to superlubricity is smooth, i.e. the energy dissipation vanishes when $\eta \to 1$ without abrupt variations. In this sense, we can say that the friction parameter $\eta$ behaves like an order parameter in a second-order phase transition. The relation between $\Delta U$ and $\eta$ can be analytically evaluated only in the extreme cases $\eta \to 1$ and $\eta \to \infty$, where the dependencies $\Delta U \sim U_0(\eta - 1)^2$ and $\Delta U \sim U_0$ respectively hold.

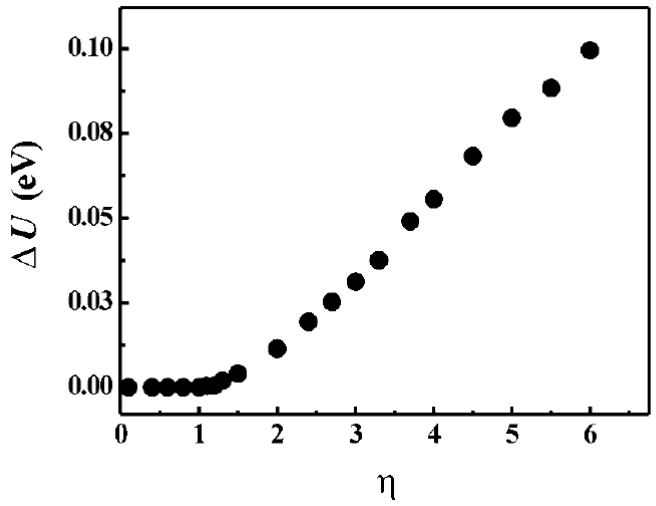


Figure 1.4: Prandtl-Tomlinson model: energy dissipation per cycle as a function of the frictional parameter $\eta$. From [44].

The main aspect of thermal effects on friction were considered in the pioneering work by Prandtl [44]. Thermal effects can be incorporated into the model in Equation 1.1 by adding a thermal random force $\hat{f}(t)$ to the conservative force between the slider and substrate and the damping term $-m\gamma\dot{x}$. Then the tip motion is described by the following Langevin equation:

$$m\ddot{x} + m\gamma\dot{x} = -\frac{\partial U(x,t)}{\partial x} + \hat{f}(t) \; . \tag{1.5}$$

The random force should satisfy the fluctuation-dissipation theorem; it has been chosen with zero mean $\langle\hat{f}(t)\rangle = 0$ and $\delta$ correlated, $\langle\hat{f}(t)\hat{f}(t')\rangle = 2m\gamma k_B T\delta(t-t')$, where $k_B$ denotes the Boltzmann constant and $T$ is the temperature. The random forces and the damping term arise from interactions with phonons and/or other fast excitations that are not treated explicitly. In the thermal Prandtl-Tomlinson model, beside the parameter $\eta$, thermal fluctuations bring out a new dimensionless parameter $\Delta$ representing the ratio between the pulling rate $v/a$ and the characteristic rate of thermally activated jumps over the potential barriers, $\omega_0 \exp(-U_0/k_B T)$, where $\omega_0$ is the attempt frequency. As a result, one should distinguish between two regimes of motion: $\Delta \ll 1$, the regime of very low velocities or high temperatures (typically $v < 1$ nm/s at room temperature), where the tip has enough time to jump back and forth across the barrier, and $\Delta \gg 1$, the stick-slip regime of motion, where thermal fluctuations only occasionally assist the tip to cross the barrier before the elastic instability is reached.
Several generalizations of the original one-dimensional PT model have marked new steps towards

understanding and implementation of frictional phenomena, considering the two-dimensional structure of surfaces, coupling between normal and lateral motion of the slider, etc.

### 1.1.2 1D Frenkel-Kontorova model

The second model we present is the simplest one that takes into account particle-particle interaction: the Frenkel-Kontorova (FK) model [27] in one-dimension. We refer to [54] for the parameters of the model. The standard FK model Hamiltonian is:

$$H(t) = \sum_i \left[ \frac{p_i^2}{2m} + \frac{K}{2}(x_{i+1} - x_i - a_c)^2 + \frac{U_0}{2}\cos\left(\frac{2\pi x_i}{a_b}\right) + \frac{\kappa}{2}(x_i - v_{drag} \cdot t)^2 \right] . \tag{1.6}$$

It consists of a chain of particles linked with springs of constant $K$, subject to a constant periodic potential of magnitude $U_0$. The chain is dragged with a constant velocity $v_{drag}$ applied to the whole chain or to the center of mass, thanks to a set of springs (or one spring) of constant $\kappa$. The two main lengths of the system, the springs equilibrium distance $a_c$ and the substrate periodicity $a_b$, can coincide or be mismatched. In the first case the FK model is named commensurate, incommensurate otherwise (see Figure 1.5).

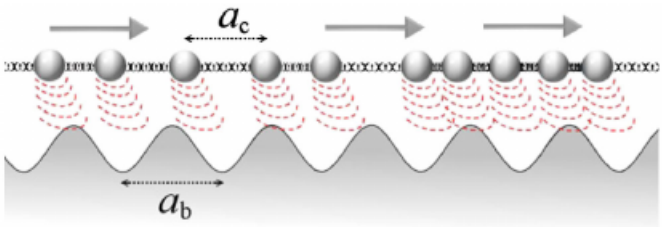


Figure 1.5: Sketch of 1D Frenkel-Kontorova. From [54].

The first term in Equation 1.6 is the kinetic energy of the chain, the second one describes the harmonic interaction of the nearest neighbors in the chain, and the last term is the interaction of the chain particles with the periodic potential. Static friction is probed driving all atoms with an extra adiabatically increasing force until sliding initiates.
Tribological processes in the FK model are ruled by kink (topological soliton) excitations. Consider the simplest case of the trivial commensurate ground state when the number of atoms $N$ coincides with the number of minima of the substrate potential $M$, so that the dimensionless concentration $\Theta = N/M = a_b/a_c = 1$. In this case, adding (or subtracting) one extra atom results in a chain configuration with a kink (or an antikink) excitation. After relaxation, the minimum energy configuration corresponds to a local compression (or extension in the antikink case) of the chain. Kinks are important because they move along the chain far more easily than atoms: the activation energy for kink motion (the Peierls-Nabarro barrier) is always smaller or much smaller than the amplitude $U_0$ of the substrate potential. Because the kinks (antikinks) correspond to extra atoms (vacancies), their motion provides a mechanism for mass transport along the chain and are thus responsible for mobility, conductivity, and diffusivity. Moreover, a kink (antikink) can be more or less localized, depending on the stiffness of the springs and on the corrugation of the potential. The

more a kink is delocalized, the smaller is its Peierls.Nabarro barrier, and the larger its mobility. For a fixed type of kink (antikink) excitation, the higher the concentration of kinks, the higher will be the system mobility [53]. When the ground state is commensurate (i.e., $\Theta = 1$), at non-zero temperature, the first step to initiate motion in the FK model is the creation of a kink-antikink pair. When the chain is of finite extension, kinks are usually generated at one end of the chain and then propagate along the chain until disappearing at the other free end. Each run of the kink (antikink) through the chain results in the shift of the whole chain of one lattice constant $a_b$. In the case of a finite film confined between two solids, one may similarly expect that the onset of sliding is initiated by the creation of local compression (kink) at the boundary of the contact, while kink motion is the basic mechanism of sliding.
Let the substrate period $a_b$ and the natural period of the chain $a_c$ be such that their ratio $\Theta = a_b/a_c$ is irrational. Roughly speaking, in this case the FK chain acquires a 'staircase' deformation, with regions of approximate commensurability separated by regularly spaced kinks (or antikinks in $\Theta < 1$). If there is a nonzero probability to find particles arbitrarily close to the maximum potential energy $U_0$, these kinks are unpinned and mobile, otherwise they are pinned. For a fixed amplitude of the substrate potential $U_0$, the FK undergoes a transition (called the *Aubry transition*, [42]) at a critical value $K = K_c$ of the chain stiffness. $K_c$ depends dramatically and discontinuously on the incommensurability ratio $a_b/a_c$ defining the interface. In particular, it has been proven [6] that $K_c$ takes the minimal possible value given by $K_c \sim 1.029$ (in units of $2U_0(\pi/a_b)^2$) for the ratio equal to the golden mean $a_b/a_c = (1+\sqrt{5})/2$. From a physical point of view, this means that for $K > K_c$ there is a continuum set of ground states that can be reached adiabatically by the chain through non-rigid displacements of its atoms at no energy cost. On the other hand, for $K < K_c$, the atoms are all trapped close to the minima of the substrate potential and thus require a finite energy per kink (equal to the Peierls-Nabarro barrier) to move over the corrugated substrate. Thus, for the incommensurate contacts above the Aubry transition ($K > K_c$) the kinks are mobile, chain sliding is initiated by even the smallest driving force, and, accordingly, the static friction force vanishes; the chain is defined *superlubric*. On the other hand, below $K_c$ the two incommensurate 1D surfaces are locked together due to the pinning of the kinks that separate local regions of common periodicity, and in this case we expect stick-slip motion. Note that a finite-size $T = 0$ FK model is always statically pinned, even for an irrational value of $a_b/a_c$ because of the locking of the free ends of the chain. At finite temperature, pinning can be overcome by thermal fluctuations, which can initiate sliding even in the most-pinned state, the fully commensurate one.

### 1.1.3 2D Frenkel-Kontorova model

In our work we have also focused on the two-dimensional version of FK model, in particular on the incommensurate case. The system is an hexagonal-shaped slider composed of $N = 1027$ particles displaced on a triangular lattice as shown in Figure 1.6, 19 for each side. The particles are coupled by nearest neighbor springs of constant $K$.
The center of mass is coupled by a spring of constant $\kappa$ to a dummy tip which drags it with constant velocity $v_{ext}$, so that the full Hamiltonian reads:

$$H(t) = \sum_i \left[ \frac{\mathbf{p}_i^2}{2m} + \frac{K}{2}(\mathbf{r}_{i+1} - \mathbf{r}_i - a_H)^2 + V(\mathbf{r}_i) + \frac{\kappa}{2}(x_{CM} - v_{ext} \cdot t)^2 \right] , \tag{1.7}$$

where $\mathbf{r} = (x, y)$ and the potential $V(\mathbf{r})$ has the following form:

$$V(x,y) = U_0 \left[ 2\cos\left(\frac{2\pi}{a_S}x\right)\cos\left(\frac{2\pi}{a_S}\frac{y}{\sqrt{3}}\right) + \cos\left(\frac{4\pi}{a_S}\frac{y}{\sqrt{3}}\right) \right] . \tag{1.8}$$

The two main lengths of the system are slightly incommensurate, with ratio $\theta = a_S/a_H \simeq 1.07$.

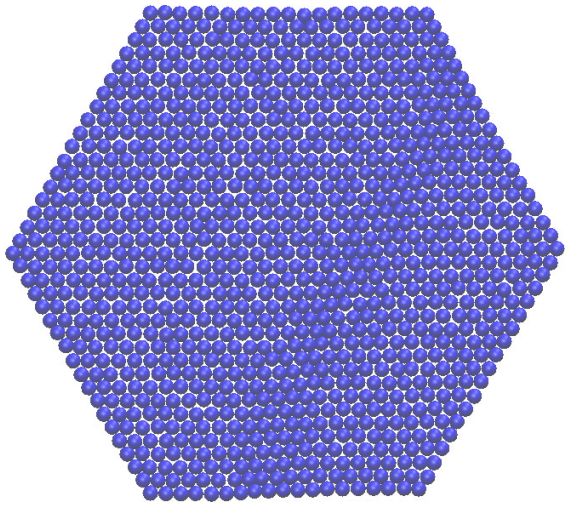

Figure 1.6: 2D Frenkel Kontorova: hexagonal island.

## 1.2 Sliding on rough substrates

The last part of this PhD project has been focused on studying the sliding of a circular island of graphene on a rough substrate of gold. Why a rough substrate? Even a surface which appears to be flat at a millimeter scale may contain micrometer scale asperities i.e., the surface is rough. If we bring two surfaces in contact, only these asperities really touch each other. Friction and energy dissipation are due to the interaction between the asperities of the different surfaces.

### 1.2.1 The old school: phenomenological laws

Contact and rubbing between surfaces, because of its enormous practical and technological importance, has stimulated progress all over the centuries [54]. A lot of historical figures have started to analyze it as a physical problem, formulating pioneering phenomenological laws. According to Da Vinci, Amonton, Desaguliers, Euler's and Coulomb's early studies, friction is:

- proportional to the normal load
- independent from the apparent area of contact
- independent from the sliding velocity

However, due to surfaces generally rough nature, the real area of contact is orders of magnitude smaller than the apparent area of contact [35], as sketched in Figure 1.7(top). Moreover, the contact area varies when a non-zero load is applied (Figure 1.7, bottom).

### 1.2.2 Real vs. apparent area of contact: Bowden and Tabor (1950)

Tribology, after centuries of research, had to wait for the milestone work of Bowden and Tabor in 1950 [5] in order to improve the phenomenological description of sliding on rough substrates. In fact, Bowden and Tabor produced a collection of facts and models on friction and lubrication that has become the standard on friction and lubrication for a couple of decades. Their adhesion model for friction at the micrometer scale, or plastic junction model, assumes that friction is proportional

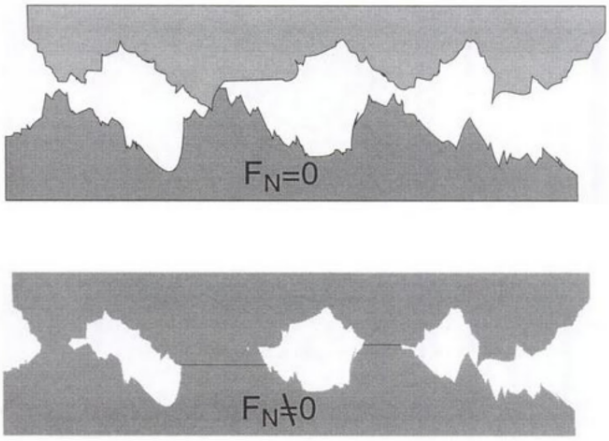


Figure 1.7: Real vs. apparent contact area. The length scale of interest depends on the normal load acting between the surfaces. A real contact area cannot be defined for zero load (top), whereas for finite normal force small asperities are destroyed (bottom). From [35].

to both the *real* area of contact and a mean lateral force per unit area, the so-called shear strength: $F_{frict} = \sigma A_R$, where $A_R$ denotes the real area of contact and $\sigma$ is the shear strength. Friction is proportional to the real area of contact as is connected to adhesion, and energy loss in the friction mechanism is described as plastic deformation of the asperities. The understanding of friction at the micrometer scale has been reduced to an understanding of two new quantities: shear strength and area of contact, which is considered to be intrinsically rough.
The shear strength is a material constant, and $\sigma$ is assumed experimentally to be independent from the applied load $F_N$. When one neglects any dependence of $\sigma$ on the normal force, the resulting experimental problem is to measure the real area of contact as a function of the applied load. This quantity depends on the length scale considered: at every different resolution the surface will show different kinds of roughness, down to the atomic level. The situation is again different if a finite normal force $F_N$ is acting on the asperities. Due to the material elasticity, all structures on a length scale which is smaller than a typical length $R_{typical} = \sqrt{DF_N}$ are destroyed, due to deformation. According to Hertz, in fact, the radius $a$ of a contact area for a perfectly spherical asperity of radius $R$ is $a = (DRF_N)^{1/3}$. The condition $a = R$ leads then to $R_{typical} = \sqrt{DF_N}$. Here, $D$ is a quantity that relates the elastic moduli and Poisson's numbers of both the sphere and the plane. The hypothesis is that, when the contact radius of an asperity is larger than the asperity itself, it is elastically destroyed. This concept will be more clear after the description of the Hertzian model, which will be discussed in more detail below.

### 1.2.3 Single asperity contact

It is convenient to start our considerations on the real area of contact by analyzing the case of a single asperity. The main distinction is between plastic and elastic point contacts.
In Bowden and Tabor's model, the deformation of the surface asperities is assumed to be totally plastic. Because of this, the area of contact is inversely proportional to the yield pressure $p_m$ of the asperity. Therefore, $A_R$ is independent from the geometrical area of contact and proportional to the normal load. Having considered the shear strength $\sigma$ as a constant, the friction force $F_{frict}$ is then proportional to the load, like in Amonton's law. However, it is unlikely that friction is

totally plastic.
The opposite argument is the one of Hertz [21], which considers the contact between surfaces as purely elastic. The demonstration of Hertz based on the contact between two spheres of radii $R$ and $R'$, as shown in Figure 1.8.

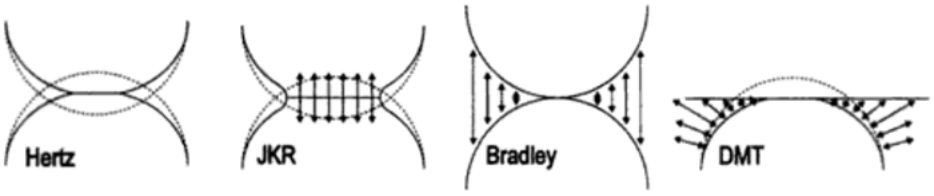


Figure 1.8: Single asperity contacts for different models: Hertzian, JKR, Bradley and DMT. From [35].

For symmetry reasons, the area of contact between the sphere and the plane is a circle and its area is:

$$A_R = \pi(DR)^{2/3}{F_N}^{2/3} \,, \tag{1.9}$$

where $R$ is the radius of the sphere, $D$ is a quantity that relates the elastic moduli and Poisson's numbers of both the sphere and the plane. Note that the result $A_R \propto {F_N}^{2/3}$ in Equation 1.9 is important: assuming that the shear strength $\sigma$ is independent from the load, then $F_L \propto {F_N}^{2/3}$, which is in contradiction with Amonton's law.
A further generalization of the single asperity contact is described in the work of Johnson *et al.* [24], extending the Hertzian model with the inclusion of adhesion. The real area of contact is described by Equation 1.10:

$$A(F_N) = \pi(DR)^{2/3}(F_N + 3\pi\gamma R + \sqrt{6\pi\gamma R F_N + (3\pi\gamma R)^2})^{2/3} \tag{1.10}$$

where $D$ and $R$ are the same symbols used in the previous equations. In the JKR model the real area of contact at zero load has the value $A(0) = \pi(6\pi D\gamma R^2)^{2/3}$, which means it has to be applied a negative load to break the contact. In the limit of zero surface tension $\gamma \to 0$, and also for large forces compared to $\gamma R$, the JKR result coincides asymptotically with the Hertzian result in Equation 1.9.
Experiments have been carried out to validate the models described up to now. The results show that for small load the JKR model fits the experimental data very well, whereas the Hertz model is not able to reproduce the observed contact diameters. However, for loads in the jump-off-contact regime also the JKR theory does not fit very well.
Some more models have been developed to describe the contact area between a plane and a sphere. The first one, by Bradley [30], considers only adhesion between two rigid spheres which are not allowed to deform. The second one, called DMT [10] model, assumes the deformation of the sphere to behave like Hertzian theory, with an additional adhesion between the whole sphere and the plane, whose effect goes beyond the contact area, contrary to the JKR model. Finally, in a more recent work by Maugis [34], a Dugdale piece-wise linear potential is used to model the separation energy of a single asperity contact. The Dugdale potential has a slope $\sigma_0$ for separations $d < h_0$ and is constant for $d > h_0$ (see Figure 1.9, top). The resulting interaction force is constant, with values $-\sigma_0$ for distances $d < h_0$, and vanishes for separations $d > h_0$ (Figure 1.9, bottom).

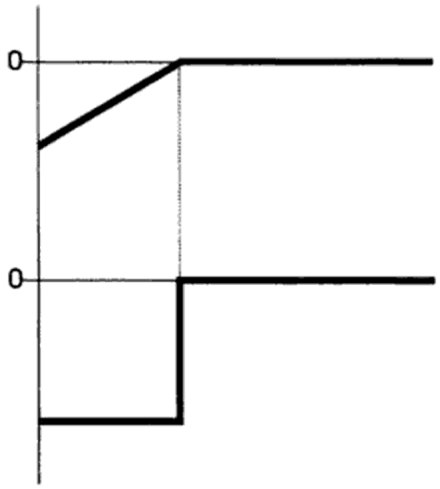


Figure 1.9: Schematics of the Dugdale model potential. Top: the potential shape. Bottom: the corresponding force law. From [35].

All the theories presented so far (Hertz, JKR, Bradley, DMT, Maugis) can be compared based on the following adimensional parameter $\lambda$:

$$\lambda = 2\sigma_0 \left( \frac{9R}{16\pi w (E^*)^2} \right)^{1/3}, \tag{1.11}$$

which is a measure of the magnitude of the elastic deformation at the point of separation compared to the range of surface forces. Thus, $\lambda$ is small for hard materials and is large for soft materials. In Equation 1.11, $\sigma_0$ denotes the depth of the potential well and $w = h_0\sigma_0$ is the adhesion energy. $R$ denotes the radius of the sphere and $E^* = 3/4D^{-1}$ is the combined elastic modulus.

### 1.2.4 Statistical ensemble of asperities: apparently flat surfaces

We will now extend the results obtained for a single asperity contact to a statistical ensemble of asperities.
The fully plastic contact can be described in a way similar to the one of a single asperity, as the condition that we have only one single asperity has never been used. Therefore, the result is the same as in Equation 1.9. For the elastic contact, the milestoning work of Greenwood and Williamson [17] (1966) has to be taken into account. They considered a surface with a random distribution of asperity heights, where every asperity has the same radius of curvature $\beta$ at the summit, which is pressed against a plane. The separation of the reference lines is denoted by $d$. If we consider the deformation of an asperity with height $z$, then $w = z - d$ is the "penetration depth" (see Figure 1.10).
Using Hertz theory of a totally elastic contact (see Equation. 1.9), we obtain the area of contact of this asperity:

$$A = \begin{cases} \pi\beta w \ \text{ if } x \geq 0 \\ 0 \ \text{ if } \ x \leq 0 \end{cases} . \tag{1.12}$$


Figure 1.10: The overlap of a rough surface with a geometrical plane. According to the Greenwood and Williamson theory the asperities above the plane are deformed elastically according to Hertzian theory (see [35]).

The load acting on the asperity after Hertz is $F_N = \frac{\beta^{1/2}}{D} w^{3/2}$, where $D$ is the inverse plane stress modulus discussed above. The probability that a given asperity has a height between $z$ and $z + dz$ will be $\Phi(z)dz$. The standard deviation of the height distribution is denoted $\sigma_0$. It can be proven that the real area of contact is:

$$\pi N \beta \int_d^\infty (z - d)\Phi(z)dz \; . \tag{1.13}$$

Note that the total number of asperities $N$ is proportional to the nominal contact area $N = \eta A_G$ and therefore $A_R \propto A_G$. In the same manner, from the expression of the load we find that the total load is:

$$F_N = \frac{N\beta^{1/2}}{D} \int_d^\infty (z - d)^{3/2}\Phi(z)dz \; . \tag{1.14}$$

If we take the simplest distribution for asperity heights, e.g. exponential ($\Phi(z) = e^{-d/\sigma}$), the integrals in Equation 1.13 and Equation 1.14 can be solved exactly, obtaining a real contact area proportional to the load, as known empirically. Moreover, the average size of contact spots is independent from the load. In fact, the size of any individual contact spot increases with load, but at the same time new, small spots are formed and there is a perfect balance which leaves the average unchanged. This leads to the conclusion that the proportionality between area and load lies in the statistics of surface roughness. In Figure 1.11, the relation between friction force and normal load for a Gaussian height distribution $\Phi(z) = e^{-z^2}$ is shown. This distribution is similar to the one obtained experimentally. This is valid just when the real contact area is much smaller than the macroscopic contact area.

The Greenwood-Williamson theory was a great success, since it was able to explain Amonton's law without the (unphysical) assumption that every deformation between the asperities is plastic. However, there are two parameters working as input to the theory which are not easy to measure. First, a well-defined number of asperities $N$ must be measured, which is a nearly impossible task to do. The height distribution turns out to be quite different for various materials and strongly dependent on the surface finish; however, an approximately Gaussian behavior is present in a lot of materials. The problem of correct counting and measuring asperities has been solved by Whitehouse and Archard in 1970 [57], using the concept of self-similarity, first introduced by

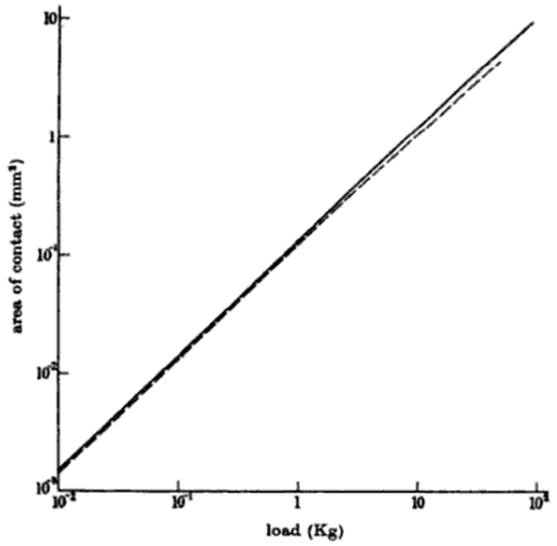


Figure 1.11: The relation between friction force and normal load within the Greenwood and Williamson model for a Gaussian height distribution $\Phi(z) = e^{-z^2}$. Amonton's law is recovered with a totally elastic approach (see [17]). This is valid just when the real contact area is much smaller than the macroscopic contact area.

Archard in its pioneering works [2, 3], where he was able to prove that for a certain self-similar surface structure, according to Hertz theory, the exponent $n$ in the relation $A_G \propto {F_L}^n$ goes to unity (see Figure 1.12).

### 1.2.5 Persson's theory (2001)

In this paragraph, we would like to describe a recent theory of contact mechanics, developed by Persson in 2001 [39], valid for randomly rough (e.g., self-affine fractal) surfaces (see Figure 1.13). Persson's theory is valid for both elastic and plastic deformation and, differently from Greenwood and Williamson's theory, it can be applied to surfaces with arbitrary surface roughness, without the need to define an average radius of curvature for the asperities. In fact, it turns out that the latter depends strongly on the resolution of the roughness-measuring instrument, or any other form of filtering, and hence is not unique.
The theory can be described as follows: consider a surface with surface roughness on two different length scales, as in Figure 1.14. Assume that a rubber block is squeezed against the substrate and that the applied pressure is large enough to squeeze the rubber into the large "cavities" of Figure 1.14. Even though the rubber is able to make direct contact with the substrate in the large cavities, the pressure acting on the rubber at the bottom of a large cavity will be much smaller than the pressure at the top of a large asperity. Thus, because of the high local pressure, the rubber may be squeezed into the "small" cavities at the top of a large asperity. However, the pressure at the bottom of a large cavity may be too small to squeeze the rubber into the small-sized cavities at the bottom of a large cavity.

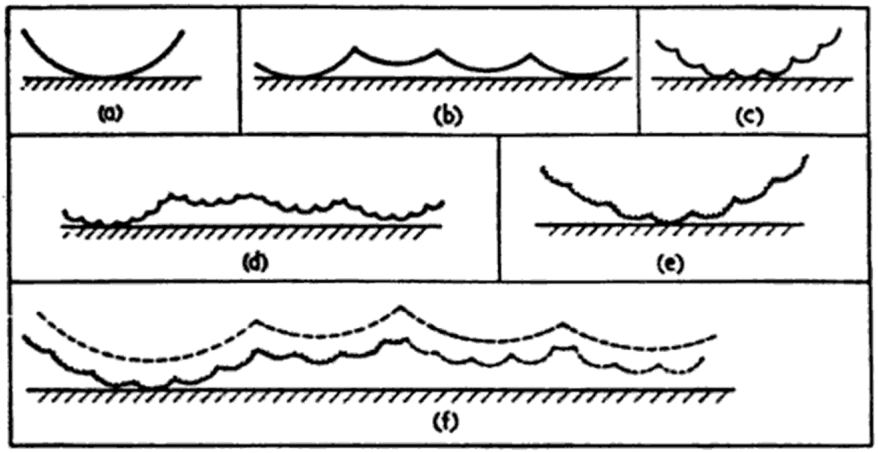


Figure 1.12: Models of surfaces containing asperities of different scales of size. When the deformation is elastic the relationships between area of contact $A$ and normal load $L$ converge to proportionality: a) $A \propto L^{2/3}$, b) $A \propto L^{4/5}$, c) $A \propto L^{8/9}$, d) $A \propto L^{14/15}$, e) $A \propto L^{26/27}$, f) $A \propto L^{44/45}$. From [35].

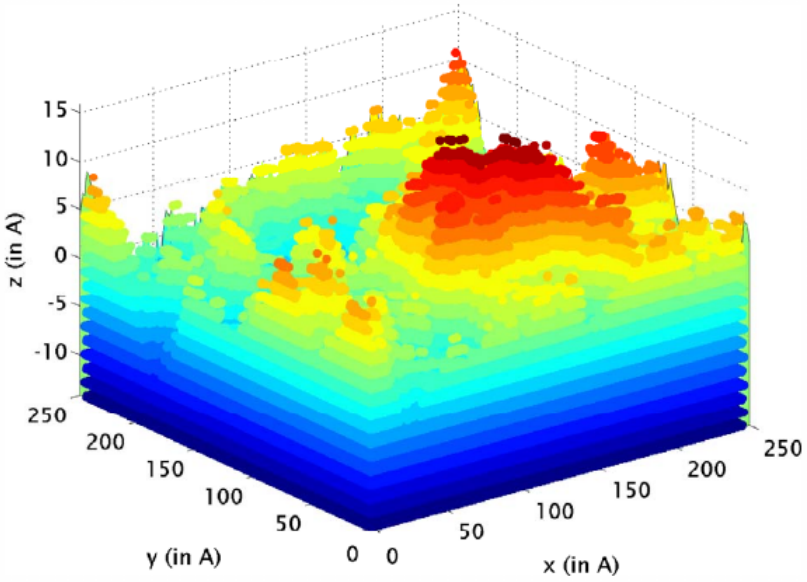


Figure 1.13: Self-affine fractal surface with Hurst exponent H=0.5. Credits: J. F. Molinari.

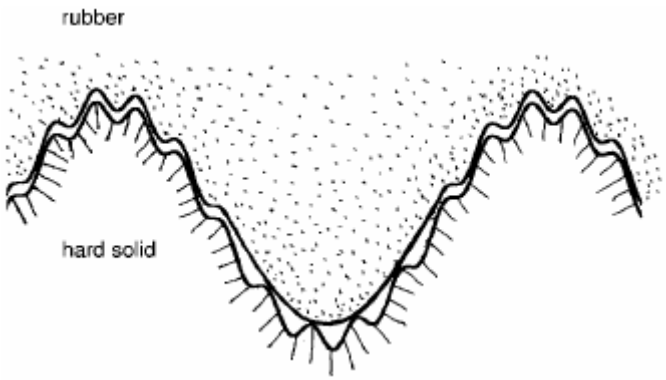


Figure 1.14: A rubber block squeezed against a substrate with roughness on two different length scales. The rubber is able to fill out the long-wavelength roughness profile, but it is not able to get squeezed into the small-sized "cavities" at the bottom of a big cavity. From [39].

Persson's theory focuses on the quantity $A(\lambda)/A(L)$, which is the relative fraction of the rubber surface area where contact occurs on the length scale $\lambda = L/\zeta$ (where $\zeta \geq 1$). $A(\lambda)$ is the (apparent) area of contact on the length scale $\lambda$ (more precisely, the area of real contact if the surface would be smooth on all length scales shorter than $\lambda$, see Figure 1.15), while $A(L) = A_0$ denotes the macroscopic contact area ($L$ is the diameter of the macroscopic contact area, so that $A_0 \approx L^2$).

It is known from contact mechanics that in the frictionless contacts of elastic solids with rough surfaces, the contact stresses depend upon the shape of the gap between them before loading. Thus, without loss of generality, the actual system can be replaced by a flat elastic surface in contact with a rigid body having a surface roughness profile which result in the same undeformed gap between the surfaces. By assuming complete contact between the rubber and the substrate on all length scales smaller than $\lambda$ [39], and expanding the stress distribution in the contact areas under the magnification $P(\sigma, \zeta + \Delta\zeta)$ (where $\sigma$ is the stress) to linear order in $\Delta\zeta$, assuming an average over regions in $\zeta$ as independent processes, the author obtains a diffusion-type equation for $P$:

$$\frac{\partial P}{\partial \zeta} = G'(\zeta){\sigma_0}^2 \frac{\partial^2 P}{\partial \sigma^2} \ , \tag{1.15}$$

where $G'(\zeta)$ is the derivative of the following function:

$$G(\zeta) = \frac{\pi}{4}\left[\frac{E}{(1-\nu^2)\sigma_0}\right]^2 \int_{q_L}^{\zeta q_L} dq q^3 C(q) \ , \tag{1.16}$$

and $C(q)$ is the surface roughness power spectra:

$$C(q) = \frac{1}{(2\pi)^2} \int d^2x \langle h(\mathbf{x}) h(\mathbf{0}) \rangle e^{-i\mathbf{qx}} \ , \tag{1.17}$$

where $z = h(\mathbf{x})$ is the height of the surface above a flat reference plane (such that $\langle h \rangle = 0$). Equation 1.15 is a diffusion-type equation where time is replaced by the magnification $\zeta$, and the spatial coordinate with the stress $\sigma$ (and where the "diffusion constant" depends on $\zeta$). Hence,

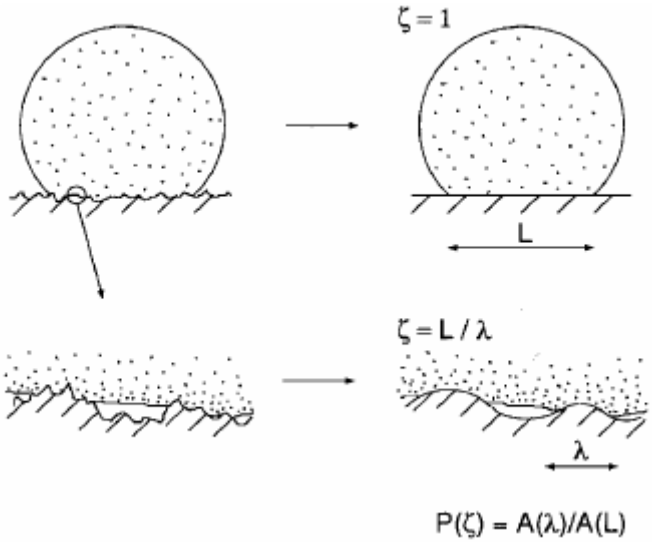


Figure 1.15: A rubber ball squeezed against a hard, rough, substrate. Left: the system at two different magnifications. Right: the area of contact $A(\lambda)$ on the length scale $\lambda$ is defined as the real area of contact when the surface roughness on shorter length scales than $\lambda$ has been removed (i.e., the surface has been "smoothed" on length scales smaller than $\lambda$). From [39].

focusing on $P(\sigma, \zeta)$ on shorter and shorter length scales (corresponding to increasing $\zeta$), $P(\sigma, \zeta)$ will become broader and broader in $\sigma$ space. Assuming that only elastic deformation occurs, and considering the limit $\sigma_0 \ll E$ (which means $G(\zeta) \gg 1$ for most values of $\zeta$), the author obtains $P(\zeta) \approx [\pi G(\zeta)]^{-1/2} \propto \sigma_0$, so that the area of real contact is proportional to the load.
A large number of surfaces of interest in tribology are self-affine fractal, with an upper cutoff length $\lambda_0 = 2\pi/q_0$ of the order of a few mm. As described in [39], for a self-affine fractal surface $C(q) = C_0$ for $q < q_0$, while for $q > q_0$ the following scaling relation holds:

$$C(q) = C_0 \left( \frac{q}{q_0} \right)^{-2(H+1)} , \tag{1.18}$$

where $H = 3 - D_f$ is the Hurst exponent, while $D_f$ is the fractal dimension of the surface. Using the scaling relation in Equation 1.18, the author obtains:

$$A(\lambda) = \frac{2L(1-\nu^2)}{\pi h_0} \left( \frac{1-H}{\pi \alpha H} \right)^{1/2} \frac{F_N}{E} \frac{\lambda}{L}^{1-H} , \tag{1.19}$$

so that, if $\lambda_1$ denotes the short-distance cutoff in the self-affine fractal distribution (which cannot be smaller than an atomic distance), then Equation 1.19 shows that the area of real contact $A(\lambda_1)$ is *proportional* to the load.
Persson's theory can be generalized to the case where also plastic deformation occurs simply by replacing the boundary condition $P(\sigma = \infty, \zeta) = 0$ with $P(\sigma_Y, \zeta) = 0$, which describes that plastic deformation occurs in the contact area when the local stress has reached $\sigma_Y$. In this case, the function $P(\zeta)$ can be divided in three different contributions: $P_{el}(\zeta) + P_{non}(\zeta) + P_{pl}(\zeta) = 1$, which describe the fraction of the original macrocontact area where, under the magnification $\zeta$, elastic, non-contact or contact with plastic yield has occurred, respectively.

### 1.2.6 The fractal dimension of rough surfaces

Most natural surfaces and surfaces of engineering interest are self-affine fractal over a wide range of length scales, sometimes extending from atomic dimensions to the linear size of the object under study. Surface roughness is of crucial importance in many engineering applications: for example, the surface roughness on a road surface influences the tire-road friction or grip. It is therefore of great interest to understand the nature of surface roughness in engineering applications. In another work by Persson [40], several examples are provided for the power spectra of different surfaces with self-affine fractal-like surface roughness; in particular, there are considered randomly rough surfaces where the statistical properties are transitionally invariant and isotropic. In this case, the 2D power spectrum defined as in Equation 1.17:

$$C(q) = \frac{1}{(2\pi)^2} \int d^2x \langle h(\mathbf{x})h(\mathbf{0})\rangle e^{-i\mathbf{qx}} \, , \tag{1.20}$$

will only depend on the magnitude of the wavevector $\mathbf{q}$. Here, $h(\mathbf{x})$ is the height coordinate at the point $\mathbf{x} = (x, y)$ and $\langle \ldots \rangle$ stands for ensemble averaging. From $C(q)$ (angular averaged power spectrum), many quantities of interest can be directly calculated. For example, the root-mean-square (rms) roughness amplitude can be written as:

$${h_{rms}}^2 = 2\pi \int_{q_0}^{q_1} dq q C(q) \, , \tag{1.21}$$

where $q_0$ and $q_1$ are the small and large wavevector cut-off. The rms slope $\kappa$ is determined by:

$$\kappa^2 = 2\pi \int_{q_0}^{q_1} dq q^3 C(q) \, . \tag{1.22}$$

For a self-affine fractal surface, as already stated in Equation 1.18, $C(q) \sim q^{-2(1+H)}$. Substituting this in Equation 1.21 gives:

$${h_{rms}}^2 = \frac{\pi C_0}{H} {q_0}^2 \left[ 1 - \left( \frac{q_1}{q_0} \right)^{-2H} \right] \, , \tag{1.23}$$

while for Equation 1.22:

$$\kappa^2 = \frac{\pi C_0}{1-H} {q_0}^4 \left[ \left( \frac{q_1}{q_0} \right)^{2(1-H)} - 1 \right] \, . \tag{1.24}$$

Usually, $q_0/q_1 \ll 1$ and since $0 < H < 1$, unless $H$ is very close to 0 or 1, we get:

$$\kappa = q_0 h_{rms} \left( \frac{H}{1-H} \right)^{1/2} \left( \frac{q_1}{q_0} \right)^{1-H} \, . \tag{1.25}$$

Many surfaces of engineering interest, e.g. a polished steel surface, have rms roughness of order $\sim 1$ $\mu$m when probed over a surface region of linear size $L = \pi/q_0 \sim 100$ $\mu$m. This gives $q_0 h_{rms} \approx 0.1$, and if the surface is self-affine fractal, the whole way down to the nanometer region (length scale $a$) then $q_1 = \pi/a \approx 10^{10}$ m$^{-1}$ and Equation 1.25 gives $\kappa \approx 0.1 \times 10^{5(1-H)}$. From the latter relation Persson shows that most surfaces of interest, if self-affine fractal from the macroscopic length scale to the nanometer region, cannot have a fractal dimension larger than $D_f \approx 2.3$ (or $H \approx 0.7$), as otherwise the average surface slope becomes huge, which is unlikely to be the case as the surface

would be very "fragile" and easily damaged (smoothened) by the mechanical interactions with external objects. In [40], Persson has calculated the 2D roughness spectra of several hundred surfaces of engineering interest. We report some examples in Figure 1.16. See the caption for more details.

Persson proposes also a simple model of sandblasting, showing that if one assumes that material removal is more likely at the top of asperities rather than in the valleys (see Figure 1.17), a surface with relatively low fractal dimension is naturally obtained.

In Persson's model for sandblasting, a beam of hard particles is sent on the surface orthogonal to the originally flat substrate surface, and with a laterally uniform probability distribution. The substrate is considered as a cubic lattice of blocks (or particles) and every particle from the incoming beam removes a randomly chosen surface block on the solid substrate. As shown in Figure 1.18, if an incoming particle impacts at site $(i, j)$ (at position $(x, y) = (i, j)a$, where $a$ is the lattice constant), then one of the blocks $(i, j), (i + 1, j), (i - 1, j), (i, j + 1)$ or $(i, j - 1)$ is removed. The author assumes either that the block that has the smallest number of nearest neighbors is removed (with probability 0.5), since this block is most weakly bound to the substrate, or the highest block is removed (with probability 0.5). In both cases, if several such blocks exist, the one to be removed is randomly chosen, unless the block $(i, j)$ is part of the set of blocks, in which case this block is removed.

Figure 1.19 shows the topography of a surface produced by the eroding process described above, after removing 76 290 layers of blocks. Figure 1.19 shows the surface roughness power spectrum as a function of the wavevector (on a $\log_{10}$-$\log_{10}$ scale). The surface is self-affine fractal with the Hurst exponent $H = 1$ (or fractal dimension $D_f = 2$), which has also been observed for sandblasted surfaces.

Finally, more results related to simulation of rough surfaces by erosion processes are presented. Consider first the most simple picture of sandblasting where a beam of hard particles is sent on the surface orthogonal to the originally flat substrate surface, and with a laterally uniform probability distribution. The substrate is again considered as a cubic lattice of blocks (or particles) , and every particle from the incoming beam removes a randomly chosen surface block on the solid substrate. This process will result in an extremely rough substrate surface with the Hurst exponent $H = -1$ and fractal dimension $D_f = 4$. This value of the fractal dimension may seem non natural, especially in a space that is 3D. A value of the Hurst exponent that is equal to $-1$ is also very unlikely in nature. The point, in this case, is that the power spectrum of the generated surface is independent of the wavevector. In fact, the author obtains $C(q) = C_0$ (a constant), and using the definition $C(q) \sim q^{-2(1+H)}$, this results in $H = -1$. In Figure 1.21 it is shown the power spectrum after removing 76 290, 19 070 and 2384 layers of blocks assuming process (a+b) as in Figure 1.20. For short time of sandblasting, a large roll-off region prevails which decreases toward zero as the sandblasting time increases. In Figure 1.22 the surface roughness power spectrum obtained using the random removal model is compared with the random removal with relaxation models like sand blasting (a) and lapping with sand paper (b), or the combined (a+b) after removing 19 070 layers of blocks. The models of random removal are shown in Figure 1.17.

The corresponding topography pictures for processes (a), (b) and (a+b) are shown in Figure 1.23. The random removal gives a constant power spectrum. The random removal with relaxation model (a) gives also unphysical surface topography with high sharp spikes. The (a+b) model gives results in agreement with experiments, which shows, as expected, that both removal (or smoothing) of high regions (asperity tops) and low coordinated surface volumes are important in sandblasting. Random removal results in an interface which is uncorrelated (see Figure 1.22). The columns shrink independently, as there is no mechanism that can generate correlations along the interface. The other erosion processes [(a), (b), (a+b)] all involve correlated removal of material, allowing the spread of correlation along the surface.

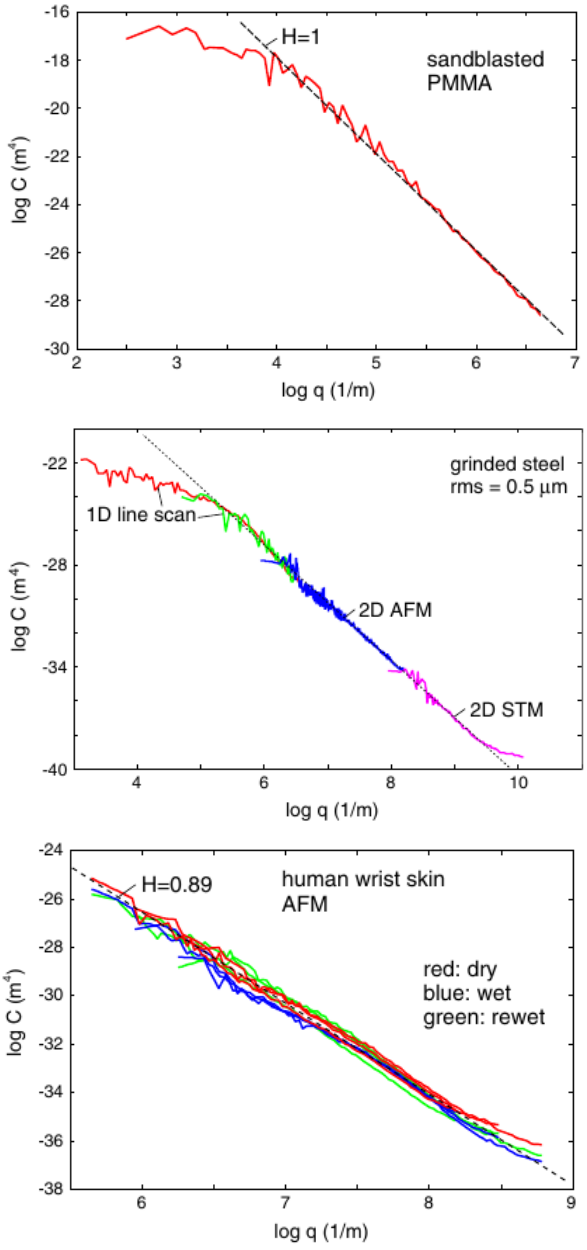


Figure 1.16: Some examples of 2D power spectrum for "natural" surfaces. From top to bottom, a sandblasted PMMA surface based on height profiles measured using 1D-stylus instrument (Hurst exponent $H = 1$ or fractal dimension $D_f = 2$), a grinded steel surface (Hurst exponent $H = 0.72$ or fractal dimension $D_f = 2.28$) and a human wrist skin surface analysis obtained from AFM measurements (Hurst exponent $H = 0.89$ or fractal dimension $D_f = 2.11$). All the Figures are in $\log_{10}$-$\log_{10}$ scale. From [40].

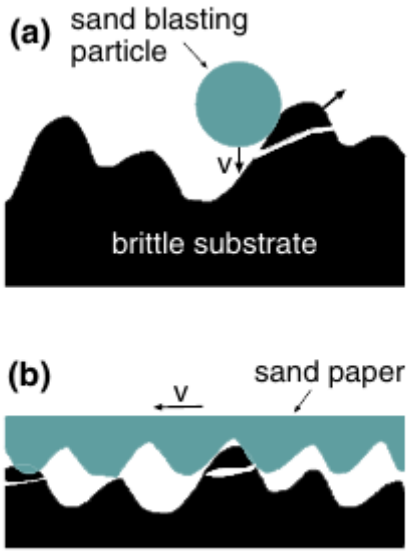


Figure 1.17: Sand blasting (a) and lapping with sand paper (b) will roughen an initially flat surface but in such a way that high and sharp asperities never form, i.e. the removal of material is easier at the top of the asperities than at the valley. This will result in a rough surface with low fractal dimension. From [40].

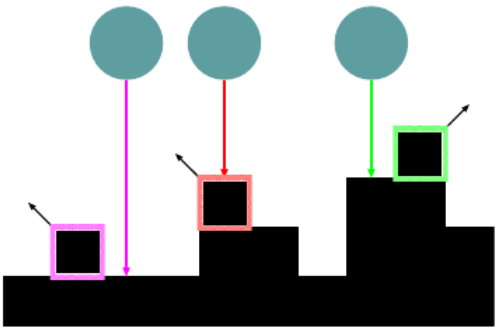

Figure 1.18: Incoming particles (colored arrows) and the blocks removed by the impact (black squares surrounded by colored rims) for a 1D version of the simulation model used. For the 2D model, if a particle impact at site $(i, j)$ (at position $(x, y) = (i, j)a$, where $a$ is the lattice constant), then one of the blocks $(i, j), (i + 1, j), (i - 1, j), (i, j + 1)$ or $(i, j - 1)$ is removed. Of these blocks, it is assumed either that the block that has the smallest number of nearest neighbors is removed (with probability 0.5), since this block is most weakly bound to the substrate, or the highest block is removed (with probability 0.5). In both cases, if several such blocks exist, the one to be removed is randomly chosen, unless the block $(i, j)$ is part of the set of blocks, in which case this block is removed. From [40].

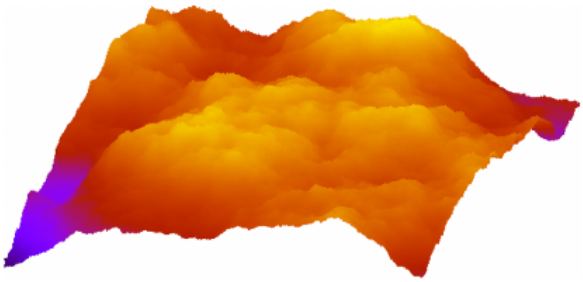

Figure 1.19: Topography picture of a surface produced by the eroding process described in Figure 1.18 after removing 76 290 layers of blocks. The surface plane consists of 2048x2048 blocks. The surface is self-affine fractal with the Hurst exponent $H = 1$ (or fractal dimension $D_f = 2$), see Figure 1.20. The width of the removed particles (or blocks) is $a = 0.1$ $\mu$m. The surface has the rms roughness $h_{rms} = 2.1$ $\mu$m and the rms slope $\kappa = 1.04$. From [40].

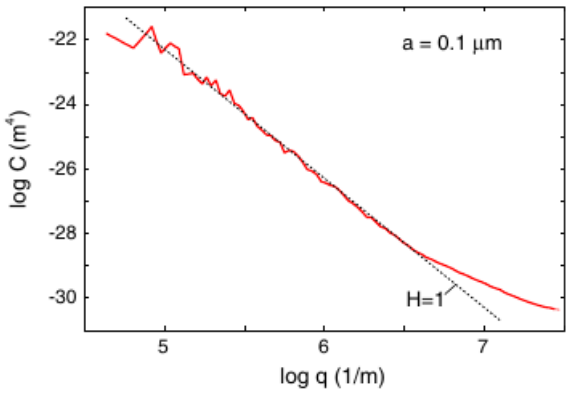


Figure 1.20: The surface roughness power spectrum as a function of wavevector, $\log_{10}$-$\log_{10}$ scale, after removing 76 290 layers of blocks (surface topography in Figure 1.19. The surface plane consists of 2048x2048 blocks. The surface is self-affine fractal with the Hurst exponent $H = 1$ (or fractal dimension $D_f = 2$). The linear size of the removed blocks has been assumed to be $a = 0.1$ $\mu$m. From [40].

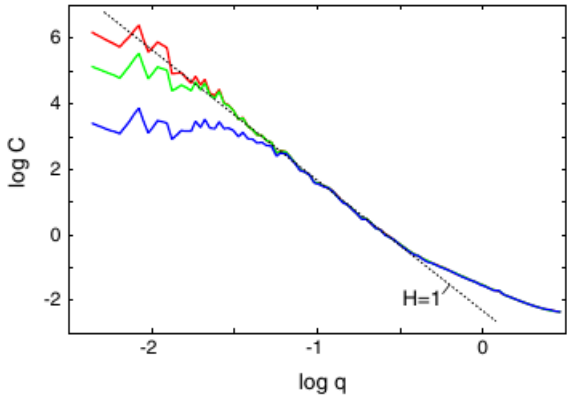


Figure 1.21: The surface roughness power spectrum as a function of wavevector, $\log_{10}$-$\log_{10}$ scale, for the erosion processes (a+b) (see Figure 1.17), after removing 2384 (*blue*), 19 070 (*green*) and 76 290 (*red*) layers of blocks. The wavevector is in units of $1/a$, and the power spectrum is in units of $a^4$. From [40].

i

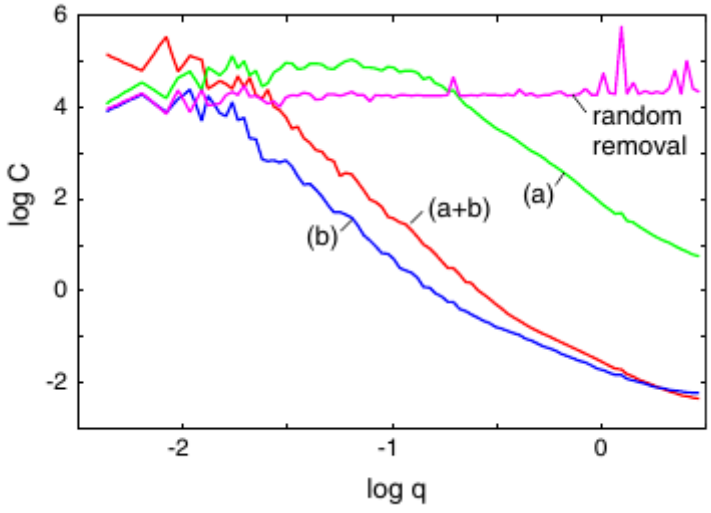


Figure 1.22: The surface roughness power spectrum as a function of wavevector, $\log_{10}$-$\log_{10}$ scale, for all the erosion processes considered, after removing 19 070 layers of blocks. The wavevector is in units of $1/a$, and the power spectrum is in units of $a^4$. From [40].

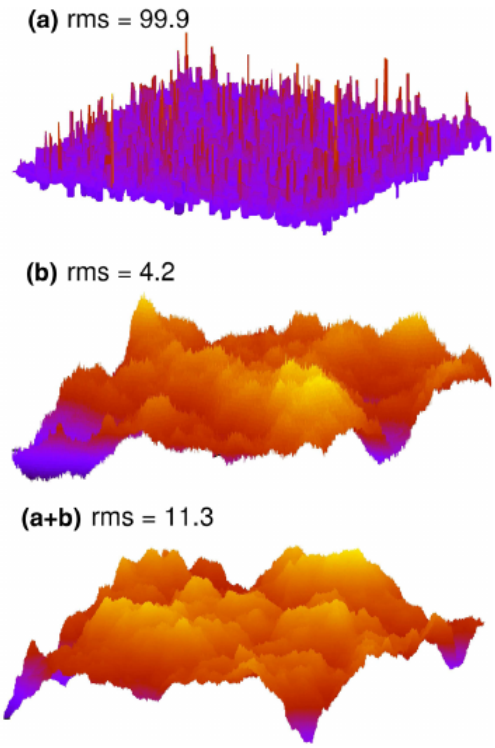


Figure 1.23: Topography picture of surfaces produced by the eroding processes (a), (b) and (a+b) after removing 19 070 layers of blocks. The surface plane consists of 2048x2048 blocks. The rms roughness values are in units of $a$. Random removal is not shown as it gives an extremely rough surface. From [40].

### The Contact-Mechanics challenge

Surfaces with a spectrum similar to the ones in [40] have been used in a contact-mechanics modeling challenge announced by Martin Muser [36], in 2017. The participants could rely on mathematical methods, simulations or experiments. We will not describe in details all the methodologies used and the results. Instead, we will briefly sketch the surface topography adopted in [36], as it is strictly related to the one studied in our realistic model simulation. The surface topography was produced by drawing random numbers for the Fourier transform of the height profiles $\tilde{h}(\mathbf{q})$ having a mean of zero and, on average, a second moment defined by the height spectrum:

$$C(q) \equiv \langle |\tilde{h}(\mathbf{q})|^2 \rangle = C(q_r) \times \begin{cases} 1 \text{ for } \lambda_r < 2\pi/q \leq \mathcal{L} \\ (q/r_r)^{-2(1+H)} \text{ for } \lambda_s \leq 2\pi/q < \lambda_r \\ 0 \text{ else} \end{cases} . \tag{1.26}$$

Here, $\mathcal{L} = 0.1$ mm is the linear dimension in $x$ and $y$ of the periodically simulated cell, $\lambda_r = 20$ $\mu$m is the roll-off wavelength, $q_r = 2\pi/\lambda_r$ and $\lambda_s = 0.1$ $\mu$m is the short wavelength cutoff, below which no roughness is considered. $H = 0.8$ is the Hurst roughness exponent. $\langle \ldots \rangle$ in Equation 1.26 denotes an average over different, random-surface realizations, or, alternatively, a local running average of the real spectrum. A graph showing the spectrum is presented in Figure 1.24. The features of the spectrum are similar to those found experimentally for a wide variety of surfaces (as in Reference [40]). The resulting surface topography arising from the spectrum is depicted in Figure 1.25.

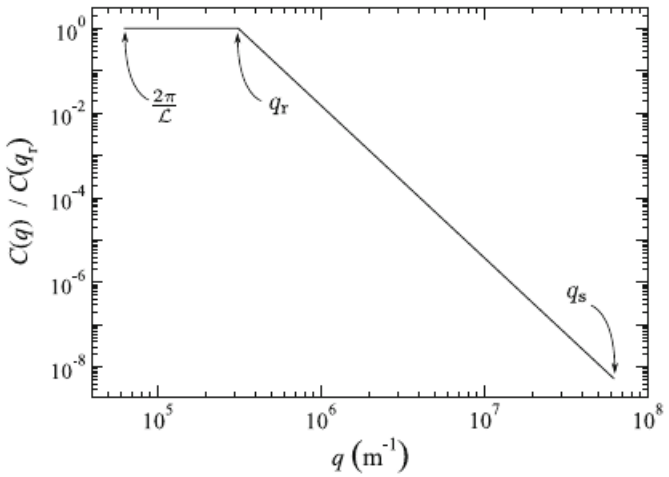


Figure 1.24: Height spectrum $C(q)$ from which the height distribution is drawn. It is normalized to its value at the roll-off wave number $q_r$. From [36].

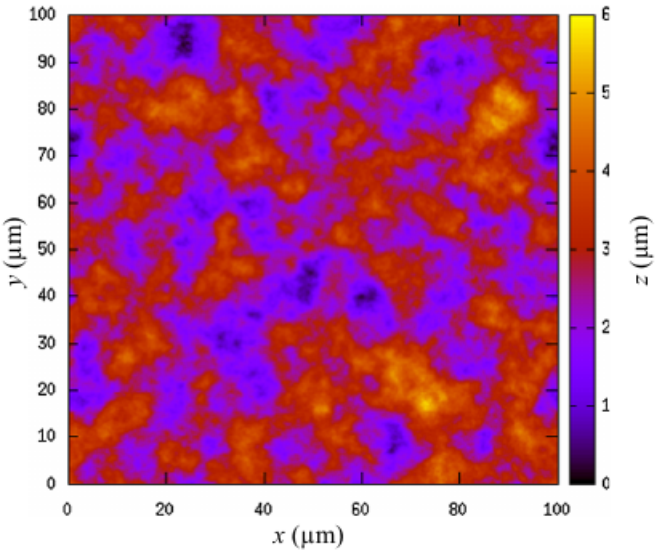


Figure 1.25: Height profile of the random surface that was produced from the spectrum shown in Figure 1.24. From [36].

# Chapter 2

# Methodological background

The aim of this chapter is introducing a procedure which allows describing the dynamics of driven systems, for example a tip sliding on a substrate, with the use of a few, relevant, states. Their definition is performed through a series of steps that we are going to describe in the following.
As a starting point, one needs to perform a long Molecular Dynamics (MD) simulation of the system. MD is widely used to study different kind of systems; in the present case, this technique has the ability of describing frictional systems at the nanometric scale, with atomistic detail. If the MD simulation is long enough, the system is able to visit all the relevant conformations a statistically meaningful number of times. Note that a long trajectory can also be replaced by a large number of short trajectories, if the length of the simulations is sufficient, larger than the time required from the system to loose memory of its initial configuration.
Once a long trajectory is available, the main problem to solve is to identify a bunch of states able to condense the most important features of the simulated dynamics. The most visited states correspond to the minima of the free energy of the system. When solving the equation of motion with Langevin dynamics, we recover Boltzmann statistics, and the most favoured configurations are the ones with lower energy, as far as the trajectoty is ergodic. As simple as this statement can appear, identifying those minima is not an easy task. Solving this problem implies addressing the long-standing problem of the characterization of the configurations with few collective variables, able to describe the dynamics of the system. We propose to address this problem using a new clustering procedure that will be described in the following. This allows mapping a large number of configurations into a discrete, small number of microstates.
Once the coarse graining of the system is complete, the trajectories (mapped into a jump process between the different microstates) are employed to built a transition matrix, which can be diagonalized. The eigenvalues and eigenvectors of this matrix can be used to build a so-called Markov State Model (MSM) [45]. In practice, this approach allows determining the time-scales of the main slow modes of the dynamics and obtaining the time-dependent probability distribution of every quantity.
In Fig. 2.1 we show an outline of the pipeline adopted in the present work.

## 2.1 Molecular Dynamics

As stated above, the analysis begins with a classical MD simulation long enough to explore all relevant configurations in phase space a sufficiently large number of times. Friction experiments consist in the sliding of a tip (usually an AFM tip) on a crystalline surface. The dissipation source is the work of the external force necessary to move the tip.

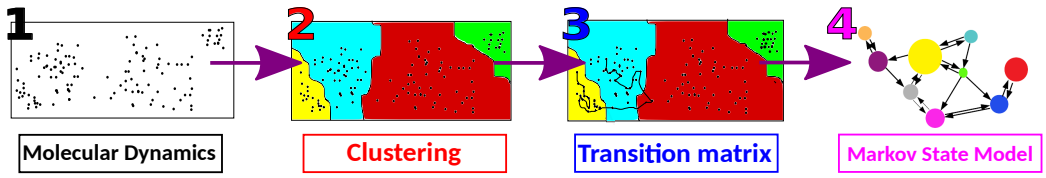


Figure 2.1: Outline of our analysis approach: the MD simulation, the dimensional reduction performed with the clustering approach, the calculation of the time scales with the transition matrix and, finally, the description in terms of Markov State Model.

To resemble friction experiments, our simulations will always concern the interplay between a moving object, called *slider*, and a surface, addressed as *substrate*. Note that, differently from the majority of simulations to which MSM has been applied to so far, our dynamics is out of equilibrium and does not satisfy detailed balance. We will come back to this point later in this chapter.
The dynamics is modeled by an overdamped Langevin dynamics. Let us have a look at the different systems studied in this work.

### 2.1.1 1D Frenkel-Kontorova

As described in Section 1.1.2, the first system studied is a one-dimensional Frenkel-Kontorova model, whose Hamiltonian reads (see Equation 1.6):

$$H(t) = \sum_i \left[ \frac{p_i^2}{2m} + \frac{K}{2}(x_{i+1} - x_i - a_c)^2 + \frac{U_0}{2}\cos\left(\frac{2\pi x_i}{a_b}\right) + \frac{\kappa}{2}(x_i - v_{drag}\cdot t)^2 \right] .$$

It consists of a chain of particles linked with springs of constant $K$, subject to a constant periodic potential of magnitude $U_0$. The chain is dragged with a constant velocity $v_{drag}$ applied to the whole chain. The two main lengths of the system, the springs equilibrium distance $a_c$ and the substrate periodicity $a_b$, can coincide or be different. In the first case the FK model is named commensurate; it is called incommensurate otherwise (see Figure 1.5, reported also below).

The overdamped Langevin dynamics for a particle labeled by the index $l$ in the 1D Frenkel-Kontorova is the following:

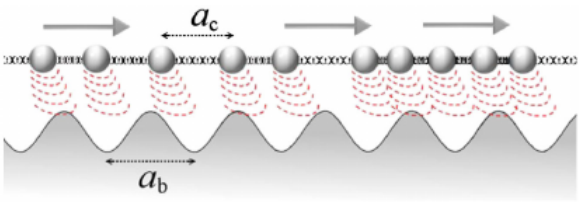


Figure 2.2: Sketch of 1D Frenkel-Kontorova.

$$x_l{}^{t+dt} = x_l{}^t + \left[\frac{\pi U_0}{\gamma m a_b}\sin\left(\frac{2\pi x_l{}^t}{a_b}\right) + \frac{\kappa}{\gamma m}(v_{drag} - x_l{}^t) - \frac{k}{\gamma m}(2x_l{}^t - x_{l-1}{}^t - x_{l+1}{}^t)\right]dt + \\ + \sqrt{\frac{2dt}{\gamma m\beta}}f^t\ , \tag{2.1}$$

where $f^t$ is harvested from an uncorrelated Gaussian distribution and $dt$ is the time step. $\gamma$ is the damping of the Langevin dynamics , and the system is immersed in a bath of inverse temperature $\beta = 1/k_B T$.

### 2.1.2 2D Frenkel-Kontorova

We also consider a 2D version of Frenkel-Kontorova model. The island is made by 1027 particles arranged in an hexagonal shape coupled by springs of constant $K$ (see Figure 1.6). The Hamiltonian reads (as in Equation 1.7):

$$H(t) = \sum_i \left[\frac{\mathbf{p}_i^2}{2m} + \frac{K}{2}(\mathbf{r}_{i+1} - \mathbf{r}_i - a_H)^2 + V(\mathbf{r}_i) + \frac{\kappa}{2}(x_{CM} - v_{ext}\cdot t)^2\right]\ .$$

The center of mass is coupled by a spring of constant $\kappa$ to a dummy tip which drags it with constant velocity $v_{ext}$, while $V$ is a potential with triangular symmetry like the one in Equation 1.8:

$$V(x,y) = U_0\left[2\cos\left(\frac{2\pi}{a_b}x\right)\cos\left(\frac{2\pi}{a_b}\frac{y}{\sqrt{3}}\right) + \cos\left(\frac{4\pi}{a_b}\frac{y}{\sqrt{3}}\right)\right]\ .$$

The overdamped Langevin dynamics is:

$$\mathbf{r}_l{}^{t+dt} = \mathbf{r}_l{}^t + \\ \left[\frac{1}{\gamma m}\nabla V(\mathbf{r}_l{}^t) + \frac{\kappa}{\gamma m}\left(v_{ext}t - \frac{1}{N}\sum_j x_j{}^t\right) - \frac{K}{\gamma m}\sum_{j\in NN}\left(\mathbf{r}_l{}^t - \mathbf{r}_j{}^t\right)\right]dt + \sqrt{\frac{2dt}{\gamma m\beta}}\mathbf{f}^t\ , \tag{2.2}$$

To simulate the Frenkel-Kontorova model in 1D and 2D, we directly implemented a MD code.

### 2.1.3 Graphene plaquette on gold

The realistic model we simulated and analyzed is a circular island of 1440 graphene atoms, saturated by 96 hydrogen atoms. Graphene has been chosen for its wide use in both research and

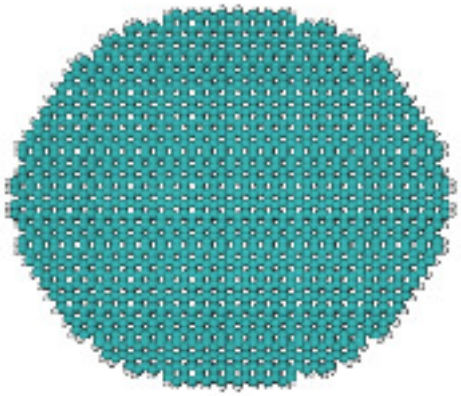

Figure 2.3: Circular graphene plaquette saturated by hydrogens.

technology. Moreover, regarding our simulations, graphene is the ideal slider since it is really stiff and experiences no wear. Because of these features, it precisely describes and follows the $z$ profile of the gold substrate, while sliding. A snaphot of the system can be seen in Figure 2.3; a circular shape has been chosen instead of an hexagonal one, since in experiments the shape of the slider is never perfectly polygonal. The substrate has been obtained from an FCC gold bulk, extruding excess gold so as to have your remaining bulk surface have a profile which is a self-similar random surface, adapting to our study the self-similar $512 \times 512$ surface by Müser (see Figure 1.24 and Figure 1.25). The $512 \times 512$ surface from the Contact-Mechanics challenge has been chosen; the lattice spacing $a$ has been replaced from the one in [36] to the typical gold-gold bond distance, namely 2.88 Å, in the $(x - y)$ plane, while in the $z$ direction the spacing has been taken as half of the Au-Au bond, as simulations with $a_z = 2.88$ Å created a profile with too rough asperities, getting the MD simulations into troubles. We remind that the Hurst exponent for this surface is $H = 0.8$. In order to create a larger substrate, a mirroring of the initial height profile has been done reflecting $x$, $y$, and $(x, y)$ coordinates respectively; the four surfaces obtained from this procedure have been stuck together. Starting from an FCC bulk of gold, its surface has been shaped according to the profile just created; finally, a strip has been cut from this substrate, with an orientation of 47°. The result for the height profile is shown in Figure 2.4, while in Figure 2.5, a focus on the substrate and the slider with atomistic detail is shown.

### AIREBO potential

For the simulation of the graphene plaquette sliding on gold we used LAMMPS [1, 43]. The plaquette is driven in a way similar to the 2D Frenkel-Kontorova, e.g. by a dummy atom coupled to the center of mass with a spring of constant $\kappa$. The advantage of using LAMMPS is the presence of specific force fields to describe the interaction between the different atomic species. We adopted the AIREBO potential [49] for both carbon-carbon and carbon-hydrogen interactions, and the Shifted-Force Lennard-Jones [51] for carbon-gold interaction. The AIREBO potential consists of three terms:

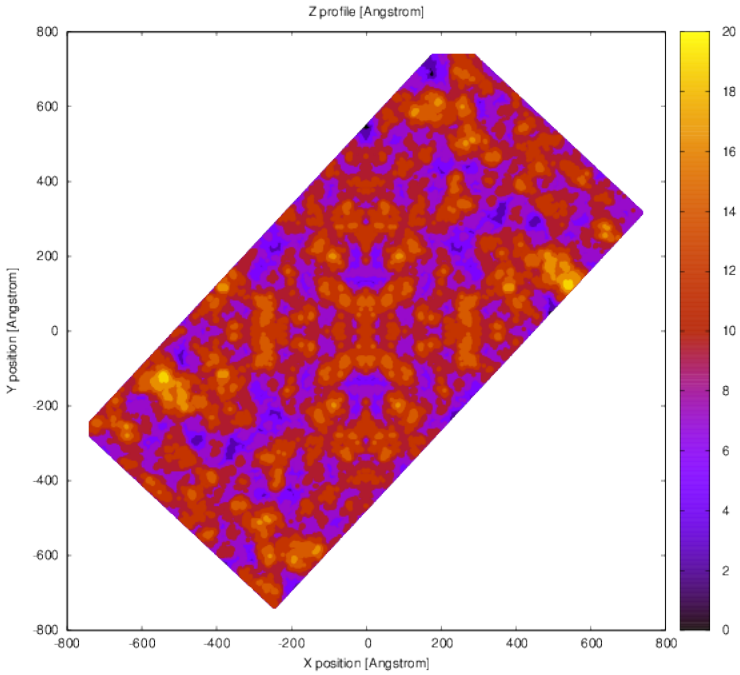


Figure 2.4: $z$ profile of the surface used in the simulations, together with a frame showing the slider over the gold substrate, with atomistic detail.

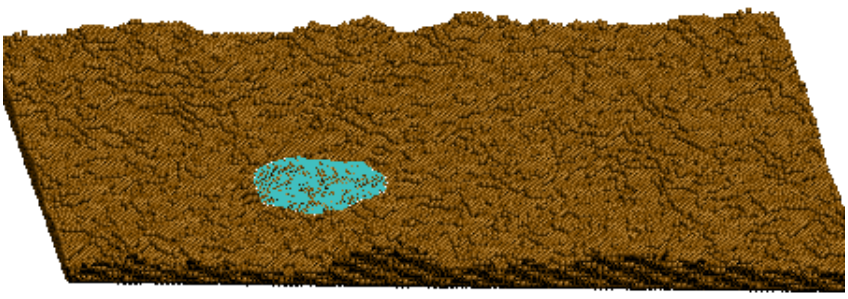

Figure 2.5: Slider deposited on the gold substrate.

$$E = \frac{1}{2}\sum_{i}\sum_{j\neq i}\left[ {E_{ij}}^{REBO} + {E_{ij}}^{LJ} + \sum_{k\neq i,jl\neq i,j,k} E^{TORSION}(\omega_{ijkl}) \right] , \tag{2.3}$$

where $E^{REBO}$ is a potential typical of hydrocarbon interaction:

$${E_{ij}}^{REBO} = f^c(r_{ij})(1 + Q/r_{ij})Ae^{-\alpha r_{ij}} + b_{ij}f^c(r_{ij}) \sum_{n=1,3} B_n e^{-\beta_n r_{ij}} , \tag{2.4}$$

where $r_{ij}$ is the scalar distance between atoms $i$ and $j$ and $f^c(r_{ij})$ is a function limiting the range of the covalent interactions. All the other parameters are fit from datasets of equilibrium distances, energies and stretching force constants for single (from diamond), conjugated double (from graphite), full double (from ethene), and triple (from ethyne) bonds. For further detail, see [7]. $b_{ij}$ is the bond-order term. $E^{LJ}$ is a Lennard-Jones interaction:

$${E_{ij}}^{LJ} = 4\epsilon_{ij}\left[ \left(\frac{\sigma_{ij}}{r_{ij}}\right)^{12} - \left(\frac{\sigma_{ij}}{r_{ij}}\right)^{6} \right] . \tag{2.5}$$

Finally, $E^{TORSION}$ is a 4-body potential that describes dihedral angle in hydrocarbons:

$$E^{TORSION}(\omega) = \epsilon\left[ \frac{256}{405}\cos^{10}\left(\frac{\omega}{2}\right) - \frac{1}{10} \right] . \tag{2.6}$$

The constants in Equation 2.6 are chosen such that when the torsional interactions are summed over the nine dihedral angles in a bond between identically distributed $sp^3$ carbons, the overall molecular torsion potential has the expected three-fold symmetry with a barrier height of $\epsilon$; further details can be found in [49].

## 2.2 Clustering

Dealing with a lot of data has become common in a lot of areas nowadays. The simulation of complex systems is not an exception. In our project, we can take advantage of modern techniques developed to address this problem, like the clustering analysis. These kind of technique belong to the "unsupervised learning" family of methods.
Clustering analysis is the task of grouping objects into groups (or clusters) sharing common characteristics. Objects are usually considered to be similar if they are "close" in some space, where proximity is defined, based on a certain concept of distance. The features chosen to define a configuration (positions, velocities, etc., defined case-by-case) form what will be called a *metric*.
In this project we have employed two different clustering algorithms. The first one, called Density-Peak algorithm (DP), has been introduced in 2014 by Rodriguez and Laio [47]. It is based on the idea that cluster centers are the points of highest density in their neighborhood, and that they are characterized by a relatively large distance from points with higher densities. With these assumptions, a clustering algorithm is defined, in which the number of clusters arise naturally from the analysis and is not defined a priori. In this approach, clusters are identified regardless of their shape and the dimensionality of the space in which they are embedded.
The second clustering algorithm employed is an variant of DP clustering not depending on a cutoff for the density. It is exploiting Point-Adaptive k-Nearest-Neighbors (PAk) [46] non-parametric density estimator, which automatically measures the density in the manifold containing the data. This method requires, as a preliminary step, the estimation of the intrinsic dimension, namely

of the minimum number of coordinates required to describe the dataset without significant information loss. Importantly, the PAk density estimator provides an estimate of the error, allowing the distinction between genuine probability peaks and density fluctuations due to finite sampling. Using this extension of DPA will allow clustering the configurations in a fully unsupervised manner.

### 2.2.1 Estimating the intrinsic dimension

Historically, several methods have been developed to compute the ID of a set of data. The early ones have been projective methods like PCA [15], invented by Pearson in 1901, exploiting a linear projection of the data on an hyperplane of dimension $d$. Commonly to all other projective methods, it searches for a subspace to project the data by minimizing a projection error. The main idea of PCA is making a linear combination of the data $\{\mathbf{X}\}$, as in the following:

$$Y^i = \sum_k w_k {X_k}^i \ , \tag{2.7}$$

where the vector $\{\mathbf{W}\}$ is chosen so that the variance of $\{\mathbf{Y}\}$ is maximal. If the projection of $\{\mathbf{X}\}$ over $\{\mathbf{Y}\}$ can be truncated at some value $\bar{k}$, such that $\lambda_k$ are large up to some value $\bar{k}$, and $\lambda_k/\lambda_{\bar{k}} \ll 1$ for $k = \bar{k}+1, \ldots, D$, then $d = \bar{k}$ is assumed to be the intrinsic dimension of the dataset. In some cases a gap does not exist between "large" and "small" eigenvalues; this condition does not imply that a manifold does not exist, it just shows that the manifold is not isomorphic to a hyperplane: in this case projective methods will fail.
A different approach for computing the ID has been adopted by Procaccia and Grassberger (1983) [16, 25] (GP algorithm). For any positive number $r$, the GP algorithm defines a correlation sum $\hat{C}(r)$ as the fraction of pairs whose distance is smaller than $r$. $\hat{C}(r)$ is monotonically decreasing to zero at $r \to 0$. If the correlation integral $C(r)$ decreases like a power law, $C(r) \sim r^d$, then $d$ is called the correlation dimension of $\mu$. Formally the ID is defined by $d = \lim_{r\to 0} \frac{\log(C(r))}{log(r)}$.

### 2.2.2 Density-Peak Algorithm

In this section we describe the clustering algorithm introduced in 2014 by Rodriguez and Laio [47]. This method is based only on the concept of distances between data points, and does not require to decide a priori the number of clusters. It does not require any projection of the data on a hyperplane.
The main concept is to identify cluster centers as maxima of local density of the data points. In fact, the algorithm assumes that cluster centers are surrounded by a neighborhood of lower local density, and that they are also at a relative large distance from other points of higher density.
In order to locate cluster centers, the authors compute two quantities for each point: its local density $\rho_i$ and its distance $\delta_i$ from points of higher density. Both these quantities depend only on the distances $d_{ij}$ between data points. The local density $\rho_i$ of data point $i$ in the original implementation of the algorithm is estimated as:

$$\rho_i = \sum_j \chi(d_{ij} - d_c) \ , \tag{2.8}$$

where $\chi$ is the characteristic function, while $d_c$ is a cutoff distance. The considerations for the cluster centers assignation rely only on the relative density between points. Because of this, just the relative magnitude $\rho_i$ in different points is important, and for large dataset the results obtained are robust with respect to the choice of $d_c$. The distance $\delta_i$ of point $i$ from points of higher density is simply:

$$\delta_i = \min_{j:\rho_j > \rho_i} (d_{ij}) \, . \tag{2.9}$$

For the highest-density points, this quantity cannot be computed and it is conventionally set as $\delta_i = \max_i(d_{ij})$ is adopted. Note that $\delta_i$ is much larger than the typical nearest neighbor distance only for points that are local or global maxima in the density. Thus, cluster centers are recognized as points for which the value of $\delta_i$ is anomalously large. This observation, which is the core of the algorithm, is illustrated by a simple example in Figure 2.6.

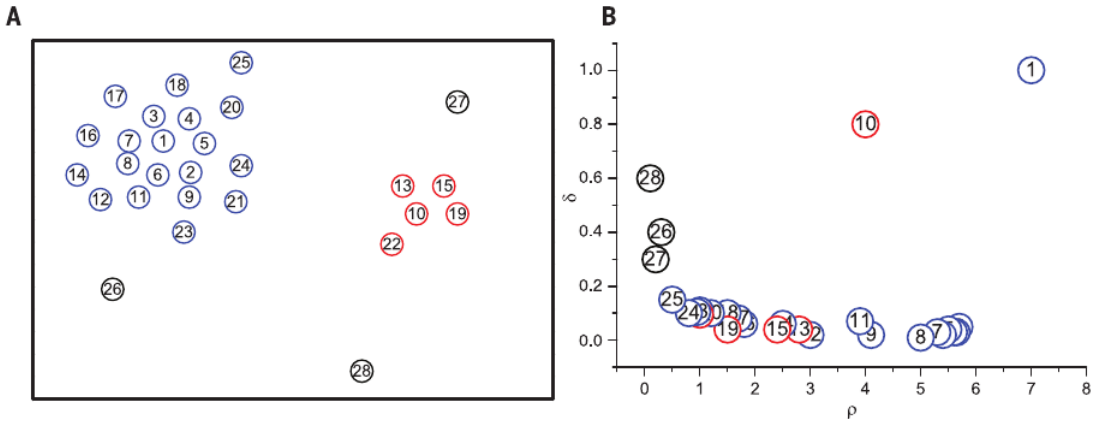


Figure 2.6: The algorithm in two dimensions. (A) Point distribution of 28 points embedded in a two-dimensional space. Data points are ranked in order of decreasing density. (B) Decision graph for the data in (A). Different colors correspond to different clusters. Density maxima are found at points 1 and 10: these points are then identified as cluster centers. Points 26, 27, and 28 have a relatively high $\delta$ and a low $\rho$ because they are isolated; they can be considered as clusters composed of a single point, namely, outliers. From [47].

After the cluster centers have been found, each remaining point is assigned to the same cluster as its nearest neighbor of higher density. The method is robust with respect to changes that do not significantly affect the distances below $d_c$, that is, that keep the ranking of the density approximation unchanged. The distance in Equation 2.9 will be affected by such a change of metric, but the structure of the decision graph (in particular, the number of data points with a large $\delta$) is a consequence of the ranking of the density values, not of the actual distance between far away points. An example of a typical decision graph can be seen in Figure 2.6(B).
DP algorithm has few important drawbacks that are going to be overtaken by the adaptive method described in the Section 2.2.4. First, the identification of the peaks has to be made by visual inspection of the decision graph: this implies that the selection of the cluster centers is relatively subjective. Secondly, the density estimate in DP clustering is based on Equation 2.8, which depends on the cutoff parameter $d_c$, making the method sensible to the change of this parameter.

### 2.2.3 The Two-NN intrinsic dimension estimator

We have already discussed why projective methods like PCA are not always appropriate to the calculation of the intrinsic dimension, as they require the projection of the data points on an hyperplane. Fractal methods like the GP algorithm are different, as they compute the volume of a sphere in $d$ dimension, varying the radius $r$ and estimating the growth of the number of observations

included in the sphere, as $r$ increases. Therefore, they have difficulties when the density varies rapidly, or the curvature of the embedding manifold is large. This determines systematic errors in the estimate.
We now describe an estimator for the intrinsic dimension that is relatively insensitive to density variations and curvatures. Its name is Two-NN [14], and it requires computing only the distances to the first two nearest neighbors of each point. This method is based on the idea that, if the density is constant around point $i$, all the hypershells $\Delta\nu_l$ enclosed by further neighbors $l$ are independently drawn from an exponential distribution with rate equal to the density $\rho$. Because of this, it is possible to find a quite simple relationship between the value of the ID and of the ratio $\mu \equiv \frac{r_2}{r_1} \in [1, +\infty)$, where $r_2$ is the distance between point $i$ and the second neighbor, while $r_1$ is the distance from the first neighbor.

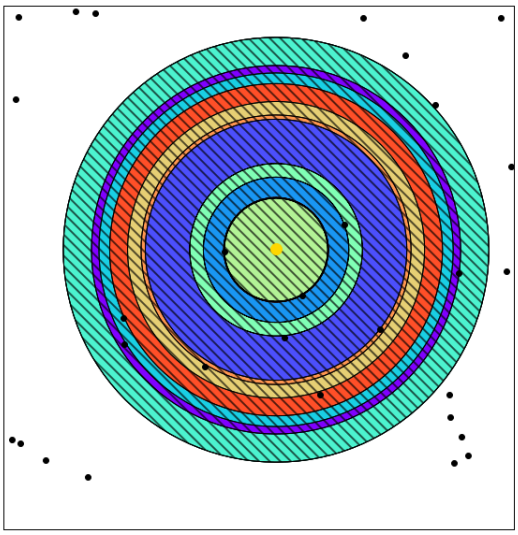

Figure 2.7: Hyperspherical shells of volume, labeled with different colours. Credits: Alex Rodriguez.

For every point $i$ of the dataset, one computes its distance from the first $k$ neighbors, obtaining a list of distances, in increasing order, $r_1 < r_2 < \ldots < r_k$, from point $i$ to its first, second, $k$-th neighbor (see a sketch in Figure 2.7). $r_0$ is set to zero by definition. The volume of the hyperspherical shell enclosed between two successive neighbors $l-1$ and $l$ is given by:

$$\Delta\nu_l = \omega_d({r_l}^d - {r_{l-1}}^d) \,, \tag{2.10}$$

where $d$ is the dimensionality of the space in which the points are embedded and $\omega_d$ is the volume of the $d$-sphere with unitary radius. If the density is constant around point $i$, all the $\Delta\nu_l$ are independent and distributed according to an exponential distribution with rate equal to the density $\rho$:

$$P(\Delta\nu_l \in [\nu, \nu + d\nu]) = \rho e^{-\rho\nu} d\nu \,. \tag{2.11}$$

Consider two shells $\Delta\nu_1$ and $\Delta\nu_2$ and let $R = \frac{\Delta\nu_1}{\Delta\nu_2}$; after some calculation (more details can be found in [14]) the probability distribution function for $R$ can be found. It reads:

$$g(R) = \frac{1}{(1+R)^2} \ . \tag{2.12}$$

It is important to note that this distribution function does not depend explicitly on the dimensionality $d$, included just in the definition of $R$. In order to extrapolate the value of the intrinsic dimension $d$, we need a formula that takes directly this quantity into account. In order to do so, we consider the quantity $\mu \equiv \frac{r_2}{r_1} \in [1, +\infty)$. $R$ and $\mu$ are, in fact, related by the equality $R = \mu^d - 1$. From these quantities it is possible to find the explicit form of the distribution of $\mu$:

$$f(\mu) = d\mu^{-d-1}\chi_{\{1,+\infty\}}(\mu) \ , \tag{2.13}$$

where $\chi_{\{1,+\infty\}}$ is the characteristic function of the set $\{1, +\infty\}$, while the cumulative distribution function is obtained by integration:

$$F(\mu) = (1 - \mu^{-d})\chi_{\{1,+\infty\}}(\mu) \ . \tag{2.14}$$

The functions $f$ and $F$ are independent of the local density, but they depend explicitly on the intrinsic dimension $d$. The value of $d$ can now be estimated, using the formula:

$$d = \frac{\log(1 - F(\mu))}{\log(\mu)} \ , \tag{2.15}$$

which is obtained by taking the logarithm of both members of Equation 2.14. In Figure 2.8 the quantity $-\log(1-F^{empirical}(\mu))$ as a function of $\log(\mu)$ is shown for three datasets containing 2500 points: a dataset drawn from a uniform distribution on a hypercube in dimension $d = 14$, analyzed with periodic boundary conditions, another drawn from a uniform distribution on a Swiss Roll embedded in a three-dimensional space, and a Cauchy dataset in $d = 20$. By "Cauchy dataset" we refer to a dataset where the norms of points are distributed according to the pdf $f(x) = 1/(1+x^2)$. According to the Two-NN estimator, the value of the ID for the uniform hypercube is $d = 14.09$, a measure that is consistent with the true value. For the Swiss Roll the ID estimated is $d = 2.01$, corresponding to the dimension of a hyperplane tangent to the Swiss Roll. This problem can be overcome by discarding a certain percentage of the points characterized by a large value of $\mu$. After this procedure, the new slopes have values $d = 13.91$, $d = 2.01$ and $d = 22.16$, for the hypercube, the Swiss Roll and the Cauchy datasets respectively. The value $d = 22.16$, larger than the nominal one $d = 20$, has been caused by the presence of outliers.

Two-NN method has been tested also in real worlds datasets, like sets of images and MD configurations, being able to correctly estimate the density using just the two closest neighbors of data points. In the following sections, we are going to see how the combination of Density Peak algorithm with PAk estimator allows the identification of principal minima of the free energy.

### 2.2.4 Adaptive Density-Peak clustering

In 2018 Rodriguez *et al.* [46] introduced a technique that provides estimates of the free-energy in high-dimensional spaces without performing any explicit dimensional reduction, called Point-Adaptive k-Nearest-Neighbors (PAk). Differently from previous methods, PAk does not require any projection of the points on a plane, and it does not depend on any parameter to be fixed, avoiding any assumption on the functional form of the density function. Differently from a popular non-parametric estimator like the k-Nearest-Neighbor (k-NN) estimator, where the local density at a point is measured as the ratio of the number of nearest neighbors $k$ to the volume they occupy, PAk does not set a global value a priori for $k$. It is well-known, in fact, that using a global smoothing

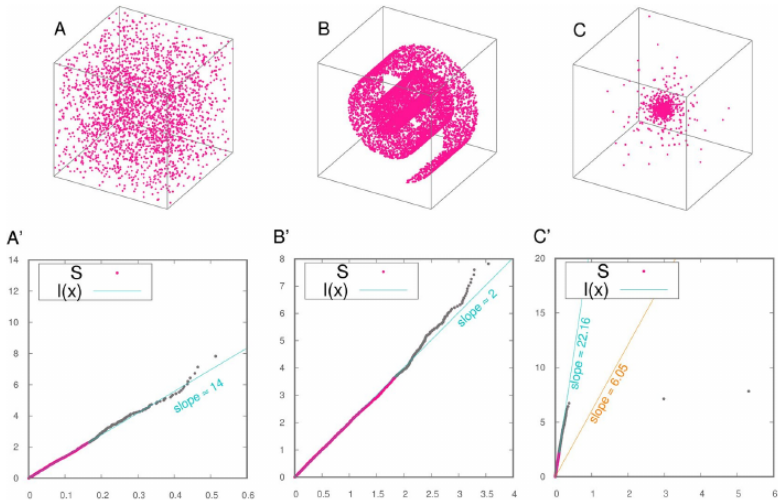


Figure 2.8: The fitting function $l(x)$ in three exemplar datasets of 2500 points. In the first column we display the dataset while in the second one we represent dataset $S$ (pink dots) together with the discarded points (gray dots) and the fitting function $l(x)$. Panel A, A': cube in dimension 14 (in panel A only the first 3 coordinates are represented) analyzed with pbc. Panel B, B': a Swiss Roll. Panel C, C': a Cauchy dataset in $d = 20$ (only the first 3 coordinates are represented). From [14].

parameter in highly inhomogeneous data sets induces systematic errors. PAk is based on finding, for each point, the size of the neighborhood in which the free energy is approximately constant (see Figure 2.9). Moreover, PAk measures the density in the manifold in which the data lay, and not in the embedding space whose dimensionality is normally overwhelmingly large, providing also a measure of the uncertainty on the density.

Consider $\{X_1, \ldots, X_N\}$ as a set of $N$ independent and identically distributed random vectors with values in $\mathbb{R}^D$. We assume that the $X_i$'s lie on a manifold of dimension $d \leq D$, constant in the data set. The calculation of the intrinsic dimension $d$ of the manifold is exploited by the Two-NN method described in Section 2.2.3. We remind that the hypershells of volume around a point $i$ are independently drawn from an exponential distribution with rate equal to the density $\rho$. Because of this, we can write the log-likelihood function of the parameter $\rho$ given the observation of the k-nearest neighbor distances from point $i$:

$$\mathcal{L}(\rho|\{\nu_{i,l}\}_{l\leq k}) \equiv \mathcal{L}_{i,k}(\rho) = k\log(\rho) - \rho\sum_{l=1}^{k}\nu_{i,l} = k\log(\rho) - \rho V_{i,k} \ , \tag{2.16}$$

where $V_{i,k} = \sum_{l=1}^{k}\nu_{i,l}$ is the volume of the hypersphere with center at $i$ containing $k$ data points, which is estimated as:

$$\nu_{i,l} = \omega\left(r^d{}_{i,l} - r^d{}_{i,l-1}\right) \ , \tag{2.17}$$

where $r_{i,l}$ denotes the distance from the point $i$ to the $l$-th neighbor, $\omega$ is a constant and $d$ is the intrinsic dimension. Maximizing the likelihood with respect to $\rho$, an expression for the constant

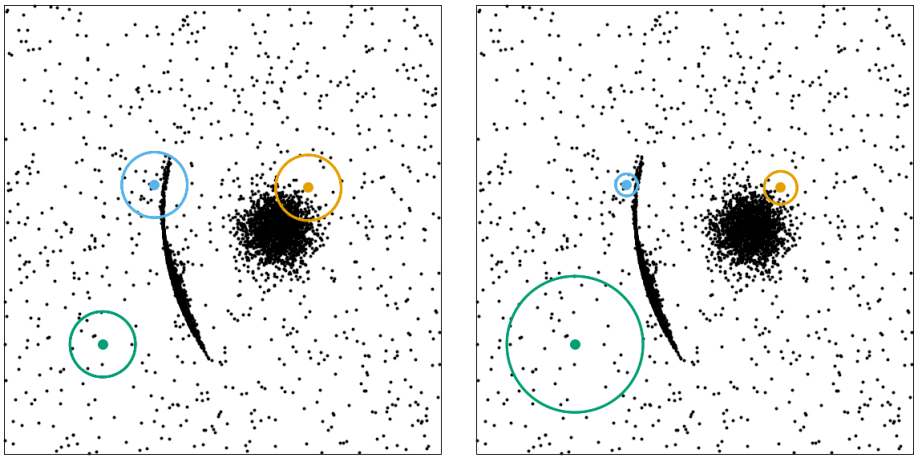

Figure 2.9: On the left, sketch of k-NN neighborhood in the case of non-constant density data. It is evident that a common value of $k$ would fail in estimating the density. On the right, PAk estimation of the neighborhood, for the same data landscape. Credits: Alex Rodriguez.

density is obtained as $\rho = k/V_{i,k}$, which coincides with the standard k-NN estimator of the local density. The estimated error on $\rho$ is given by the standard deviation $\varepsilon_\rho = \rho/\sqrt{k} = \sqrt{k}/V_{i,k}$.
The error of the standard k-NN gets smaller as $k$ increases. However, when $k$ increases, the density in the neighborhood within a distance $r_{i,k}$ from the point $i$ can become non-constant. In order for the method to be reliable, a likelihood-ratio test is performed to choose the largest $k$ possible for which the condition of constant density holds within a given level of confidence. Two models are compared: one in which the densities of point $i$ and of its $(k+1)$-th nearest neighbor are different, and a second one, where the density at point $i$ is assumed to be equal to the density at its $(k+1)$-th nearest neighbor. The two models are considered distinguishable with a high statistical confidence if the difference between the log-likelihood of the two models is larger than a threshold value (the p-value chosen is $10^{-6}$). For each point $i$ the optimal value of $k$ is chosen (denoted in the following by $\hat{k}_i$) as the largest value of $k$ for which the two models are not distinguishable. The error on the logarithm of the density is estimated from the variance of the likelihood [11]. It is really useful to supply the measure of the density with an error, in order to distinguish spurious cluster from real ones.
We now describe the modified version of the DPA algorithm which exploits the PAk density estimator. To find the density peaks, the authors do not consider the density of points, which typically varies by several orders of magnitude, but the logarithm of the density $\log(\rho_i) = -F_i$, identified as the free-energy at point $i$. Moreover, since the estimate of $F$ can be affected by non-uniform errors, the cluster centers are defined as the local maxima of $g_i$, where:

$$g_i = \log(\rho_i) + \varepsilon_i = -F_i + \varepsilon_i \ . \tag{2.18}$$

The local maxima of $g_i$ coincide with the local maxima of $\rho_i$, if the error is uniform. If the error is not uniform, points with large error are less likely to be selected as local maxima with respect to points with a small error. Following [47], the quantity $\delta_i$ is computed, namely the distance to the nearest point with higher $g$. In order to automatically find the cluster centers, the algorithm takes advantage of the fact that PAk provides an estimate of the size of the neighborhood in which the logarithm of the density can be considered constant. Therefore, putative centers are considered

points for which $\delta_i > r_{\hat{k}_i}$, where $\hat{k}_i$ is the optimal value of nearest neighbors, and $r_{\hat{k}_i}$ the distance from this neighbor. Thus, a data point $i$ is a center only if all its $\hat{k}$ neighbors contributing to determining the value of its density have a value of $g$ lower than $g_i$. A further check, which makes putative centers selection more robust in front of statistical fluctuations in the density estimation, is that a center cannot belong to the neighborhood of any other point with higher $g$. The next step is the assignation of all the points that are not centers to the same cluster as the nearest point with higher $g$. This assignation is performed in order of decreasing $g$.
It is important to underline that some density peaks may be spurious, due to poor sampling. An example is shown in Figure 2.10. In the figure, an example of a (1D) density is shown, with two density maxima separated by a saddle point. One can notice that several spurious density peaks are present, due to the uncertainty of the density estimate. In order to recognize genuine density peaks from spurious peaks due to statistical errors, we proceed as follows. Consider two clusters $c$ and $c'$: a point $i$ belonging to cluster $c$ is assumed to be at the border between $c$ and $c'$ if its closest point $j$ belonging to $c'$ is within a distance $r_{\hat{k}_i}$ and if $i$ is the closest point to $j$ among those belonging to $c$. The saddle point between a pair of clusters $c$ and $c'$ is defined as the point with the highest value of $g$ among those at the border between $c$ and $c'$. The value of the logarithm of the density of this point and its error are denoted by $-F_{cc'}$ and $\varepsilon_{F_{cc'}}$. Based on the value of the saddle free energies $F_{cc'}$ and their error, the quantitative criterion aimed at distinguishing genuine density peaks from statistical fluctuations is the following:

$$(F_{cc'} - F_c) < Z \cdot (\varepsilon_{F_c} + \varepsilon_{F_{cc'}}) \,, \tag{2.19}$$

where $-F_c$ is the logarithm of the density of the center of the cluster $c$. If condition in Equation 2.19 holds, the two clusters are merged. The constant $Z$ in Equation 2.19 defines the level of statistical confidence at which one decides to consider a cluster meaningful. The condition in Equation 2.19 is checked for all the clusters $c$ and $c'$, in order of decreasing $-F_{cc'}$.

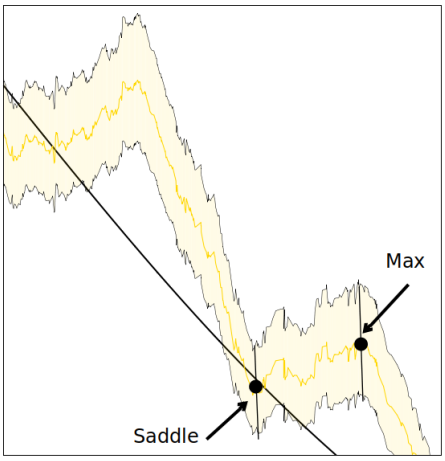


Figure 2.10: Spurious peak of the density: the saddle point density is compatible with the local maximum one, within the error. Credits: Alex Rodriguez.

## 2.3 Markov State Models

The other tool we are going to exploit in our work is Markov State Modeling, a well-established technique used to obtain a dynamic coarse-graining of a system, using a small number of relevant variables [37]. MSM models have been widely applied to protein folding and bio-molecules.
A similar problem is the one faced in the present work, where the aim is to describe realistic frictional systems in an unprejudiced and efficient way.
The "classical" version of MSM builds a model defined by $N$ states and parameterizes the model with the rates between these states. Classical MSMs often have many states, around hundreds. The reason to keep that many states is that it allows the construction of a very high resolution model of the dynamics: in this sense, short simulations are sufficient to observe transitions between them.
We will concentrate on MSMs created from MD simulation. The data from MD can take several forms, but in the majority of cases a configuration will be defined by the position of the particles at a certain time step. Even though what is meaningful in a Markov model is a kinetic description of the relevant state, the coarse graining procedure starts with a structural dimensionality reduction, using a clustering algorithm [31, 32]. Every configuration at a certain time will then be mapped into the cluster it belongs, as sketched in Figure 2.11. As previously stated, in this version of MSM the clusters can be many, but a clear definition of the geometric boundaries of the states is necessary. The definition of the clusters, or *microstates*, is entangled with the definition of a metric, a distance between two configurations. At a later time, if there exists a kinetic similarity between two microstates, they can be merged together.

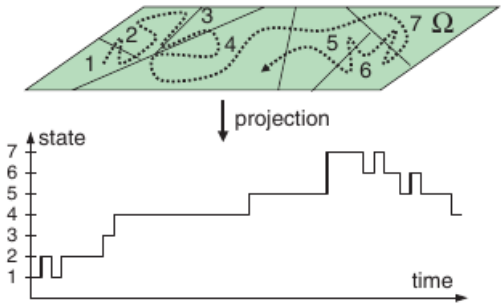


Figure 2.11: Scheme: The true continuous dynamics (dashed line) is projected onto the discrete state space. MSMs approximate the resulting jump process by a Markov jump process. From [45].

Once the states have been identified, a transition matrix between microstates is estimated. The dynamics has turned into a series of jumps between microstates. In particular, one estimates a matrix with elements $C_{ij}(\tau)$, counting the number of jumps from the microstate $i$ to the microstate $j$ in a time $\tau$. Once normalized, this matrix becomes the transition matrix $\Pi_{ij}(\tau)$, giving the probability of the jump from $i$ to $j$, in a time $\tau$. $\tau$ is defined as the lag time of the MSM model: the time distance between two states cannot be smaller than the decorrelation time of the system, in order for the Markovian hypothesis to be valid. The longer the lag time, the fewer the number of relevant states; however, enlarging the lag time results in a poorer statistics. Finally, a successive coarse graining of the states can be performed using methods that lump similar microstates together based on the eigenvalues and the eigenvectors of the transition matrix.

### 2.3.1 Classical version of MSM

In this section we are going to give a brief description of the classical version of Markov State Modeling, for the discrete-time case. Further details can be found in [45]. Consider a space $\Omega$ which contains the dynamical variables needed to describe the system; in the case of molecular simulations, $\Omega$ usually includes both positions and velocities of the particles of the system. We define $X^t = X \in \Omega$ at time $t$ and $X^{t+\tau} = X' \in \Omega$ two successive configurations separated by a time $\tau$. Moreover, let $\Pi^\tau(X \to X')$ be the probability to go from $X$ to $X'$ in a time $\tau$. MSM makes the following assumptions:

- $\Pi^\tau$ is a *Markov process*: this condition implies that the probability to go to $X'$ depends just on configuration $X$, and not on the previous history;
- the dynamical process constituted by the configurations $X$ explored is *ergodic*: this condition implies that the space $\Omega$ does not have two or more subsets that are dynamically disconnected, and that for $t \to \infty$ each state $X$ is going to be visited infinitely often. The fraction of time spent in any of the states $X$ during an infinitely long trajectory is denoted by its unique stationary density $\mu(X)$: Figure 2.12 shows the stationary density $\mu(X)$ for a diffusion process on a potential with high barriers;
- $\Pi^\tau$ satisfies *detailed balance*: this implies that:

$$\mu(X)\Pi^\tau(X \to X') = \mu(X')\Pi^\tau(X' \to X) \,, \tag{2.20}$$

  i.e. in equilibrium the fraction of time spent in the transition $X \to X'$ is the same as the fraction spent by the system in the transition $X' \to X$.

Of the three conditions described above, the third one can be relaxed as it is not essential for the construction of Markov Models, as we will discuss later. Indeed, we want to build a MSM of a driven system, where detailed balance does not hold.

The operator $\Pi^\tau(X \to X')$ has left eigenmodes $\{\psi_i\}$ that satisfy the following eigenvalue equation:

$$\int dX \Pi^\tau(X \to X')\psi_i(X) = \lambda_i \psi_i(X') \,. \tag{2.21}$$

We are now looking for a solution in the form of a linear combination of the eigenfunctions of the operator $\Pi^\tau$:

$$P(X,t) = \sum_i w_i(t)\psi_i(X) \tag{2.22}$$

where $w_i(t)$ is the weight of the eigenmode $\psi_i$ at time $t$. Substituting this expression in Equation 2.21, we obtain:

$$\sum_i w_i(t+\tau)\psi_i(X') = \int dX \Pi^\tau(X \to X') \sum_i w_i(t)\psi_i(X) \,. \tag{2.23}$$

From the eigenvalue relation in Equation 2.21, we can write: $w_i(t+\tau) = \lambda_i w_i(t)$. This reasoning can be iterated for successive jumps at time $2\tau$, $3\tau$, etc. We can finally conclude:

$$P(X,t) = \sum_i w_i(t=0){\lambda_i}^{-t/\tau_i}\psi_i(X) \,. \tag{2.24}$$

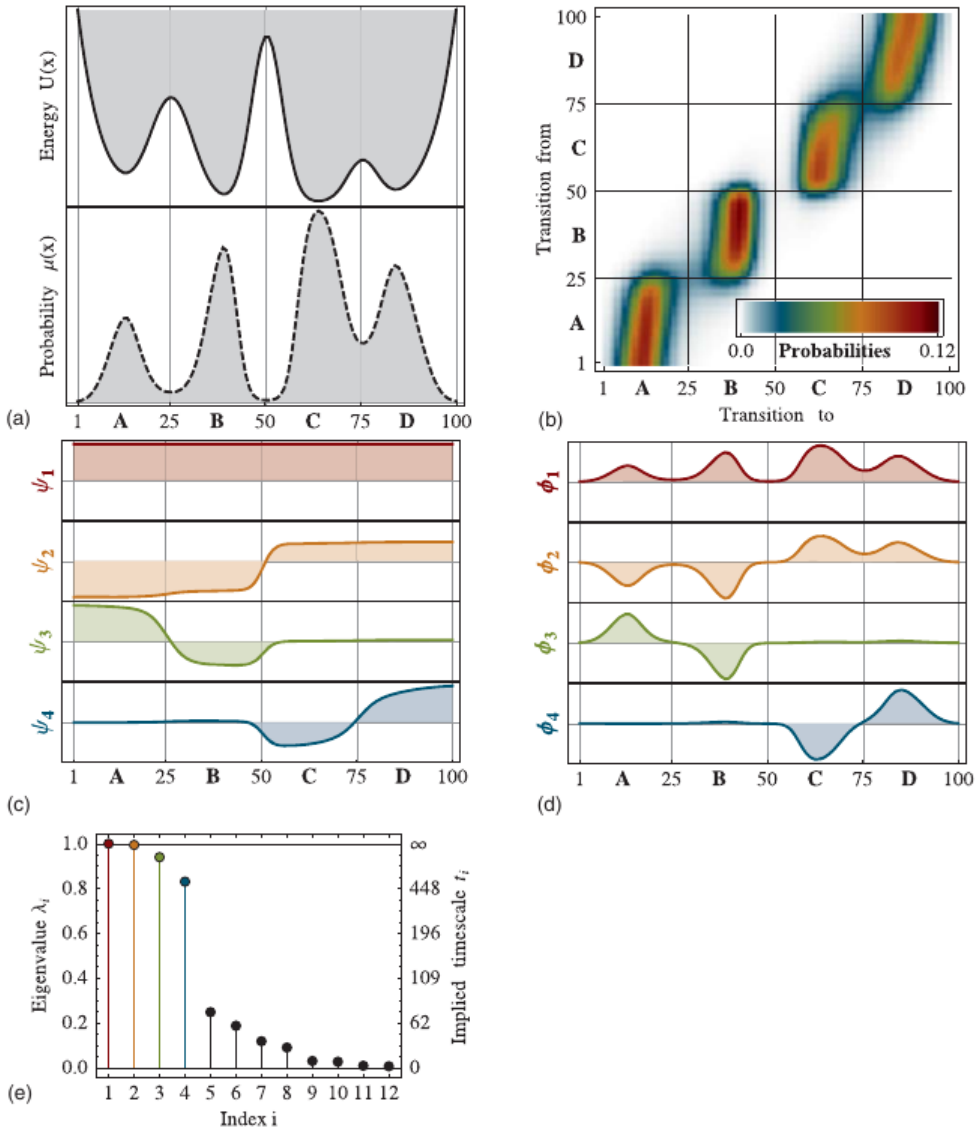


Figure 2.12: (a)Potential energy function with four metastable states and corresponding stationary density $\mu(X)$. (b) Density plot of the transfer operator for a simple diffusion-in-potential dynamics defined on the range $\Omega = [1, 100]$, black and red indicates high transition probability, white zero transition probability. Of particular interest is the nearly block-diagonal structure, where the transition density is large within blocks allowing rapid transitions within metastable basins, and small or nearly zero for jumps between different metastable basins. (c) The four dominant eigenfunctions of the transfer operator, $\psi_1, \ldots, \psi_4$, which indicate the associated dynamical processes. The first eigenfunction is associated with the stationary process, the second to a transition between $A + B \leftrightarrow C + D$, and the third and fourth eigenfunction to transitions between $A \leftrightarrow B$ and $C \leftrightarrow D$, respectively. (d) The four dominant eigenfunctions of the transfer operator weighted with the stationary density, $\phi_1, \ldots, \phi_4$. (e) Eigenvalues of the transfer operator, the gap between the four metastable processes ($\lambda_i \approx 1$) and the fast processes is clearly visible. From [45].

Hence, the eigenvectors $\{\psi_i\}$ allow us to describe the system studied in terms of probability distributions of the quantities coming from the dynamics, giving a clear physical description.
The transfer operator $\Pi^\tau$ defined above has eigenvalues $\{\lambda_i\}$, left eigenvectors $\{\phi_i\}$ and right eigenvectors $\{\psi_i\}$, see Figure 2.12(c-e). The relation $|\lambda_i| \leq 1$ holds, $\forall i$. The eigenvalue with the largest modulus is exactly 1, and if the evolution is ergodic there is only one such eigenvalue. The associated right eigenfunction corresponds to a constant function on all state space $\Omega$, as in Figure 2.12, at the top.
In some cases, a gap in the eigenvalue spectrum can be identified, distinguishing between a group of slow dynamical processes and another of fast dynamical processes. The slow part of the time scales is the dominant one, as it describes all the slowly decaying part of the dynamics, while the fast processes are usually not of interest. In fact, to each eigenvalue $\lambda_i$ we can associate a corresponding physical time scale indicating how quickly the perturbation to the equilibrium distribution described by the eigenvector $\psi_i$ decays (see Figure 2.12(e)):

$$\tau_i = -\frac{\tau}{\log(\lambda_i)} \ . \tag{2.25}$$

$\tau_i$ is often called the $i$-th implied time scale. The $i$-th process decays exponentially $\sim \exp(-t/\tau_i)$; the closer $\lambda_i$ is to 1, the slowest the process; conversely, the closer it is to 0, the faster. Therefore, in the long-time limit where $t \to \infty$, only the first term with $\lambda_1 = 1$ remains, recovering the stationary distribution $\phi_1(\mathbf{x}) = \mu(\mathbf{x})$. All other terms correspond to processes with eigenvalues $\lambda_i < 1$ and decay over time, thus the associated eigenfunctions correspond to processes that decay under the action of the dynamics and represent the dynamical rearrangements taking place while the ensemble relaxes toward the equilibrium distribution. This implies that when there are gaps among the first $m$ eigenvalues, the system has dynamical processes acting simultaneously on different time scales. A system with two-state kinetics would have $\lambda_1 = 1$, $\lambda_1 \approx 1$ and $\lambda_3 \ll \lambda_2$ ($t_3 \ll t_2$), while a system with a clear involvement of an additional kinetic intermediate would have $\lambda_3 \sim \lambda_2$ ($t_3 \sim t_2$). In Figure 2.12, the second process, $\psi_2$, corresponds to the slow exchange between basins $A + B$ and basins $C + D$, as reflected by the opposite signs of the elements of $\psi_2$ in these regions (Figure 2.12(d)). The next-slowest processes are the $A \leftrightarrow B$ transition and then the $C \leftrightarrow D$ transition, while the subsequent eigenvalues are clearly separated from the dominant eigenvalues and correspond to much faster local diffusion processes. The three slowest processes effectively partition the dynamics into four metastable states corresponding to basins $A$, $B$, $C$, and $D$, which are indicated by the different sign structures of the eigenfunctions (Figure 2.12(c)). Of special interest is the slowest relaxation time, $t_2$. This time scale identifies the global equilibration or decorrelation time of the system; no structural observable can relax more slowly than this time scale.
In conclusion, the Markov Model then consists in the partitioning of state space, combined with the transition matrix modeling the jump process sketched in Figure 2.11. Modeling the long-time statistics of this jump process with a Markov process is an approximation, i.e., it involves a discretization error. Once the microstates have been identified, a discrete transition matrix ${\Pi_{\alpha\beta}}^\tau$ is defined, where $\{c_\alpha\}$, $\alpha = 1, \ldots, n_c$ are the different microstates. This matrix is a finite $n_c \times n_c$ matrix with generic element:

$${\Pi^\tau}_{\alpha\beta} = \int_{X \in c_\alpha} \int_{X' \in c_\beta} dX dX' \mu(X) \Pi^\tau(X \to X') \ , \tag{2.26}$$

which is the probability to go from $c_\alpha$ to $c_\beta$ in time $\tau$. In general, ${\Pi^\tau}_{\alpha\beta}$ depends on the lag time $\tau$. ${\Pi^\tau}_{\alpha\beta}$ is estimated counting the jumps from $c_\alpha$ to $c_\beta$ in a time $\tau$.

### 2.3.2 Markov State Modeling of Sliding Friction

The method adopted in the present work has its basis in the classical MSM, but there exist some fundamental differences between our approach and the classic one that we would like to highlight. First of all, thanks to the use of Adaptive Density Peak clustering described in Section 2.2.4 which is able to identify the main free energy minima, the number of clusters identified are a few (of the order of $\sim 10$) instead of hundreds. The capability of locating just the principal minima is also fundamental in order to identify immediately the slowest modes of the system, characterized by the longest transition times.
Second, the system we have analyzed are driven systems. This implies that the dynamics is not reversible, and that detailed balance does not hold. Moreover, the phase space explored during the sliding grows linearly with time. To overcome this problem, the solutions adopted are different in the different cases. If the geometry of the system presents some periodicities, they are employed to find similarity between configurations in different locations. Otherwise, variables describing internal degrees of freedom of the frictional systems are used.
For the non-equilibrium case, we denote by $\{\lambda_i\}$ the eigenvalues of the transition matrix and by $\{\chi_i\}$ its left eigenvectors. Since we are not in equilibrium, as we said earlier, detailed balance does not hold. Hence, the eigenvalues of the transition matrix are not necessarily real. However, they still satisfy $|\lambda_i| \leq 1$, by the Perron-Frobenius theorem. The eigenvalue with the largest modulus is exactly 1, and if the evolution is ergodic there is only one such eigenvalue. The eigenvector $\chi_0$ represents the invariant, steady-state distribution, characterized by non-zero sliding current. The $\chi_i$ with $|\lambda_i| \simeq 1$ denote the long-lived excitations of the steady-state, which decay with long characteristic times $\tau_i = -\tau/\log(|\lambda_i|) \gg \tau$, while oscillating with period $\tau/\arctan(Im[\lambda_i]/Re[\lambda_i])$.

#### Probability distributions

The time-dependent probability distribution of a microstates $\alpha$ is given by:

$$P_\alpha(t) = {P_\alpha}^{SS} + \sum_i f_{i,\alpha}\, \psi_{i,\alpha}\, e^{-t/\tau_i}\ , \tag{2.27}$$

where ${P_\alpha}^{SS}$ is the steady-state probability, conditioned to the microstate $c_\alpha$, $f_{i,\alpha} = {\chi_i}^\alpha {P_0}^\alpha / {P_\alpha}^{SS}$ accounts for the initial condition (at time t=0) in $c_\alpha$; $P(t|\alpha)$ is the probability distribution of $c_\alpha$ at time $t$. For any observable $O$ we estimate its time-dependent probability distribution as follows. We first compute its probability distribution in each microstate $c_\alpha$, denoted by $P_\alpha(O)$; then, using Equation 2.27, we estimate $P(O,t)$ as follows:

$$P(O,t) = \sum_\alpha P_\alpha(t) P_\alpha(O) = P^{SS}(O) + \sum_i f_i g_i(O) e^{-t/\tau_i}\ , \tag{2.28}$$

where:

$$P^{SS}(O) = \sum_\alpha {P_\alpha}^{SS} P_\alpha(O)\ , \tag{2.29}$$

and:

$$g_i(O) = \sum_\alpha \psi_{i,\alpha}\, P_\alpha(O)\ . \tag{2.30}$$

# Chapter 3

# Sliding over a periodic substrate

In this chapter we are going to describe the first part of the results obtained with our approach. Our path will start from a toy model consisting in a chain of 10 commensurate Frenkel-Kontorova (FK) particles from Reference [38] (see Section 1.1.2). This system has been the first studied with this method. Hence, apart from representing a proof of concept demonstrating the validity of the study, it is useful to introduce the main steps concerning our analysis to the reader.
The second system we present is once again a 1D chain of FK particles, this time with a mismatch between lattice parameter of the the substrate and the equilibrium distance between two successive beads. This incommensurate system has been studied since in the thermodynamic limit, the incommensurability allows the presence of a phase transition (the Aubry transition) between a superlubric regime characterized by zero static friction, and a stick-slip regime with nonzero value (as described in Section 1.1.2). Even though a finite system always experiences a bit of stick-slip, that finite size effect is easy to discount.
We then studied a system with increased dimensionality (from 1D to 2D) and number of particles. With triangular symmetry, a 2D Frenkel-Kontorova island is a closer example for the sliding of two-dimensional crystalline surfaces.

## 3.1 1D commensurate Frenkel-Kontorova model

### 3.1.1 The model

We start describing the first system studied with MSM of sliding friction, a one-dimensional Frenkel-Kontorova model. This study follows Reference [38]. Even though this model may appear simple, it contains all the basic ingredients of real frictional systems, and it is useful to mimick their behavior. In fact, it includes both the interaction between the particles of the slider and between slider and substrate, together with the driving of the whole system. Moreover, the study of this 1D model allows us to introduce the procedure of MSM of sliding friction and to explain it starting from a test case.
Before the work of Pellegrini *et al.* [38], Markov State Modeling had been used to study non-equilibrium systems with just a few instances related to periodic driving [55] or cycle detection [26]. In [55], MSM has been used to study the conformational dynamics of alanine peptide under an oscillating electric field, while Reference [26] analyzes a driven particle in a double-well potential, coarse-graining space using cycles (defined as ordered sets of states at the end of which the starting state is reached again and no other state occurs twice). However, we are not aware of any example of the study of friction in a similar way to the one we proceed, using MSM.

The one-dimensional FK model, Figure 3.1(a), is made by a chain of particles dragged over a sinusoidal potential $V(x) = A\cos(2\pi x/a)$. The total number of particles is labeled by L, while $k$ is the stiffness of the spring coupling nearest-neighbors. $m$ is the mass of the particles, $x_i$ their positions and the spacing $a$ is commensurate with the periodic potential. Each particle is connected with a spring of constant $\kappa$ to a slider that moves with velocity $v_{ext}$.

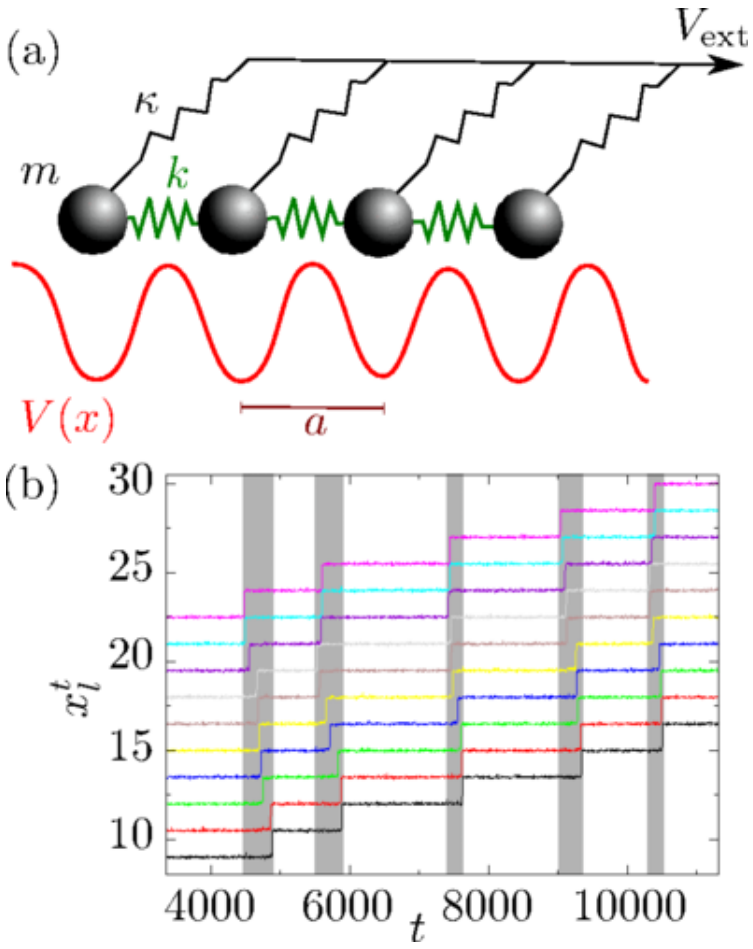


Figure 3.1: (a) Schematic of the FK system. (b) Sample of steady-state motion of $L = 10$ particles with parameters $k = 0.04$, $A = 0.1$, $a = 1.5$, $m = 1$, $\gamma = 1$, $\beta = 500$, $\kappa = 0.01$, and $v_{ext} = 0.001$. The white and gray backgrounds represent stick and slip time domains, respectively. From [38].

The dynamics is Langevin overdamped; the particles experience the effects of a bath with inverse temperature $\beta = 1/k_B T$ as in Equation 2.1, that we report below for simplicity:

$$x_l{}^{t+dt} = x_l{}^t + \left[\frac{2\pi A}{\gamma m a}\sin\left(\frac{2\pi x_l{}^t}{a}\right) + \frac{\kappa}{\gamma m}(v_{ext} - x_l{}^t) - \frac{k}{\gamma m}(2x_l{}^t - x_{l-1}{}^t - x_{l+1}{}^t)\right] dt + \sqrt{\frac{2dt}{\gamma m \beta}} f^t \ .$$

$f^t$ is harvested from an uncorrelated Gaussian distribution and $dt$ is the elementary time step. In Reference [38], the time step has been set to $dt = 10^{-2}$. As usual in the case of MSM, the analysis is based on a long MD simulation (about $10^6$ time units).
As described in Section 1.1.1 and Section 1.1.2, in a wide range of parameters the system experiences a stick-slip dynamics, during which long sticking periods during which the particles remain close to the potential minima alternate with rapid slip events responsible for the shift of the particles of one or more lattice spacings. When a slip event occurs, the chain is involved in large detours from the equilibrium configuration, which involve the formation of kink-antikink defects (see Section 1.1.2) that propagate along the chain and permit its motion. Figure 3.1(b) shows an example of the steady-state dynamics, focusing on the trajectory of each particle; the slip events are evident.

### 3.1.2 Choice of phase space metric

In the FK model, the metric includes internal variables, the bond lengths ${b_l}^t = ({x_{l+1}}^t - {x_l}^t - a)/a$, and an external variable, the center of mass coordinate (CM): ${x_{CM}}^t = \frac{1}{Na}\sum_{l=1}{}^{L} {x_l}^t$. As the authors explain, in the ideal situation one should consider a portion of the evolution long enough that all relevant events have occurred, then set "absorbing" boundary conditions for any such transition from and to the outside of this range, then averaging over many such equivalent stretches. In the alternative approach adopted by the authors in Reference [38], the absorbing conditions are substituted with artificially periodic boundary conditions, a choice which provides a more compelling picture of steady-state sliding, and where the error involved in the transition rates can be reduced at will by extending the portion size. The differences between the positions of the center of mass for two different configurations can be taken modulus $na$, for a chosen integer $n > 1$. If the driving is slow enough (as in [38]), the value $n = 2$ is sufficient to give a correct description of the slip events. In this way, the states divide into even and odd $x_{CM}$. If the driving velocity is increased, the system will experience more and more multiple slip events; in that case, a larger value of $n$ must be adopted. In conclusion, the metric adopted in [38] defines the distance between configurations at times $s$ and $t$ as:

$$d_{st} = \left[\frac{({x_{CM}}^s - {x_{CM}}^t)_{mod(2a)}}{2a}\right]^2 + \sum_{l=1}^{L-1}\left({b_l}^s - {b_l}^t\right)^2 . \tag{3.1}$$

This choice has the aim to be as unprejudiced and "blind" as possible. However, a unique recipe does not exist; similar results, with an analogous physical description, should appear with a different choice of the metric, as far as it is made with some physical insight.

### 3.1.3 Clustering analysis and Transition Matrix evaluation

Reference [38] analyzed samples of $10^5$ configurations, clustering them based on the metric defined in Equation 3.1, with the Density Peak (DP) clustering [47]. The number of clusters found is around $nc \simeq 100$. Once the algorithm has assigned a cluster index to all the configurations of the sample, the core-set analysis is exploited. Both DP algorithm and Pointwise-Adaptive-k-NN (PAk) provide the density (or, analogously, the free-energy) for all the points in the dataset. A threshold is defined for the free-energy, and for every cluster $i$ just the data that differ in free-energy from the cluster center less than the threshold value are considered. In this way, the microstates are more reliable, since they contain just points around the minimum, and the sampling around the saddle points between clusters is neglected. The points that have been disregarded are later reassigned to the last core set visited. In this way it is possible reducing the number of recrossings, and to

eliminate a bias in the evaluation of the time scales of the dynamics.
As previously stated in Section 2.3.2, once the microstates have been identified, a discrete transition matrix ${\Pi^\tau}_{\alpha\beta}$ is defined, where $\{c_\alpha\}$, $\alpha = 1, \ldots, n_c$ are the different microstates. This matrix is estimated by counting the jumps between clusters in the dynamics, normalizing the counts to get the probability.
As usual in MSM models, one has to determine the range of lag times that are long enough to obtain "markovianity", and thus a correct estimation of the dominant timescales. In order to do so, [38] evaluated the first non-trivial time scales $\tau_i$, $i > 1$ (since $\tau_1 = \infty$) as a function of the lag time $\tau$. From Figure 3.2 we see that the range of acceptable lag times is contained in $1 - 100$, as for that range of lag times the time scales show a plateau. In Reference [38] a lag time $\tau = 10 = 1000dt$ is adopted.

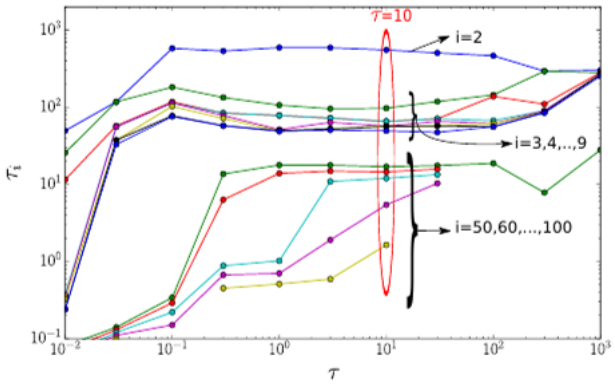


Figure 3.2: Timescales $\tau_i = 1/\log(\lambda_i)$ for some representative $i$ values (as labeled), as a function of the lag time $\tau$, obtained from the transition matrix of the clustering. Left: doubly logarithmic scale; right: linear scale in $\tau_i$. There is a clear plateau for all time scales $i \leq 60$ in the range $\tau \in [0.5, 50]$. From [38].

For the value of $\tau$ assumed, the finite time scales are $\tau_2 \simeq 600$ (see Figure 3.3, on top), separated by a gap from $\tau_3 \simeq 100$ and from other eigenvalues with shorter relaxation times.

### 3.1.4 Observables

From the diagonalization of the transition matrix $\Pi_{\alpha\beta}$ one derives eigenvalues and eigenfunctions. The eigenvectors $\{\chi_i\}$ allow us to describe the system studied in terms of the probability distribution $P(O)$ of an observable $O$ at time $t$, starting from a system prepared in the mixed state ${P_0}^\alpha$ (the probability to be in microstate $\alpha$ at $t = 0$). We have:

$$P(O) = P^{SS}(O) + \sum_{i>1} f_i g_i(O) e^{-t/\tau_i} \,, \tag{3.2}$$

where $f_i = \sum_\alpha {\chi_i}^\alpha {P_0}^\alpha / {P_{SS}}^\alpha$ accounts for the initial condition, and:

$$g_i(O) = \sum_\alpha {\chi_i}^\alpha P(O|\alpha) \,, \tag{3.3}$$

where $P(O|\alpha)$ is the probability distribution of $O$ in microstate $\alpha$, $P^{SS}(O) = g_1(O)$ the steady-state distribution of $O$, and ${P_{SS}}^\alpha$ the steady-state probability to visit microstate $\alpha$. The $g_i(O)$ for

$i > 1$ represent corrections to $P^{SS}(O)$, each decaying within the lifetime $\tau_i$.

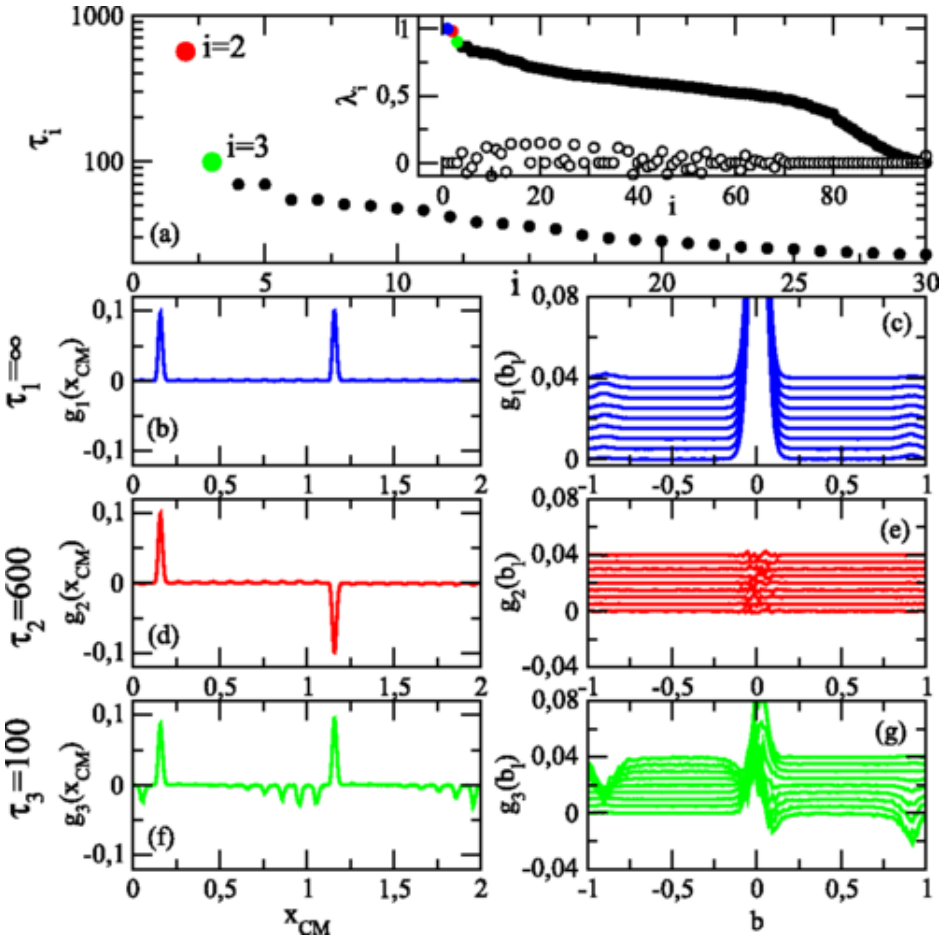


Figure 3.3: (a) Characteristic time scales and eigenvalues (in the inset, imaginary part in white) of the transition matrix (averaged over 10 realizations with $N = 10^5$ each). (b), (d), and (f) Probability distribution $g_1(x_{CM})$ and perturbations $g_i(x_{CM})$ for the first three eigenvectors of the transition matrix. (c), (e), and (g) These same functions for the bonds $b_l$, $g_i(b_l)$ (spaced vertically for clarity). From [38].

The functions $g_i$ provide a direct insight into the slow eigenmodes of the dynamics; the authors choose to analyze the components of the metric as shown in Figure 3.3.
Figure 3.3(b,d) and (f) shows $g_i(x_{CM})$: the steady state $\chi_1$ consists of one large peak per period plus nine smaller peaks. The first one is related to the chain at rest, while the others signal the presence of defects. The correction $g_2$ presents exactly the same features, except for a factor $-1$ in the second period: combining $g_1 \pm g_2$ one can obtain the chain sticking either in an odd or in an even position. Note that the corrections in Reference [38] have been presented up to a global sign and to a normalization constant, since the authors with the functions $g_i$ have been interested in showing the deviation from the steady-state distribution. We are going to adopt the same convention in the next sections. From the study of $g_2$ it is evident that this perturbation is responsible for the motion of the chain. In fact, passing from odd to even position is a hint of the advancing of the

chain, namely the slip. In fact, $\tau_2 \simeq 600$ is about half the sticking time, which is the jump time on average (see Figure 3.1, bottom).
Figure 3.3(c,e) and (g) shows the $g_i$ functions for the bonds lengths $b_l$, for $i = 1, 2, 3$. As already pointed out for the center of mass, the steady-state distribution $g_1$ describes the chain at rest with high peaks around the value 0, together with smaller ones around $b \simeq \pm 0.9$, signaling the occasional presence of some excitations, in the form of kinks and antikink. $g_2(b_l)$ shows a flat distribution: this means that this excitation does not differ from the steady-state for this observable, differently from the center of mass case. However, $g_3(b_l)$ exhibits both central peaks and lateral ones, which correspond to the creation (or the destruction, depending on the sign) of a kink or an antikink. In fact, lateral peaks are located around $b \simeq \pm 0.9$.
Because of the large number of microstates found, $n_c \simeq 100$, the authors decided to decrease the number with a further dimensional reduction: states recognized to be similar dynamically have been lumped together in the same macrostate. The method adopted is the (Robust) Perron Cluster Cluster Analysis (PCCA+). We are not presenting here further details for this technique; more information can be found in [12,56]. At the end of this analysis the number of states have reduced from $n_c \simeq 100$ to $\tilde{n}_c = 6$. Figure 3.4(a) shows the six macrostates $\{\tilde{c}_\alpha\}$, together with some of the configurations belonging to them. $\tilde{c}_1$ and $\tilde{c}_4$ represent both states in which the chain is at rest or shows at single excitations. $\tilde{c}_2$ and $\tilde{c}_5$ contain mostly single kinks, while $\tilde{c}_3$ and $\tilde{c}_6$ mostly antikinks. The microstates with (kink, antikink) pairs are spread between groups, with neighboring pairs belonging to $\tilde{c}_{1,4}$ and extended pairs to others. The only difference between macrostates $\tilde{c}_{1,2,3}$ and macrostates $\tilde{c}_{4,5,6}$ is the value of the center of mass, which is $x_{CM} \approx 0.15$ and $x_{CM} \approx 1.15$. Figure 3.4(b) shows the reduced transition matrix $\tilde{\Pi}_{\alpha\beta}$ between macrostates. The reader can note that in order to move between $\tilde{c}_1$ and $\tilde{c}_4$ the system must pass through the other states, namely $\tilde{c}_{2,3,5,6}$.

### 3.1.5 Conclusions and comments

From the analysis in Reference [38] here mentioned, one concludes that MSM can be employed to treat sliding friction, in particular the Frenkel-Kontorova system here reported. This contribution is fundamental for a branch in which a systematic theoretical approach is still missing, especially at a nanoscale level. Moreover, the method does not only give information on the average behavior of the main physical quantities in the steady-state, but it allows also the analysis of the slow modes of excitations, as shown with the functions $g_i$.

## 3.2 1D incommensurate Frenkel-Kontorova model

### 3.2.1 The model

As asserted previously in Section 1.1.2, a particular role in friction is played by the incommensurability. Incommensurability in a FK model means that the harmonic equilibrium distance $a_c$ and the substrate lattice spacing $a_b$ are irrationally mismatched. When this happens, the model admits the presence of a phase transition in the thermodynamic limit, named *Aubry transition* [42]. When the ratio $a_b/a_c$ is irrational, the system presents areas characterized by approximate commensurability in which the slider and the substrate tend to lock, separated by defects (kinks or antikinks). The transition occurs for a certain value of the harmonic coupling $K_c$ between nearest neighbors. Above $K_c$ there exist a continuum set of ground states which can be reached adiabatically by the chain of particles through non-rigid displacements of the atoms and at no energy cost: this regime is called *superlubric*. In this condition the system can move smoothly, experiencing no static friction. On the other hand, for $K < K_c$, the atoms are confined close to the minima of the substrate

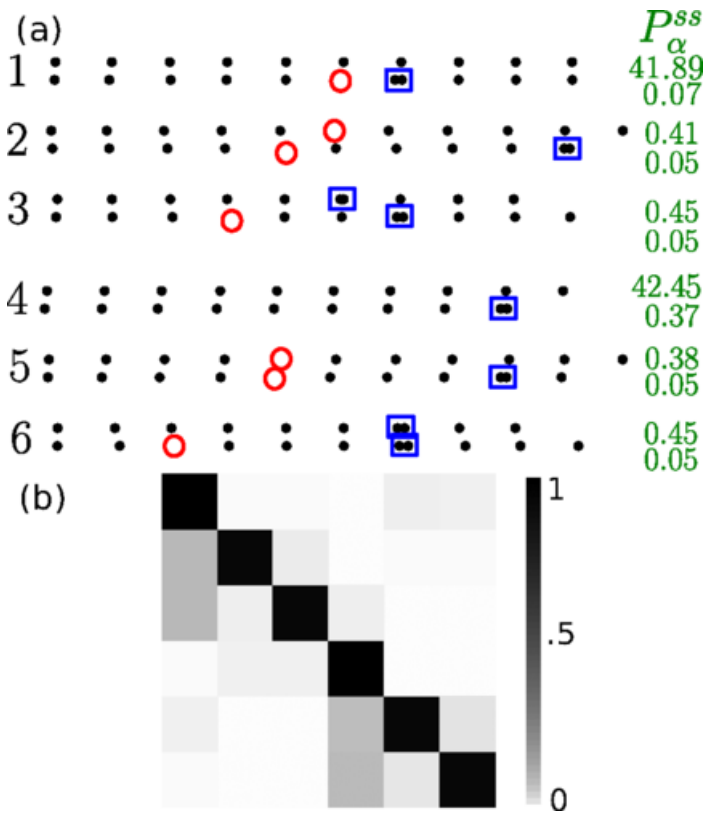


Figure 3.4: (a) Selection of microstates inside the six macrostates identified with PCCA+: the atoms positions relative to potential minima (black dots) display kinks (red circles) and antikinks (blue squares). For clarity, the probability ${P_\alpha}^{SS}$ is multiplied by 100, and only 12 of the $\sim$ 100 microstates are shown. (b) Representation of the reduced transition matrix $\tilde{\Pi}_{\alpha\beta}$ (gray scale proportional to magnitude). From [38].

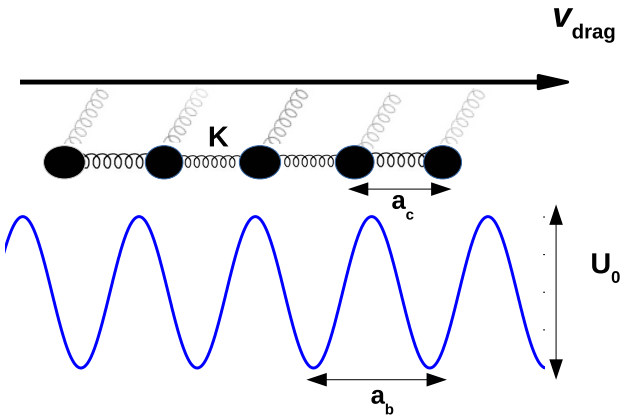


Figure 3.5: Sketch of the one-dimensional incommensurate Frenkel-Kontorova model. Here, $K$ is the stiffness of nearest-neighbor springs, $U_0$ the amplitude of the cosinusoidal potential, $\kappa$ the stiffness of the springs dragging each particle with velocity $v_{drag}$, $a_c$ the harmonic equilibrium distance and $a_b$ the lattice spacing of the cosinusoidal potential.

potential. In this case a barrier must be overcome (called Peierls-Nabarro barrier, [54]), in order to move the chain. The dynamics in this phase is a stick-slip one. For finite-size, the FK model is always pinned, but the pinning barrier changes from small to large across the Aubry transition. The critical value $K_c$ depends dramatically and discontinuously from the ratio $a_b/a_c$, assuming the minimal possible value for $a_b/a_c = (1+\sqrt{5})/2$ [54].
Moreover, one can identify two different conditions: $a_b/a_c < 1$ describes a system in which the number of minima of the substrate is smaller than the number of particles, vice versa for $a_b/a_c > 1$. We indicate the "excess" of mass of the former as *overdense case*, the latter as *underdense case*. Typically, in the overdense regime the excitations are kinks, and antikinks in the underdense case. After the commensurate case treated in Reference [38], we have analyzed also the 1D incommensurate FK model; a sketch of the system is provided in Figure 3.5. We simulate $N = 10$ particles of mass $m$ with a dynamics described by the Hamiltonian in Equation 1.6:

$$\hat{H}(t) = \sum_i \left[ \frac{{p_i}^2}{2m} + \frac{K}{2}(x_{i+1} - x_i - a_c)^2 + \frac{U_0}{2}\cos\left(\frac{2\pi x_i}{a_b}\right) + \frac{\kappa}{2}(x_i - v_{drag}\cdot t)^2 \right] ,$$

where $K$ is the stiffness of nearest-neighbor springs, $U_0$ the amplitude of the sinusoidal potential, $\kappa$ the stiffness of the springs dragging each particle with velocity $v_{drag}$, $a_c$ the harmonic interparticle equilibrium distance between two nearest-neighbor particles and $a_b$ the lattice spacing of the sinusoidal potential. In the present case, the incommensurability is $a_b/a_c = 1.6$ (overdense regime, close to the golden mean $a_b/a_c = (1+\sqrt{5})/2$). The other parameters are $U_0 = 0.1$, $k_BT = 0.04$, $\gamma = 1$, $\kappa = 0.01$ and $v_{drag} = 0.001$.
The simulation is carried out using an MD code that I have written: it performs Langevin dynamics. In order to generate the initial conditions, we start from a chain with the particles in equilibrium with respect to the harmonic interparticle distance, and we displace them slightly afterwards (in a random way) from that position. This choice allows us to speed up the initial thermalization, with respect to a chain with all the springs set at the equilibrium harmonic distances. No boundary conditions are implemented in the code: the chain continues to move in the drag direction, sliding on the infinite substrate until the end of the simulation.

To investigate the superlubric/pinned behavior of the incommensurate FK we compute the static friction force needed to depin the system for different values of the spring constant $K$, as in Figure 3.6.

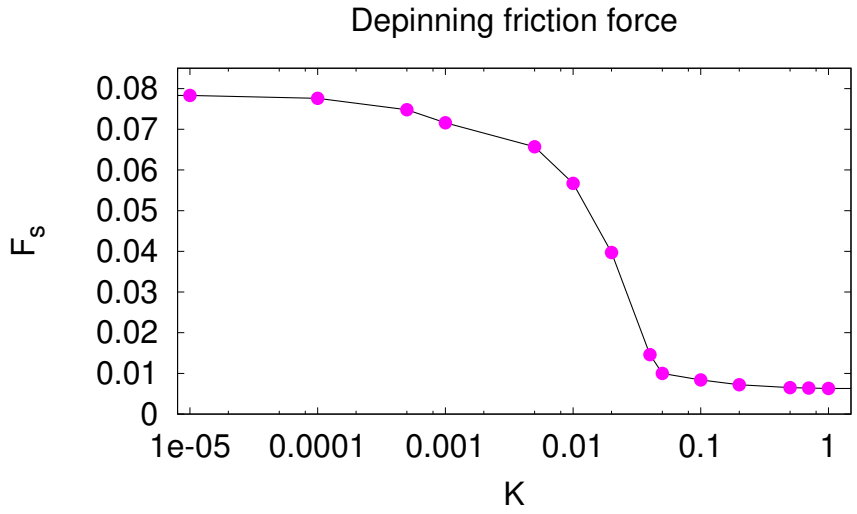


Figure 3.6: Static friction force for depinning the incommensurate one-dimensional FK model.

For a chain of finite length, the truly superlubric regime is not present, and we can only distinguish a superlubric-like regime ($K/U_0 \gg 1$) with small static friction from a pinned regime with large one ($K/U_0 \ll 1$). The measure of the depinning force in Figure 3.6 shows quite a rapid transition from a pinned-like regime to a superlubric-like one around $K \simeq 0.07$, meaning $K/U_0 \simeq 1$.
The most interesting values of $K/U_0$ are those near the transition. Hence, we decide to focus on $K/U_0 = 0.3$ ($K = 0.03$ in Figure 3.6) and $K/U_0 = 0.05$ ($K = 0.005$ in Figure 3.6): the first is above the transition identified at $K \simeq 0.07$, while the second is just below. Examples of the simulated trajectories for the cases under study are shown in Figure 3.7. The lines with different colors represent the trajectories of the 10 particles of the chain. The offset in the $y$ direction is arbitrary. The black dashed line underlining the particle trajectories represents the linear superlubric limit.

### 3.2.2 Choice of phase space metric

As in the case of the commensurate one-dimensional FK model, our aim is to identify a metric which is as little prejudiced as possible. In order to do so, we again take into account the particles positions relative to the potential, and the distances between neighbor particles. The positions are divided by twice the lattice spacing ($2a_b$); the distances have been normalized by the harmonic equilibrium distance. Given two different configurations at time $s$ and $t$, their distance is defined as:

$$d_{st} = \sum_{l=1}^{N} \left[ \frac{\left({x_i}^s - {x_i}^t\right)_{mod(2a_b)}}{2a_b} \right]^2 + \sum_{l=1}^{N-1} \left({h_l}^s - {h_l}^t\right)^2 , \tag{3.4}$$

where ${h_l}^t = ({x_{l+1}}^t - {x_l}^t)/a_c$.

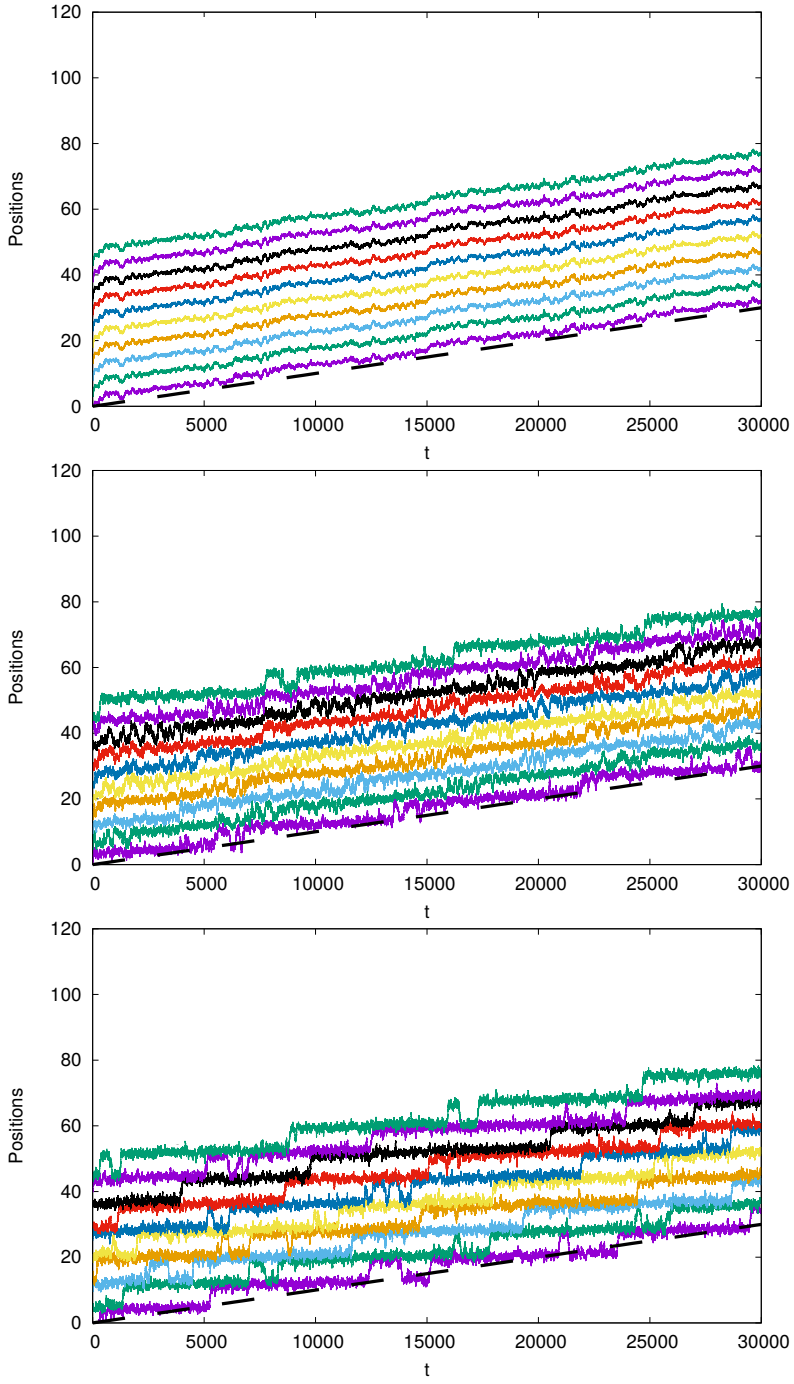


Figure 3.7: One-dimensional FK model. The plot on top refers to the condition $K/U_0 \gg 1$: the effect of the substrate is minimal, and the trajectories show an almost linear sliding. We remind to the reader for finite-size case the friction does never go exactly to zero, and a bit of stick-slip is always present. The second and third figure represent the $K/U_0 = 0.3$ case and the $K/U_0 = 0.05$ one. This two cases are the ones under study: the first one shows mostly a linear sliding, with some sporadic slip, while in the second the slip events are much more frequent. The lines with different colors represent the trajectories of the 10 particles of the chain. The offset in the $y$ direction is arbitrary. The black dashed line represents the linear superlubric limit.

### 3.2.3 Clustering analysis and Transition Matrix evaluation

We have analyzed samples with $6 \times 10^4$ configurations, obtained from a single long MD simulation. clustering them based on the metric define in Equation 3.4, with DP clustering [47]. For $K/U_0 = 0.3$ we have obtained 475 clusters, while for $K/U_0 = 0.05$ we have obtained 433 clusters. The core-set analysis has not been performed in this case. Once the microstates have been identified, a discrete transition matrix $\Pi_{\alpha\beta}$ is built up as discussed in Section 3.1.3. For this system, the study of the first few time scales as a function of the lag time $\tau$ has not been performed. For small values of $\tau$, the main problem is data correlation, while for large values it is poor sampling. For this system with a non-particularly exotic dynamics we have been able to perform long simulations, ensuring enough sampling. However, to have a clear idea on the error for the time scales, this type of analysis would be necessary. A lag time of $\tau = 300$ is assumed: this choice allows us to sample every sticking period of our trajectories at least 10 times. The value of $\tau$ is the same for both the cases under study. In Figure 3.8, we show the eigenvalues for the two cases under study. Timescales can be found from $t_i = -\tau/\log(\lambda_i)$. The first three eigenvalues have been highlighted: the steady-state eigenvalue $\lambda_1$ corresponding to $\tau_1 = \infty$ in blue, $\lambda_2$ in red and $\lambda_3$ in green. For the finite timescales we find $\tau_2 \sim 980$ and $\tau_3 \sim 250$ for $K/U_0 = 0.3$. Here a gap exists between the first three eigenvalues and the others. For $K/U_0 = 0.05$ instead, no clear gap is present. For this regime we find $\tau_2 \sim 1100$ and $\tau_3 \sim 380$.

### 3.2.4 Observables

Using Equation 3.2 we can estimate the probability distribution of any observable $O$. In Figure 3.9 we show the steady-state distributions for the nearest-neighbor distances, while in Figure 3.9 we show the steady-state distributions for particle positions. In the following plots for the positions, we have decided to picture them with a range in the abscissa going from 0 to $a_b = 8$, and not to $2a_b$. For both, $K/U_0 = 0.3$ is on the left, while $K/U_0 = 0.05$ is on the right. With a stiffer spring constant, in the $K/U_0 = 0.3$ case the chain spring tends to keep the particles at a certain fixed distance. In fact the main peak is around $b \simeq 1$ (meaning particle distance close to $a_c$). For $K/U_0 = 0.05$ instead, a looser spring causes the presence of two peaks tending to the limiting value for distances that we expect from an infinite chain in the overdense regime: a first one corresponding to $b \simeq 0$, while the other one to $b \simeq 1.6$, namely, in $a_c$ units, the substrate period distance. Differently from its commensurate counterpart, in fact, for incommensurate FK model no state exists in which both the harmonic and the potential part of the energy are at their minimum. Being stuck in the minima of the potential, particles will have a distance from the neighbors different from the equilibrium one. In particular, in the overdense case like the one here studied, there will always be more than one particle per minimum. For this reason, when the effect of the potential is strong as for $K/U_0 = 0.05$, neighbor particles gets stuck either in the same minimum or in successive ones.
In the $K/U_0 = 0.3$ case the distributions of positions are really broad, suggesting the equivalence of positions along the substrate of a superlubric-like regime. In the superlubric limit, in fact, every position is equally probable. Moreover, positions seem to be in phase, again suggesting that the particles keep a certain relative distance. For $K/U_0 = 0.05$, positions are peaked, and coherent, in the middle between two maxima. This is a clear hint of a pinned behavior.

Figure 3.10 shows the first excited state distributions of nearest neighbors distances for $K/U_0 = 0.3$ and $K/U_0 = 0.05$ (at the top and bottom respectively). Differently from the results shown in Section 3.1.4, we have decided not to show the corrections of the excited states $g_i$, $i > 1$ (see Section 2.3.2), to the steady-state distributions, but the positive/negative superpositions $P^{SS} \pm c_2\chi_2$, since they turned out to be more clear. $P^{SS}$ is the steady-state probability distribution, $\chi_2$ the

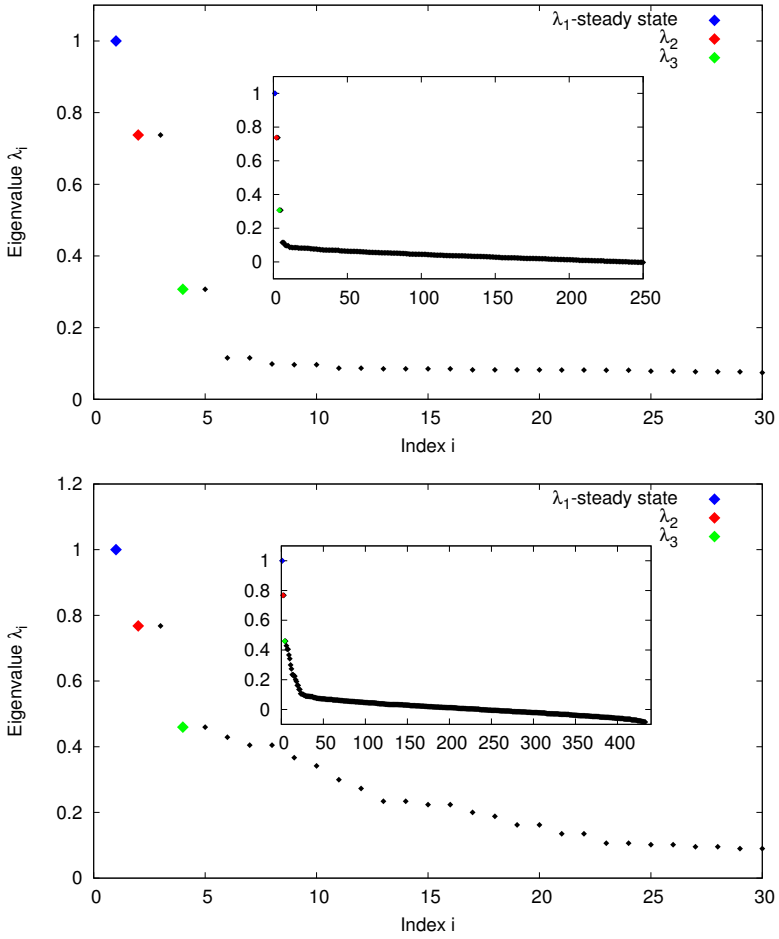


Figure 3.8: One-dimensional incommensurate FK model, eigenvalues for the two cases under study. At the top, $K/U_0 = 0.3$, while at the bottom $K/U_0 = 0.05$. The first three eigenvalues have been highlighted: the steady-state eigenvalue $\lambda_1$ corresponding to $\tau_1 = \infty$ in blue, $\lambda_2$ in red and $\lambda_3$ in green. In the insets, the whole spectrum is shown.

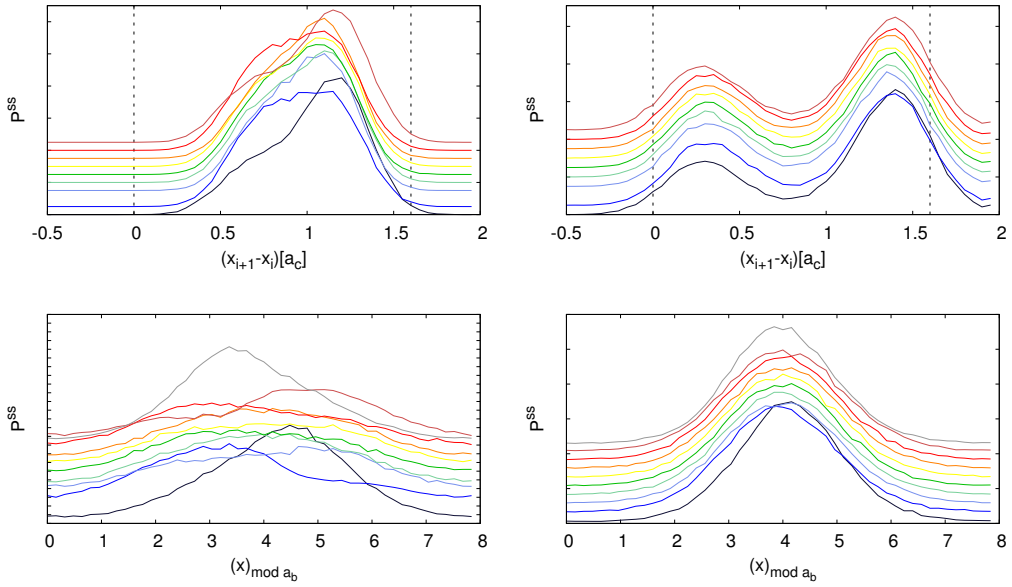


Figure 3.9: One-dimensional incommensurate FK model. Top: the steady-state distribution for nearest-neighbor distances ($K/U_0 = 0.3$ on the left, $K/U_0 = 0.05$ on the right). The different colored lines identify the different bonds between nearest neighbor particles; the offset in the y direction is arbitrary. The two dashed lines highlight the bond with zero length and the one with length $a_b$ (in fact, $a_b$ equals 1.6 in $a_c$ units), the substrate period distance. Bottom: the steady-state distribution for particle positions ($K/U_0 = 0.3$ on the left, $K/U_0 = 0.05$ on the right). The different colored lines identify the different particles; the offset in the y direction is arbitrary. Note that the x range for the particle positions goes from $x = 0$ to $x = a_b = 8$ in these plots.

left eigenvector of the transition matrix, and $c_2$ is a constant that has been chosen as: min $\left[\frac{P^{SS}}{|\chi_2|}\right]$. We have chosen as coefficient of the linear combination the smallest ratio between $P^{SS}$ and $\chi_2$ in order to have a positive distribution when combining $P^{SS} \pm c_2\chi_2$.
Concerning the first slow mode, for $K/U_0 = 0.3$ the tendency of particles to stay at the harmonic equilibrium distance is preserved but some deviations start to show up. For the $K/U_0 = 0.05$ case instead, we can easily guess which couples of neighboring particles belong to the same minimum and which one belong to two different successive minima.

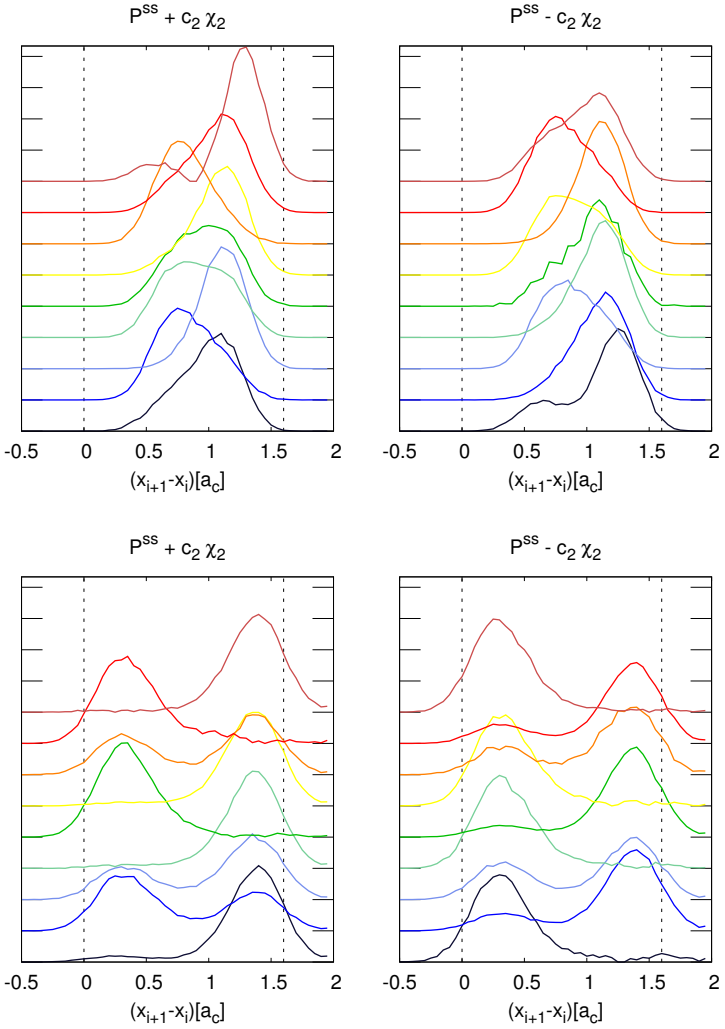


Figure 3.10: One-dimensional incommensurate FK model, first excited state positive/negative superposition $P^{SS} \pm c_2\chi_2$ for nearest-neighbor distances; $K/U_0 = 0.3$ at the top, $K/U_0 = 0.05$ at the bottom. Note that the x range for the particle positions goes from $x = 0$ to $x = a_b = 8$ in these plots.

In Figure 3.11 we show the positive/negative superpositions $P^{SS} \pm c_2\chi_2$ (averaged over the 10

particles of the chain) for particle positions. We see that in the $K/U_0 = 0.05$ case (red) the peak is less broadened and goes to zero for $x \to 0$ or $x \to a_b = 8$. This means that particles are "trapped" into the substrate minima, while for $K/U_0 = 0.3$ the broad peak again suggests the equivalence of positions along the substrate.

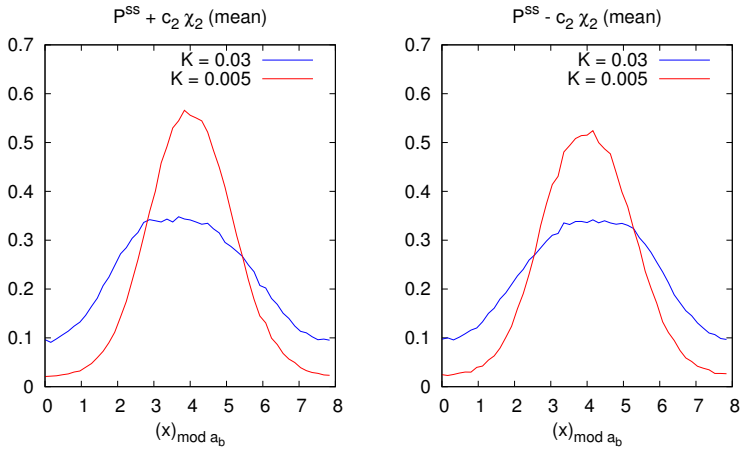


Figure 3.11: One-dimensional incommensurate FK model, first excited state positive/negative superposition $P^{SS} \pm c_2\chi_2$ (average) for particle positions ($K/U_0 = 0.3$ in blue, $K/U_0 = 0.05$ in red).

### 3.2.5 Conclusions and comments

In this section we have presented an MSM analysis for a one-dimensional incommensurate Frenkel-Kontorova model. Incommensurability implies the presence of a phase transition in the FK model, between a superlubric regime with zero friction and a pinned regime. Even if the finite-size of the chain does not allow a real phase transition to the superlubric limit, the differences in the two regimes examined are evident.
Moreover, incommensurability enriches the heterogeneity of the possible configurations that the chain can visit, because of the permanent unsatisfaction of either the harmonic or the potential part of the system.
The method implemented allows us to discover the slow excitations of the system; we describe the slowest one in Figure 3.10 using the nearest-neighbor distances between particles. This excitation consists, for the smooth sliding regime $K/U_0 = 0.3$, in a collective movement of the whole chain when proceeding of one lattice spacing: in fact, the nearest-neighbor distance is not affected by the slip. This is a result of the smooth sliding for a superlubric-like regime in which all the positions are equivalent. On the contrary, the case $K/U_0 = 0.05$ shows the particles either at distance zero or $a_b$. This means that the sliding is a stick-slip in which the slip events bring two neighbor particles either in the same minimum or in next minima. The effect of the potential is strong, conditioning the particles of advancing of multiples of the lattice spacing $a_b$.
Finally, we would like to mention the fact that, for this intermediate test, even if the total number of clusters found for each regime was large, we have not performed the PCCA+ analysis to further decrease their number.

## 3.3 2D incommensurate Frenkel-Kontorova model

### 3.3.1 The model

After the study of the 1D commensurate and incommensurate Frenkel-Kontorova model, we decided to increase the dimension of the system to 2D. In this way, we can make an intermediate step from the case of a 1D chain, towards a more realistic system with triangular symmetry. This study has been published in [50]. See Section 1.1.3 for further details. The system is an hexagonal-shaped "sliding island" composed of $N = 1027$ classical particles held together by harmonic forces, to form a triangular lattice as shown in Figure 3.13(a), 19 for each side. The center of mass is coupled by a spring of constant $\kappa$ to a dummy tip which drags it with constant velocity $v_{ext}$, so that the full Hamiltonian reads (as in Equation 1.7:

$$H(t) = \sum_i \left[ \frac{\mathbf{p}_i^2}{2m} + \frac{K}{2}(\mathbf{r}_{i+1} - \mathbf{r}_i - a_H)^2 + V(\mathbf{r}_i) + \frac{\kappa}{2}(x_{CM} - v_{ext} \cdot t)^2 \right] .$$

In the equation above, $\mathbf{r} = (x, y)$, $m$ is the particle mass, $a_H$ the harmonic equilibrium distance and the potential $V(\mathbf{r})$ has the form in Equation 1.8:

$$V(x, y) = U_0 \left[ 2\cos\left(\frac{2\pi}{a_S}x\right)\cos\left(\frac{2\pi}{a_S}\frac{y}{\sqrt{3}}\right) + \cos\left(\frac{4\pi}{a_S}\frac{y}{\sqrt{3}}\right) \right] ,$$

where $a_S$ is the substrate lattice spacing. The two main lengths of the system are slightly incommensurate, being their ratio $a_S/a_H \sim 1.07$. This value has been chosen to study what happens with a minimal deviation from commensurability. In principle, every couple of mismatched values for $a_S$ and $a_H$ could be choen to obtaining incommensurability. In our case, we decided to adopt $a_S = 15$ and $a_H = 14$ in order to have a lattice spacing of the moiré pattern comparable with the size of the hexagonal island. Further details about the moiré pattern will be discussed within this paragraph.
Particle motion obeys an overdamped Langevin dynamics, in a bath of inverse temperature $\beta = 1/k_B T$, like in Equation 2.2:

$$\mathbf{r}_l{}^{t+dt} = \mathbf{r}_l{}^t + \left[ \frac{1}{\gamma m}\nabla V(\mathbf{r}_l{}^t) + \frac{\kappa}{\gamma m}\left( v_{ext}t - \frac{1}{N}\sum_j x_j{}^t \right) - \frac{K}{\gamma m}\sum_{j \in NN} \left(\mathbf{r}_l{}^t - \mathbf{r}_j{}^t\right) \right] dt + \sqrt{\frac{2dt}{\gamma m \beta}}\mathbf{f}^t ,$$

where $\mathbf{f}^t$ is harvested from an uncorrelated Gaussian distribution and $dt$ is the elementary time step. We choose the following set of parameters: $dt = 0.1$, $m = 1$, $\gamma = 1$, $\beta = 100$, $\kappa = 0.01$, and $v_{ext} = 0.0001$.
The simulation is carried out using an extension to 2D of the MD code written for the simulations described in Section 3.2, performing Langevin dynamics. In order to generate the initial conditions, we start displacing the particles of the 2D island in a pattern with triangular symmetry, one for each of the minima of the potential. The center of mass of the island is pulled by the spring, and the initial thermalization needed to overcome the static friction and unpin the island from the substrate is not considered in the analysis. No boundary conditions are implemented in the code: the island continues to move in the drag direction, sliding on the infinite substrate until the end of the simulation.
In a temperature and parameter regime where the island does not rotate, its sliding mechanics retains some similarity to 1D sliding. In the weak potential limit, the bulk of the island is characterized by the presence of solitons (small deviations of the interparticle distance from the equilibrium

value) which create a moiré pattern over the incommensurate potential. In these conditions, the dynamics is superlubric [29,54]. Moiré patterns show the interference caused by the superposition of two similar patterns, for example when two similar geometries are shifted or tilted with respect to each other by an angle. In our case, the two different geometries are the triangular one of the FK island sliding and the one of the substrate, which has itself a triangular symmetry, but where the two lattice spacings are slightly mismatched; in our case $a_S/a_H \sim 1.07$. In fact, in order to obtain the interference typical of a moiré pattern, the two overlapping lattices must not be exactly identical. This is exactly the case of our 2D Frenkel-Kontorova model.
Upon sliding in this regime, the solitons flow unhindered, and the only source of pinning and static friction is actually provided by the island edge. In the opposite strong potential limit, the solitons, no longer weak, are strongly entrenched, and the whole island is pinned, with a bulk static friction independent of edges. In Figure 3.12 an example of the passage of two solitons through the island is shown. Depending on the ratio $K/U_0$, in our simulations we can have configurations with either one soliton or two.

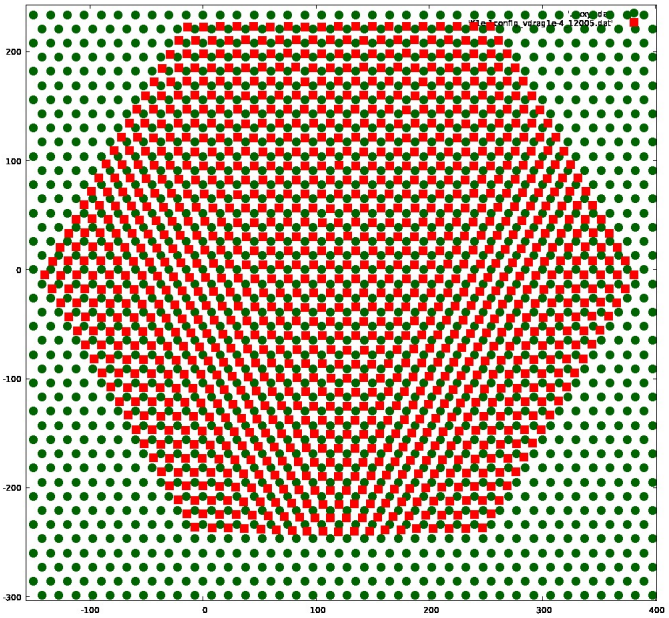


Figure 3.12: Two-dimensional incommensurate FK model, moiré pattern of the island showing the presence of two solitons ($K/U_0 = 0.5$). See text for more details.

Under the external spring force, the island sliding in this regime will alternate long "sticking" periods during which particles are close to their respective potential minima, to fast slips during which one or more lattice spacings are gained. A slip event always involves the flow of either pre-existing solitons or of newly created ones that enable the system to slide faster. Our input for the MSM procedure is a long steady-state trajectory of the island motion, obtained by integrating these equations for $\sim 10^8$ time steps for a slow external velocity. Values of $K/U_0$ were chosen so as to straddle between and beyond the weak ($K/U_0 \geq 2$) and strong ($K/U_0 \leq 0.2$) potential regimes. The average friction force:

$$F_{mean} = \kappa \langle v_{ext} t - \frac{1}{N} \sum_l x_l \rangle \ , \tag{3.5}$$

obtained from the simulation as a function of the ratio $K/U_0$ can be seen in Figure 3.13(b), where the crossover from a superlubric to a pinned regime is evident. We focus our study on three different values of the parameters representative of these different regimes (the three colored arrows in Figure 3.13(b)), as can be grasped by looking at the evolution of the position of the center of mass shown in Figure 3.13(d).

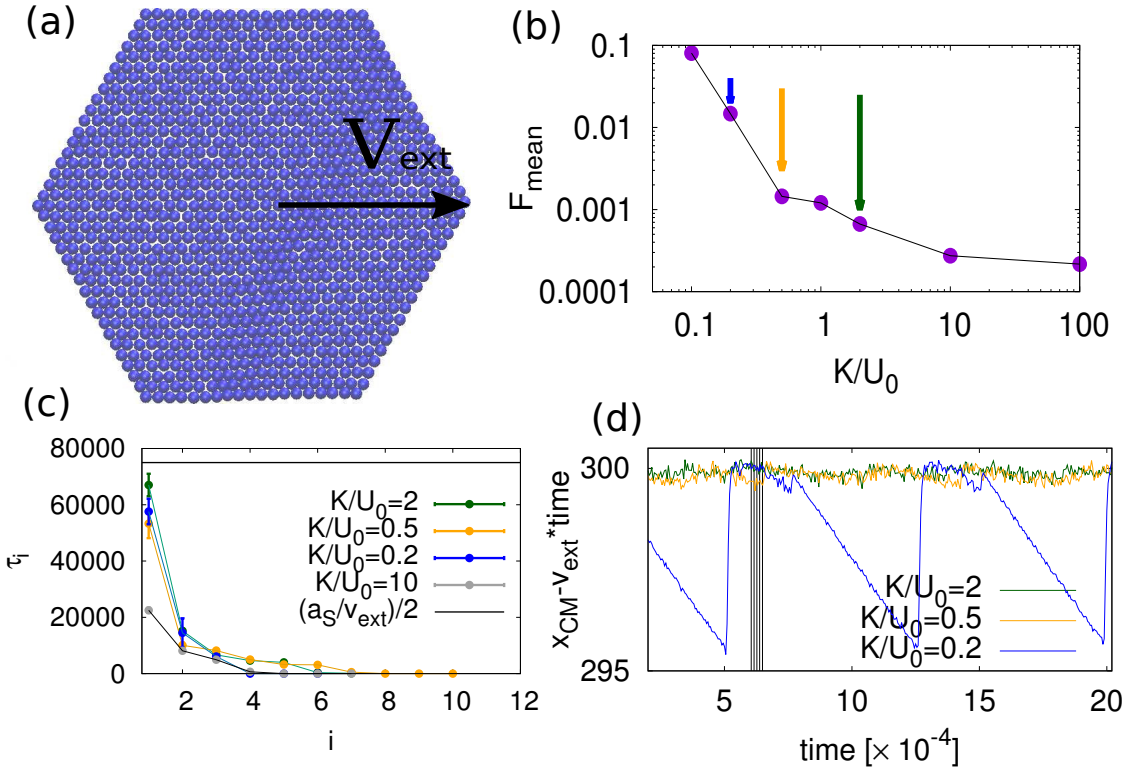


Figure 3.13: Two-dimensional incommensurate FK model. (a) Schematic of the FK island sliding on a generic 2D incommensurate triangular potential. (b) Average friction force in the steady state regime for simulations with varying ratio $K/U_0$, highlighting the transition from free sliding to stick-slip. The arrows indicate the sample parameters chosen to compare the results of our method, with a color code which we will keep throughout for all figures. (c) Slowest time scales after transition matrix diagonalization for the different regimes. The full line represents half of the time required for the external force to move the particles to successive potential minima. (d) Sample evolution for the different regimes: we show the deviations of the center of mass positions from the free sliding corresponding to an infinitely stiff island. The vertical dashed lines are spaced like the time lag $\tau = 1100$ chosen to build the MSM to represent sampled configurations.

### 3.3.2 Choice of phase space metric

As usual, the protocol begins by defining a metric, measuring distances between configurations in phase space. Since we want to remain as unprejudiced as possible, we adopt the simplest, most generic and bias-free metric, and define the distance between two configurations $s$ and $t$ as:

$$d_{st} = \left[ \left( {\mathbf{r}_{CM}}^s - {\mathbf{r}_{CM}}^t \right)_{mod(2a_S)} \right]^2 + \left[ \sum_{l=1}^{N} \left( {\mathbf{r'}_l}^s - {\mathbf{r'}_l}^t \right)^2 \right] , \tag{3.6}$$

where ${\mathbf{r'}_l}^s = {\mathbf{r}_l}^s - {\mathbf{r}^s}_{CM}$ is the relative position of the $l$-th particle with respect to the center of mass of the configuration $s$.

### 3.3.3 Clustering analysis and Transition Matrix evaluation

We have analyzed samples constituted by $\sim 10^4$ configurations, clustering them based on the metric defined in Equation 3.6, with DPA [11, 46] (see Section 2.2.4). This is a variant of DP clustering, employing a new unsupervised density estimator able to identify just the real minima of the free-energy. This method is non-parametric: it shares the same idea of k-Nearest Neighbor clustering algorithm, but this time the value $k$ labeling the neighborhood around a point is computed iteratively, and an optimal $k$ value is identified for each of the points. Moreover, the error on the value of the density is computed, allowing to distinguish between real peaks and spurious ones.
Note that the employment of PAk automatically reduces the number of clusters, as this algorithm is able to identify the minima of the free energy, decreasing drastically $n_c$ and rendering the use of PCCA+ further analysis not compulsory. The three regimes studied are: $K/U_0 = 2$, $K/U_0 = 0.5$ and $K/U_0 = 0.2$. The number of clusters found is: $n_c = 16$ for $K/U_0 = 2$, $n_c = 13$ for $K/U_0 = 0.5$ and $n_c = 9$ for $K/U_0 = 0.2$. Once the algorithm has assigned a cluster index to all the configurations of the sample, the core-set analysis is performed. PAk provides the density (or, analogously, the free-energy) for all the points in the dataset. It is then possible to define a threshold for the free-energy, and include in every cluster $i$ just the data that differ in free-energy from the cluster center less than the threshold value. In this way, the microstates are more reliable, since they contain just points around the minimum. The points that have been disregarded are later reassigned to the last core set visited. In this way it is possible to avoid counting a lot of recrossings, and to eliminate a big bias in the evaluation of the time scales of the dynamics.
Once the microstates have been identified, a discrete transition matrix $\Pi_{\alpha\beta}$ is defined, where $\{c_\alpha\}$, $\alpha = 1, \ldots, n_c$ are the different microstates obtained. From the diagonalization of the transition matrix we obtain the eigenvalues $\{\lambda_i\}$; from those, due to the relation $\tau_i = -\tau / \log(|\lambda_i|)$ we can identify the typical time scales of the dynamics of the system studied. $\tau$ is the lag time between two successive configurations. Since $\Pi_{\alpha\beta}$ depends on the lag time $\tau$, we have studied the variation of the three longest finite time scales, for the three different regimes, as shown in Figure 3.14. The optimal lag time has been set to $\tau = 1100$. In particular, we have verified that the relevant time scales stay within the statistical error in Figure 3.13 when doubling or halving the lag time.
We apply the procedure described above to three evolutions of our model characterized by different parameters $K/U_0$ as indicated in Figure 3.13(b). The time corresponding to the first largest eigenvalue is shown in Figure 3.13(c): for all cases, we find that the first implied time scale is approximately equal to $6 \times 10^4$, corresponding to roughly half the time $a_S/v_{ext}$ required on average to move by one lattice spacing. This is consistent with the interpretation of the slowest mode as being related to the movement from one local minimum of the substrate to the next. We notice that in the more extreme case $K/U_0 = 10$ the first relaxation time is much faster; since the island

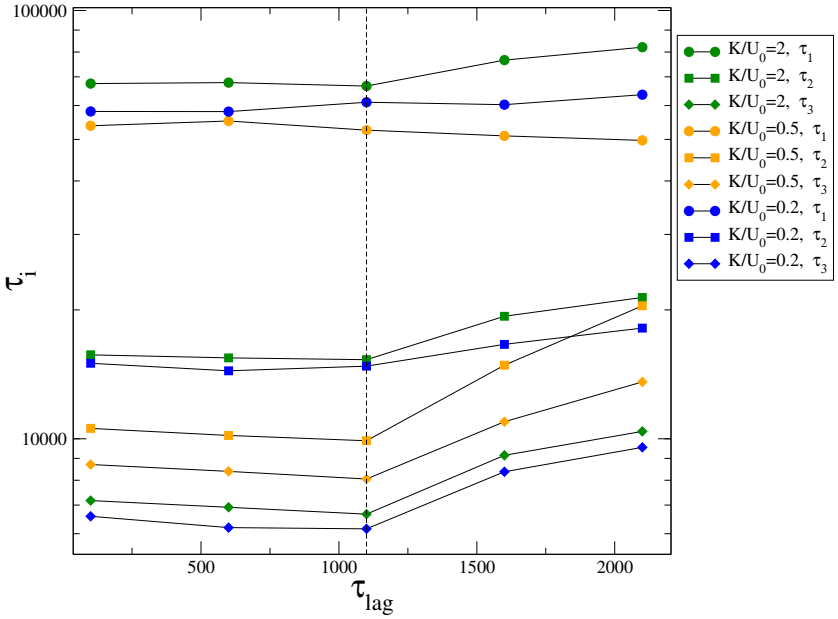


Figure 3.14: Two-dimensional incommensurate FK model. Convergence of the three timescales $\tau_{1,2,3}$ of the longest-lived slow modes, for the different regimes: $K/U_0 = 2$ in green, $K/U_0 = 0.5$ in yellow and $K/U_0 = 0.22$ in blue, respectively.

is stiff, the substrate does not play a primary role. The successive time scales are almost an order of magnitude smaller, and further insight is required for their interpretation.

### 3.3.4 Observables

We will now analyze the $g_i$ functions (see Section 2.3.2) of some relevant physical observables of this frictional system, in order to characterize the long-lived states we have identified.

#### Nearest-neighbor distance

As a first observable, we consider the nearest-neighbor distance between all particle pairs. The steady-state distributions (see Figure 3.15(a)) show the expected trend: while the $K/U_0 = 2$ case probability has a peak centered on the harmonic equilibrium distance reflecting the nature of the hard island during structurally lubric sliding, the one for the opposite case $K/U_0 = 0.2$ is centered on a distance commensurate with the substrate, reflecting the adhesion of the soft island to the external potential. For $K/U_0 = 0.5$, the situation is intermediate. The excited states complete this description (see Figure 3.15(b)): the first excited states show little correction to the steady-state distribution, as the change of a whole lattice spacing has only a minor influence on the nearest-neighbor distribution, while the second and third excited states display a significant change. Indeed, the latter corresponds to internal relaxations of the island not associated with the collective sliding. In the specific case, these corrections are related to the formation/destruction of incommensurate solitons induced on the island by the external potential. This observable lacks the ability to clearly distinguish between the excited states. In the following, we therefore considered a more extensive observable, able to highlight more differences.

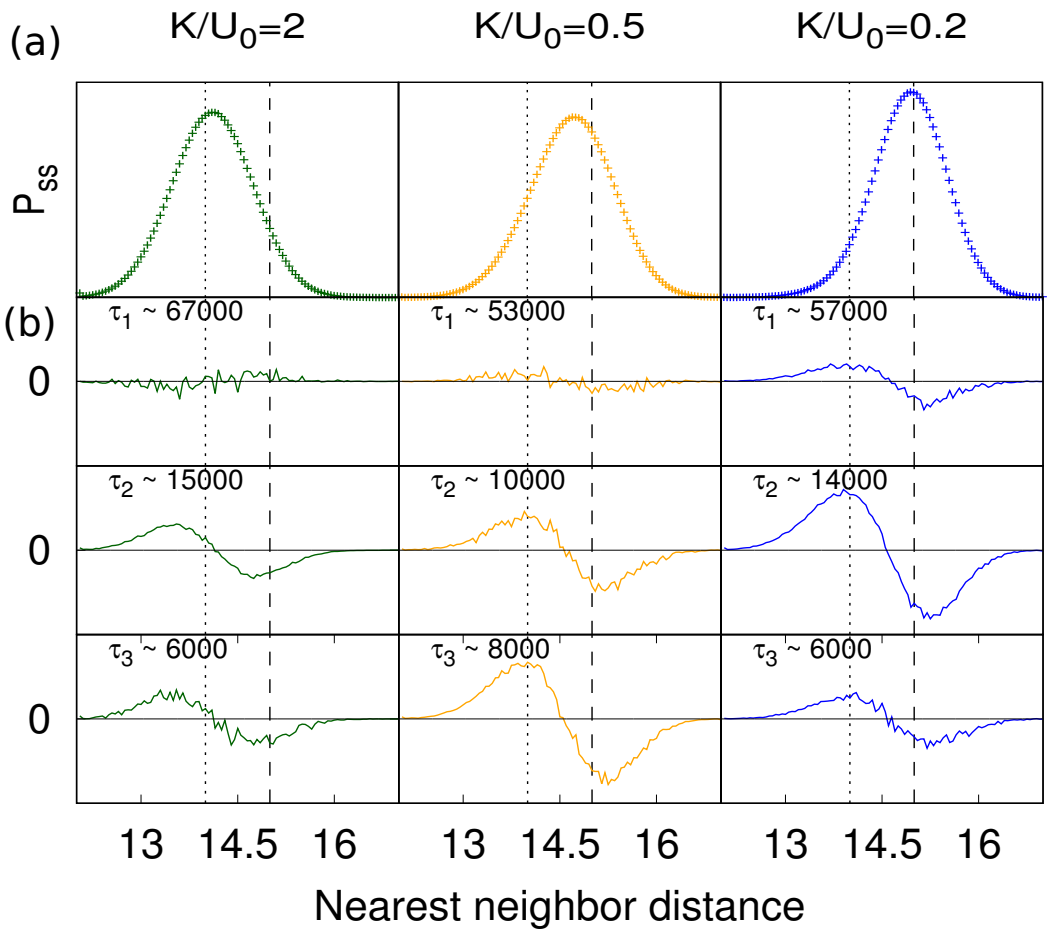


Figure 3.15: Two-dimensional incommensurate FK model. (a) Steady state probability distribution of the nearest-neighbor distances for the three regimes. Vertical dotted lines represent the rest interparticle ("harmonic") distance, while the dashed ones represent the substrate lattice spacing. (b) The perturbations $g_i$ (see Equation 3.3) estimated for the first three excited states. The observable $O$ in Equation 3.3 is here the nearest-neighbor distance. To compute $P(O|\alpha)$, 100 intervals have been chosen.

### Harmonic energy

We now consider the distribution of the total harmonic energy of the island:

$$\frac{K}{2}\langle \sum_{\langle i,j\rangle \in NN} \left(\mathbf{r}_i{}^t - \mathbf{r}_j{}^t\right)^2 \rangle \ . \tag{3.7}$$

Figure 3.16(a) shows the steady-state distributions, clearly highlighting the richer information encoded by this observable. In the stiff $K/U_0 = 2$ case, the distribution of this observable shows a single peak, while in the softer cases, it acquires a more complex structure, related to the presence of a different number of solitons in the system. The corrections in Figure 3.16(b) highlight how the different modes (besides the first one, as previously noted) are related to different relative weights in these soliton distributions, representative of the different dynamics of each regime: while in the stiff case, the few defects merely slide through the island during the motion, leaving their population unchanged; for the softer islands, the stick-slip motion is achieved through the creation of new solitons at the edges and their relatively fast propagation, leading to a complex time dependence of their population.

### Single particle positions

To gain additional insight in the nature of the slow dynamical modes we now consider the probability distribution of the position of a single particle (not on the border) as a function of its position $x$ and $y$. The periodic boundary conditions have been chosen as two lattice spacings of the 2D potential, both in $x$ and $y$. The steady state positional distribution of Figure 3.17(a) again shows how the increase of $U_0$ leads from a smooth distribution over the continuous transition path from a minimum to the next, to an increasingly peaked distribution in the potential minima. Therefore if for $K/U_0 = 2$ the particle performs a rather smooth zig-zag path between successive potential minima, in the intermediate case ($K/U_0 = 0.5$), these positions are much more probable, eventually becoming dominant for $K/U_0 = 0.2$ where the distribution reduces essentially to sharp peaks. The excited state effect on the particle position distribution is shown in Figure 3.17(b). While the first excitation is clearly related to the single period shift, as mentioned earlier, the second excited state shows that the particle jumps among successive minima in the zig-zag path. This shorter periodicity was not visible in the previous observables as it is not shared by all particles. The third excited state, finally, reflects the particle position probability perturbation caused by the "slip" events, which are characteristic and strong for the softer island, as in the previous analysis.

### Work distribution

As a final observable, relevant to the description of a frictional model, we consider the instantaneous work done on the system by the external force in a single time step $\tau$:

$$W_t = \kappa \sum_l \left(v_{ext}t - x_l{}^t\right)\left(x_l{}^{t+\tau} - x_l{}^t\right) \ , \tag{3.8}$$

shown in Figure 3.18(a). Notice that this quantity depends on the successive position at time steps $t$ and $t+\tau$. The steady-state work distribution $P_{SS}(W)$ is centered on $\langle W\rangle$, a value evolving from near zero to larger values as one goes from $K/U_0 = 2$ to $K/U_0 = 0.2$. At the same time, $P_{SS}(W)$ develops an increasing asymmetry with a broader and broader tail around positive values of work. Both features are related to the increase of dissipation as the substrate corrugation increases. As seen in Figure 3.18(b) for $K/U_0 = 2$, the excitations show just noise, which tells us that the slider moves as a whole, as the characteristic of the superlubric sliding in this regime. The notable

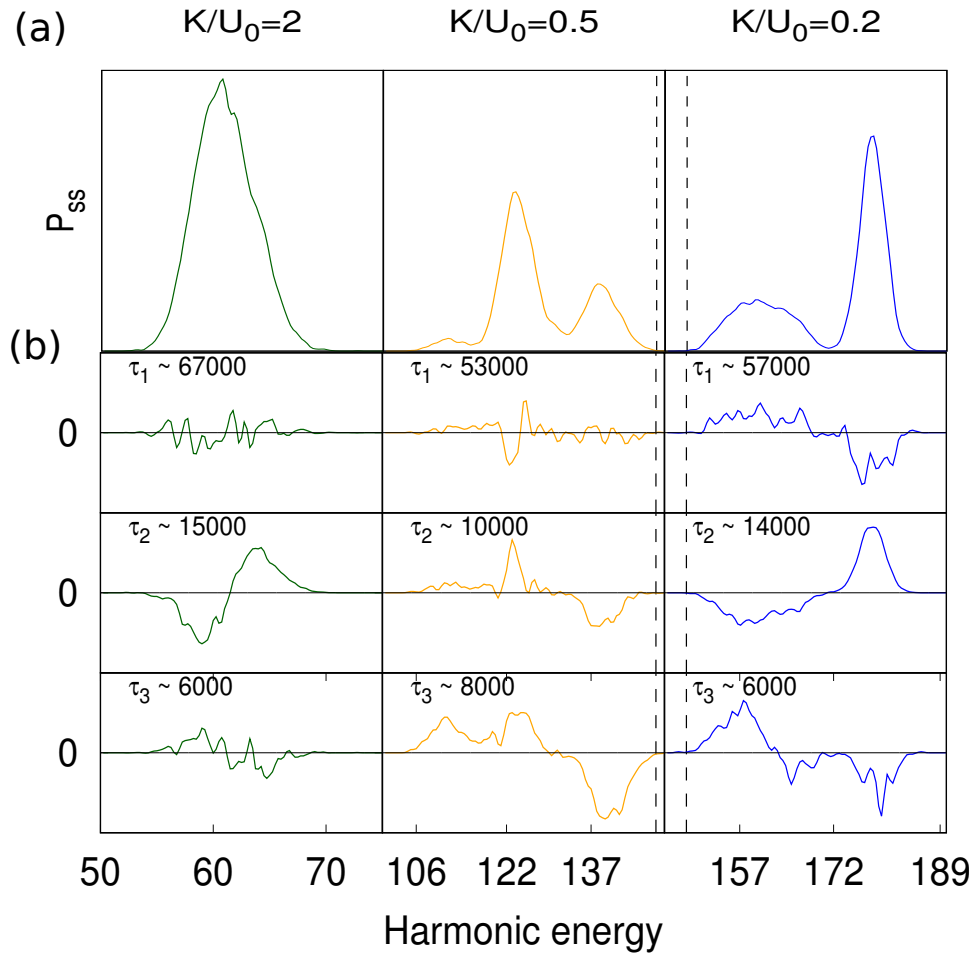


Figure 3.16: Two-dimensional incommensurate FK model. (a) Steady state probability distribution of the harmonic energy for the three regimes. The vertical dashed lines represent the harmonic energy for an island completely relaxed to the substrate lattice spacing. In this case, we applied a running average to the data, both for the steady-state distribution and the corrections. The switch from a single peak of the hard island to a multiplicity of peaks for the medium to soft island is the direct evidence of the more elaborate sliding dynamics of the latter. (b) The perturbations $g_i$ (see Equation 3.3) estimated for the first three excited states. The observable $O$ in Equation 3.3 is here the harmonic energy. To compute $P(O|\alpha)$, the abscissa axis has been divided into 100 equal intervals.

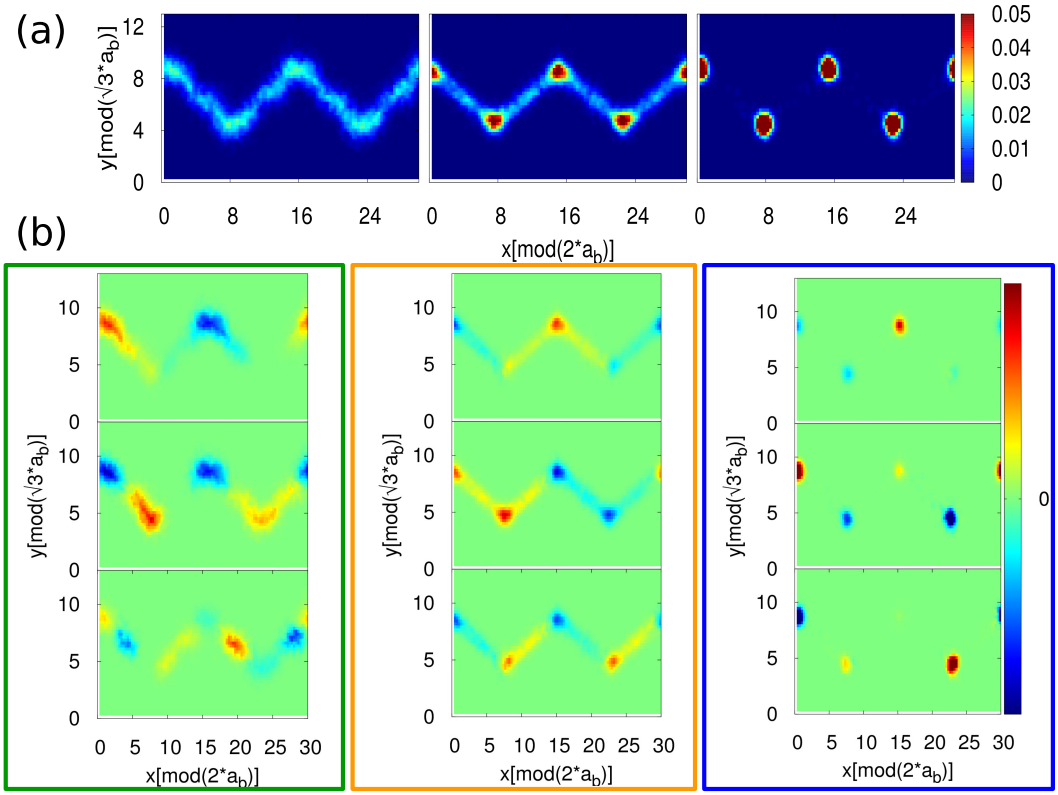


Figure 3.17: Two-dimensional incommensurate FK model. (a) Steady state 2D probability distribution of all single particle positions (excluding edges) for the three regimes. Position along $x$ and $y$ is taken modulus 1 and 2 lattice spacings, respectively. The zig-zag pattern reflects the motion of the whole which, while pulled along $X$, moves between neighboring potential minima that are 60°off. (b) The perturbations $g_i$ (see Equation 3.3) estimated for the first three excited states. The observable $O$ in Equation 3.3 is here the the single particle positions. Note the evolution for decreasing $K/U_0$, from smooth flow to sharp hopping between minima. To compute $P(O|\alpha)$, the binning on the axes has been chosen in this way: 100 intervals for $x$, and 50 for $y$.

exception is however the second excitation, showing a forward jump. As we move towards smaller and smaller $K/U_0$ and the island softens, all excitations gradually come into play. In the stick-slip regime for $K/U_0 = 0.2$, modifications in the soliton structure are strongly related to an increase in the positive tail of the work distribution, highlighting the mechanism behind the increased friction coefficient.

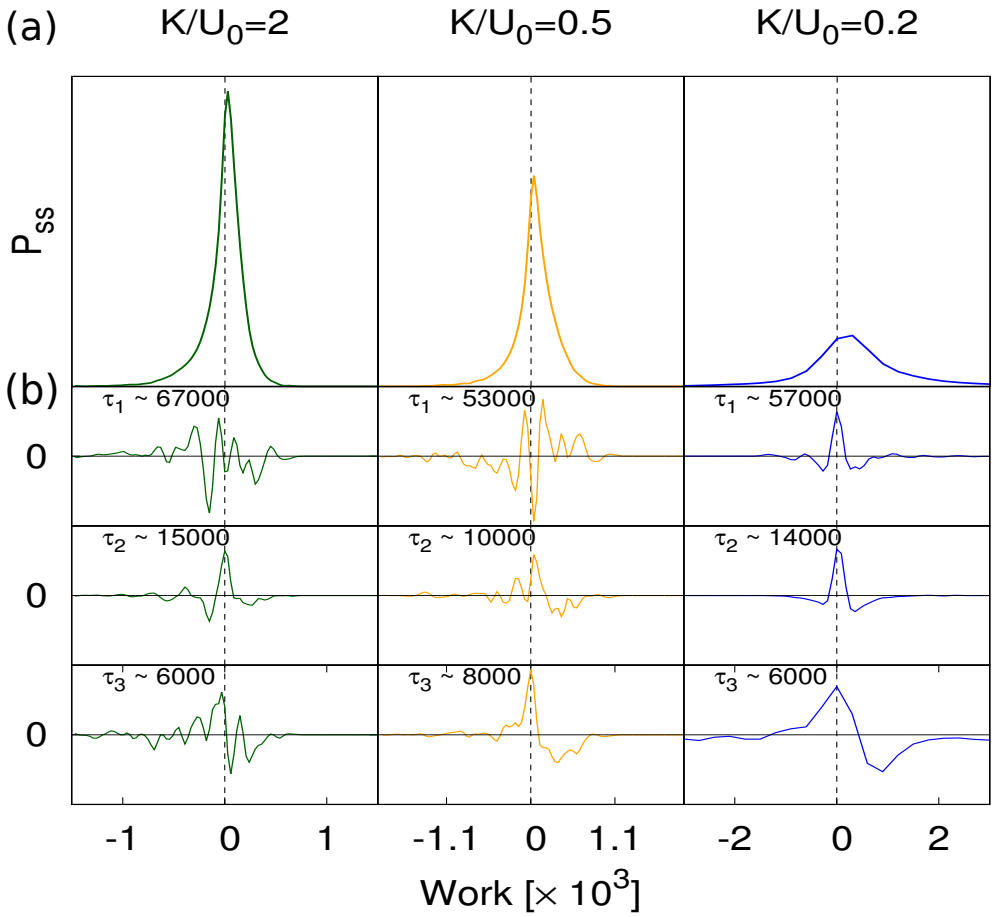


Figure 3.18: Two-dimensional incommensurate FK model. (a) Steady state probability distribution of work for the three regimes. In this case, we applied a running average to the data, both for the steady-state distribution and the corrections. (b) The perturbations $g_i$ (see Equation 3.3) estimated for the first three excited states. The observable $O$ in Equation 3.3 is here the work. To compute $P(O|\alpha)$, the abscissa axis has been divided into 100 equal intervals.

### 3.3.5 Conclusions and comments

In this section we have presented the MSM study for a 2D Frenkel-Kontorova hexagonal island. We had already studied FK model in one dimension, but fulfilling the goal of the application of our method to a 2D system has been crucial to understand how to analyze a real system. In fact, even though still a model, the system analyzed here presents already a triangular symmetry typical of materials like graphene that have been widely studied in experiments; moreover, the slider

already possesses a number of particles similar to the ones of the sliders used in realistic frictional simulations. Despite many thousands of atomistic degrees of freedom, the procedure developed allows the selection of just very few slow variables, automatically eliminating all other fast irrelevant variables. Those slow variables, once examined at the end, are found to be appropriate for describing the actual frictional physics of the system, be it superlubric or stick–slip.

# Chapter 4

# Sliding of a graphene island on a non-periodic substrate

In this chapter we analyze a much more realistic system, with respect to the periodic ones studied in the previous chapter. It consists of a circular island of graphene (inscribed in an original hexagonal flake), saturated by hydrogens at the borders, and sliding on a substrate realized starting from an FCC crystal of gold, whose surface has been shaped rough. The system is shown in Figure 4.1. The substrate surface has been shaped rough as a lot of surfaces of interest in friction, and also a lot of natural surfaces (like the ones described in Section 1.2.6) present a self-similar profile. Moreover, we have chosen graphene as a slider as it is very stiff and strong, and very lubric, while experiencing no wear. When pulled by a spring (which in our case is a spring coupled to the center of mass of the flake) mimicking an AFM tip, the graphene island will get stuck here and there on the rough substrate. Strong elasticity of graphene gives rise to stick-slip events, including as we will see realistic translations and rotations.
This simulated system will be useful in several ways. First, it will provide a comparison with the MSM study of the sliding over a periodic substrate presented in the previous chapters. Since the system is modeled by atomistic description, the analysis will also permit the extraction of realistic mesoscopic variables relevant to friction, and of their fluctuations. For example, the waiting times between two successive slip events, or the dissipation energies. Finally, we manage to test our method in real conditions, like the absence of any reference periodicity in the substrate, making the identification of the microstates an extremely challenging task.
We would like to highlight the fact that the method has not changed throughout the study of the different systems, even if the arrangements differed a lot in number of particles, kind of substrate, even dimensionality. MSM of sliding friction always starts with a long MD simulation (or, equivalently, many small MD simulations); a clustering algorithm (DP clustering or DPA) is used to find a small discrete number of microstates, and finally a normalized transition matrix is calculated, measuring the probability of jumping between pairs of clusters. The transition matrix, in turn, describes the coarse grained frictional kinetics.

## 4.1 The system in details

The graphene slider is a circular sheet of graphene consisting of 1440 carbon atoms. The circular shape has been obtained inscribing the circle in an hexagonal graphene flake; the resulting sheet has been subsequently saturated by 96 hydrogens at the borders, in order not to leave unsatu-

rated bonds for the carbon atoms. The carbon-carbon distance has been set to 1.4224 Å, while the carbon-hydrogen distance is 1.0904 Å(see Figure 4.1). For both carbon-carbon and carbon-hydrogen interactions AIREBO potential [49] has been used, with a cutoff of 20 Å(see Section **??** for further details).
The flake is pulled by a spring coupled to a dummy "atom" (the tip) of weight 1000 amu, which does not interact with gold atoms and moves linearly, in time and direction, at a constant speed $v_{ext}$. The velocity of this "tip" is oriented by an angle of 47 °relative to the gold (110) surface direction, so as not to be aligned with any of the substrate high-symmetry directions.
The substrate has been obtained from an FCC gold bulk, "cutting" a self-similar random surface, adapting to our study the self-similar crystal $512 \times 512$ surface profile by Müser *et al.* [36] (see also Section 2.1.3). The Z profile (top), together with a zoom on the atomic configuration (bottom) are shown in Figure 4.1. The interaction of gold with carbon is a Shifted-Force Lennard-Jones [51], with parameters: $\varepsilon = 0.025$ eV, $\sigma = 2.74$ Å, while that with hydrogens is the same but with $\varepsilon = 0.01$. The gold substrate is assumed, for simplicity, to be rigid: all dissipation being embodied in the flake itself, employing a large value of $\gamma$ in the Langevin dynamics. We have adopted a rigid substrate since we wanted to compare the results obtained for the graphene flake to the ones obtained in the previous chapter for infinite periodic rigid substrates.
The pulling velocity has been set to $v_{ext} = 0.01$ Å/ps; the island slides with a stick-slip dynamics, alternating periods of accumulation of elastic energy and subsequent sudden releases upon advancement. The dynamics is an overdamped Langevin one with temperature $T = 200$ K and damping $\gamma^{-1} = 1$ ps. The dynamics was carried out using LAMMPS [43].

We have performed 350 independent simulations, each one 6 ns long. The time step chosen is $dt = 0.001$ ps. We decided to carry out independent runs, providing in such way a good statistics, as we wanted to study the distributions of both the dissipated energy and the waiting time between successive slips, starting from several different independent initial conditions.
From visual inspection of our simulations, it is clear that the dynamics of the slider shows a behavior really similar to that of seismic events. The accumulation of tension due to the corrugation of the graphene island, together with the sudden release in its rotation and successive translation made us speculate about the possibility that quantities like the waiting time between slips and the dissipation energy should satisfy the Gutenberg-Richter type power law [19, 20, 41]. This law relates the magnitude of an earthquake to the fraction of the total number of earthquakes in any given region and time period of at least that magnitude. The relation is the following:

$$\left(\frac{N}{N_{total}}\right) = 10^{\alpha - \beta M} , \tag{4.1}$$

where $N$ is the number of events having a magnitude larger or equal to $M$, $N_{total}$ the total number of events, while $\alpha$ and $\beta$ are constants. $\alpha$ and $\beta$ are constants, and the magnitude $M$ is computed as the logarithm of the the total energy released in an earthquake. Quantities like the waiting time between successive slips and the energy dissipated in a slip event are also expected to show a power law similar to the one in Equation 4.1. The magnitude $M$ in the equation is going to be substituted by these quantities. The results of this analysis are presented in the following section.
The idea of comparing the dynamics of our system with the one of seismic events has started from a visual inspection of MD trajectories. We have noticed that the island movements were formed by quite long slip periods, followed by abrupt changes characterized by a large dissipation in energy (namely, the slips). Moreover, the Gutenberg-Richter law has been empirically justified using the Burridge-Knopoff frictional model, consisting in a chain of blocks coupled by springs [9, 41].
In each of the simulations we have observed on average $\sim 20$ slip events; the center of mass moves of around 70 Å in the drag direction, while the shift in the direction perpendicular to the motion

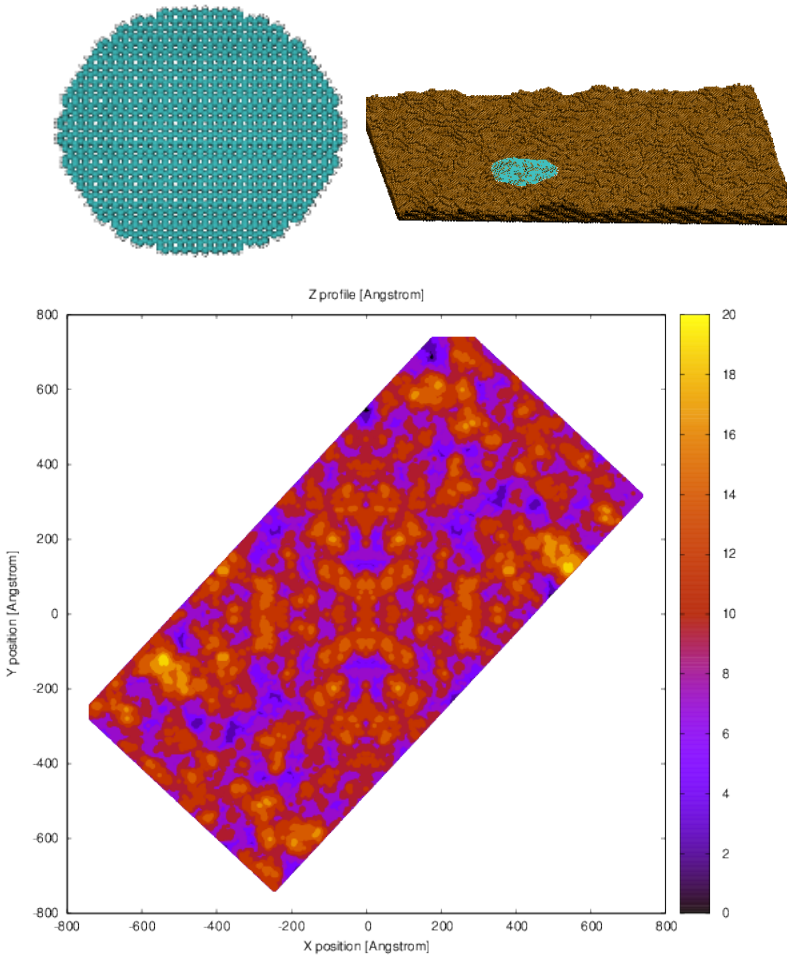


Figure 4.1: Top left: graphene slider, circular island. Carbon atoms are shown in light blue, while the hydrogens at the borders in white. Top right: focus on both the island and the substrate, with atomistic detail. Bottom: the Z profile (the color scale is in Angstrom) of the gold substrate.

is negligible. The initial configurations for every run have been created in order to maximize the sampled substrate surface. Knowing the average length and width of the path covered by the slider center of mass during one simulation, we divided the substrate surface in almost equal subsections, in order to make the smallest overlap between different trajectories. Once the single subsection has been identified, we restarted by the slider, for each new run, at the basis of each area with a procedure of minimization of the total energy implemented in LAMMPS (further details about the procedure can be found in [48]). In this way, the planar slider adapts to the surface of gold before the beginning of the simulation.

### 4.1.1 Analysis of some steady-state friction-related quantities

We first studied the behavior of some mesoscopic quantities that are going to give us a useful interpretation of the dynamics.
The first quantity is the Center of Mass (CM) trajectory: this quantity gives us an insight on the mesoscopic dynamics of the system. Figure 4.2 shows a stick-skip behavior with relatively long sticking periods. During the sticking, the motion in the XY plane is somehow viscous. No stick-slip regularity is present, reflecting the substrate roughness. In Figure 4.2 the projection of the CM path on the XY plane is shown, together with a straight line representing the path the island would have followed in a perfect lubric regime. We notice just occasional deviations in angle with respect to the tip direction of motion, which probably reflect the necessity of a small rotation when the island meets a standing block. One possibility is that the deviations in angle with respect to the tip direction of motion might be due to moiré patterns (see Section 3.3 for further details) that create in the whole island or in parts of it due to its interaction with the substrate, in a similar way to the analysis of the 2D Frenkel-Kontorova model. The most plausible possibility is that the island "stumbles" on an asperity, and rotations help to override it.
Figure 4.3 shows the velocity of the center of mass. This is another key quantity in the study of friction. In fact, the stick-slip behavior, together with the duration of sticking times, can be immediately identified from this observable. Figure 4.3 clearly shows the main peaks corresponding to slip events: the $X$ coordinate of the center of mass has been superimposed to the velocity (the offset of the CM position is arbitrary) in order to show the correspondence between the main peaks and the slip events. In our analysis we identify slip events from the peaks of $v_{CM}$: we assume an event has occurred whenever $v_{CM} \geq 0.07$ Å/ps. The black arrows indicate the events that have been taken into account in the analysis, while the red ones indicate the slip events that occurred but were not detected. The first peak of $v_{CM}$ around $\sim 420$ ps has not been detected correctly, even if above the threshold, as we have neglected an initial time of 500 ps to avoid the first stick which is longer than the subsequent ones, due to the initial transient of time needed to overcome static friction, and to the initial elongation of the driving spring. Moreover, in order not to count multiple close slips that belong to a single slip event as separated, we distinguished slip events delayed at least 150 ps. For example, around 6000 ps in Figure 4.3, we detect one slip event out of two peaks. Few other slip events have not been detected along the dynamics, but we can conclude that the failed detections are far less than the one correctly identified.

In Figure 4.4 the spring drag force in the XY plane, computed as $\vec{F} = K\vec{r}$ in the direction of drag (where $\vec{r}$ is the vector distance between the tip coordinate and the island center of mass), is shown, together with $\theta$, the orientation angle of the island (computed as the angle between a chosen diameter of the island and the X axis). The spring force is a key quantity in nanotribology, revealing the fundamental frictional response, as it represents the direct connection between the driving and the system. The force is negative in certain periods of time, which means that there are some overshoots that occasionally launch the island slide further than the tip, as suggested by

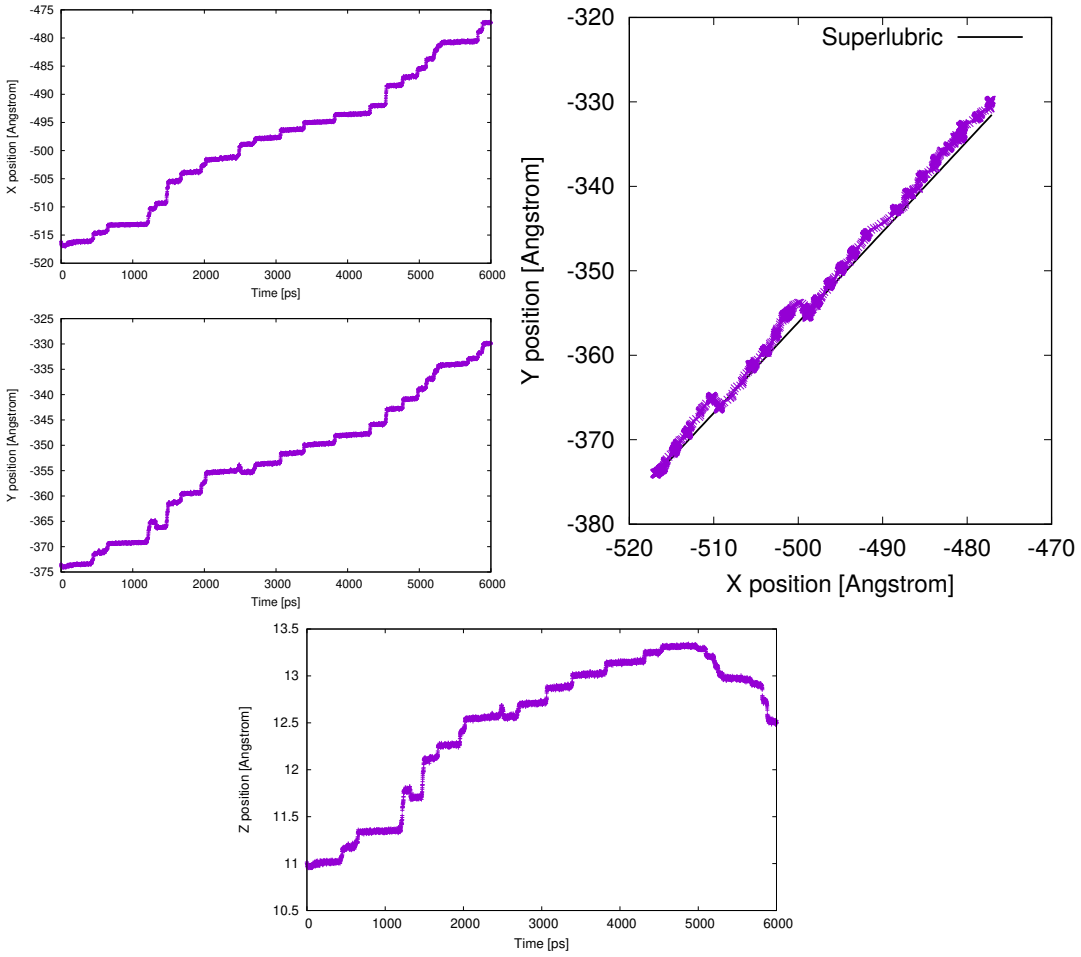


Figure 4.2: Representative results for a stick-slip run. Left: center of mass trajectory as a function of time, for the x and y. Steps indicating stick-slip dynamics can be identified. Right: center of mass trajectory projection in the XY plane, compared with tip position, or with superlubric sliding. Bottom: center of mass trajectory a a function of time, in the off-surface z direction.

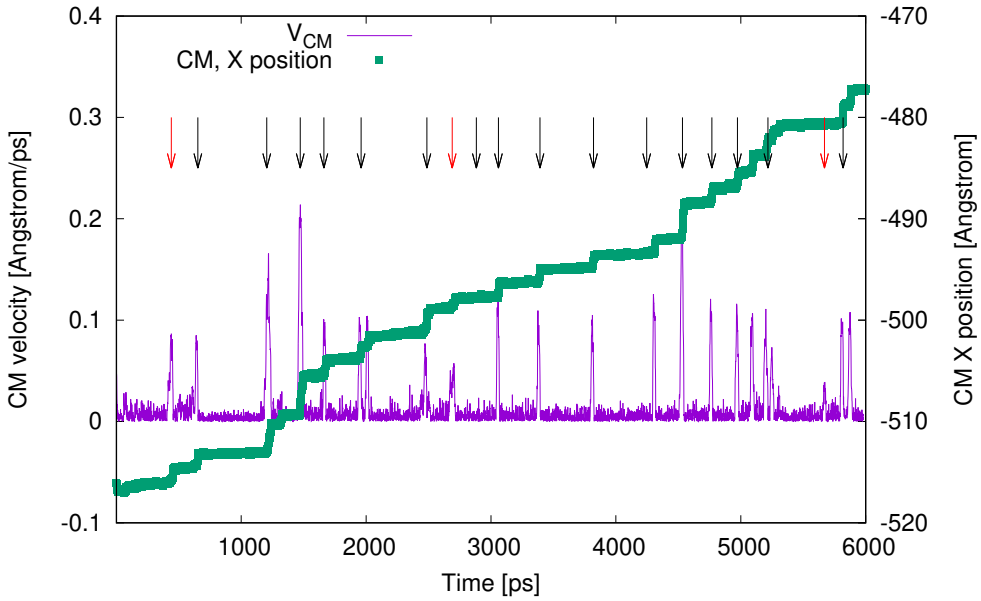


Figure 4.3: Center of mass velocity, together with the $X$ coordinate of the center of mass trajectory (the offset of the CM position is arbitrary, taken from the same simulation concerning the velocity profile). A slip has been chosen as an event with $v_{CM} \geq 0.07$ Å/ps. The black arrows indicate the events that have been taken into account in the analysis, while the red ones indicate the slip events that occurred but were not detected. Note that in this plot the velocity is always positive, because we have performed a running average on 10 ps. The instantaneous velocity assume positive and negative values, instead.

the visual inspection of some of the trajectories. Moreover, slip events are often anticipated by rotations of the island, responsible for unlocking the graphene from the gold substrate, as illustrated by the almost perfect correlation is present between the changes in the island orientation and the slip events in Figure 4.4.

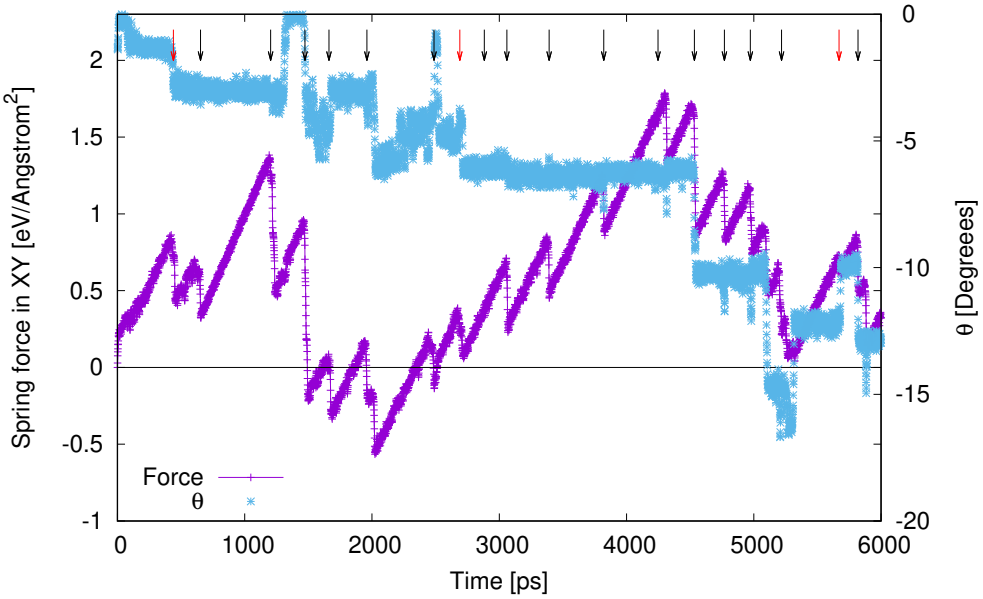


Figure 4.4: Spring force between the tip and the center of mass of the island, together with the angle orientation $\theta$ of the island ($\theta$ has been computed as the angle between a generic chosen diameter of the island and the $X$ axis). An almost perfect correlation is present between the changes in the island orientation and the slip events. This corroborates our hypothesis that rotations open the way to slip events. The black arrows indicate the events that have been taken into account in the analysis, while the red ones indicate the slip events that occurred but were not detected.

We then analyzed the behavior, over time, of the spring harmonic energy, the internal carbon-carbon energy of the flake and the interaction energy between flake and the substrate; in Figure 4.5 we show their deviation with respect to the average value. Slip events correlate with main changes in energy. Moreover, the variation in elastic energy is balanced to the one in interaction energy.

The last two quantities that we are going to introduce are different from the ones we have analyzed before: the slip dissipation energy and the waiting time between slip events are studied as distributions. From visual inspection of the simulations, we noticed that the dynamics of the graphene slider is similar to a seismic event, with accumulation of potential energy and subsequent sudden releases. Because of this, we guessed that the probability distributions of some quantities like the waiting time between slips or the dissipated energy might follow the Gutenberg-Richter law, as in Equation 4.1. The role of the magnitude $M$ in the equation is going to be assumed by the waiting time or the dissipated energies, fitting each time the constants $\alpha$ and $\beta$. Figure 4.6 shows the fraction of the number of occurrences against the waiting time $t_w$ between slips, in log-log scale. We find constants $\alpha_{t_w} = 0$ and $\beta_{t_w} \sim 0.0029$ ps$^{-1}$.

In a way similar to the case of waiting times, we find a similar behavior also for the distribution

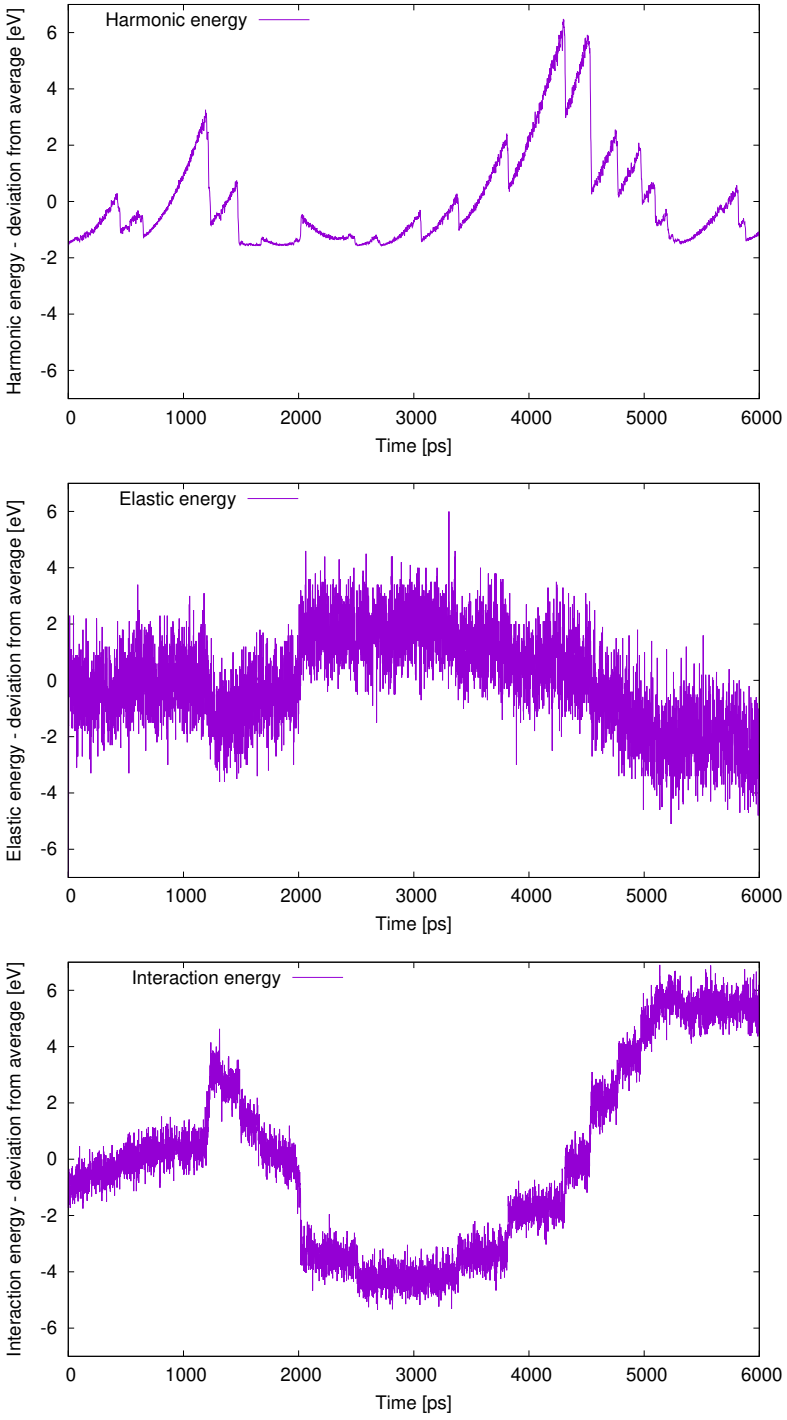


Figure 4.5: Potential energies (deviation from average). From top to bottom: pulling spring energy, internal elastic energy of the flake, interaction energy between the flake and the substrate. We remind to the reader that the main contribution to the energy is given by the elastic energy of the graphene flake, with average $\sim 11140$ eV, followed by the interaction energy between the flake and the gold substrate, with average $\sim 110$ eV, and the harmonic energy with average 5 eV.

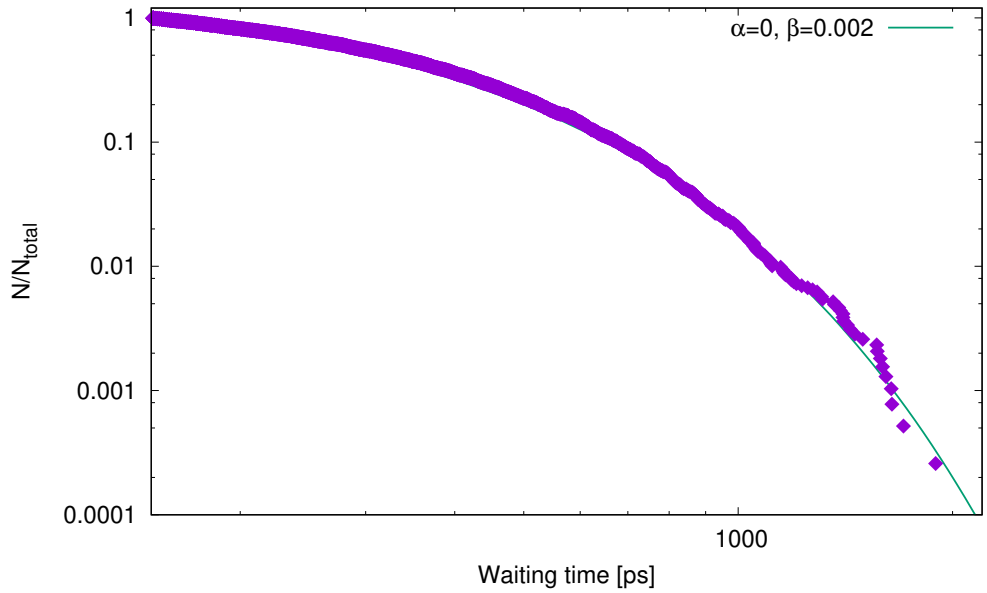


Figure 4.6: Fraction of number of occurrences vs. waiting time between slips, log-log scale. For the waiting time we have found constants $\alpha_{t_w} = 0$ and $\beta_{t_w} \sim 0.002$ ps$^{-1}$ (see Equation 4.1 for details).

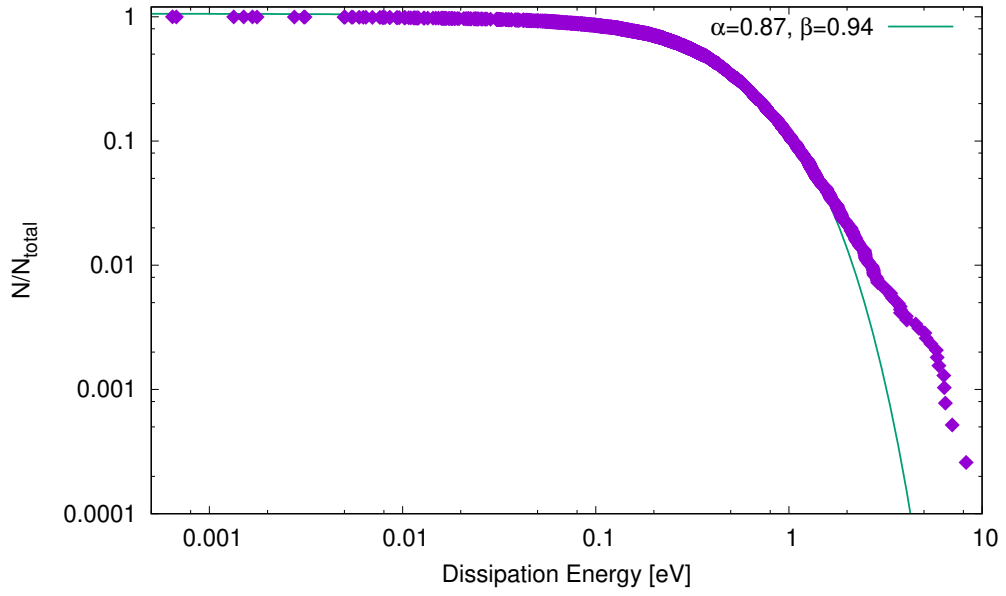


Figure 4.7: Fraction of number of occurrences vs. dissipation energy, log-log scale. For the dissipation energy $E_{diss}$ we have found constants $\alpha_{E_{diss}} \sim 0.87$ and $\beta_{E_{diss}} \sim 0.94$ eV$^{-1}$ (see Equation 4.1 for details). The points have been fit with Gutenberg-Richter law in the range from 0 to 8 eV.

of the dissipated energy (computed as the product $F \cdot v_{CM}$), see Figure 4.7, in log-log scale. We obtain constants $\alpha_{E_{diss}} \sim 0.87$ and $\beta_{E_{diss}} \sim 0.94$ eV$^{-1}$. For the dissipation energies, the points have been fit with Gutenberg-Richter law in Equation 4.1 in the range from 0 to 8 eV.

## 4.2 Markov State Modeling

So far we analyzed the steady-state sliding of the graphene island. We are now going to present the MSM analysis, to learn about the study of the dynamics. The system described in this section is more realistic than the FK model, with a dynamics characterized by abrupt slips in a way that reminds much more of seismic behaviors than of the sliding of two perfect lattices. Moreover, the rough nature of the substrate pushes the application of the MSM procedure defined so far to its limits, in terms of the definition of the metric, of the decimation of the initial dataset for the clustering analysis, and of the interpretation of the results.

### 4.2.1 Choice of phase space metric

The 350 simulations of length 6 ns each produce the positions of all the atoms at each time step. In the previous chapter, we have chosen the metric in the most unprejudiced and blind possible manner. The particle positions have been sufficient to describe both the 1D and the 2D periodic Frenkel-Kontorova model, but a similar choice for the system we are describing now is unfeasible. In fact, due to the rough nature of the gold substrate, this time we are not allowed to adopt a metric in which we take advantage of the substrate periodicities. The areas of the substrate sampled by the flake are never identical to each other, and no geometrical references can be found to identify a unit cell that repeats over the surface, on which the configurations can be mapped back.
Because of this issue, the quantities we have chosen are not absolute, but internal of the flake: the first one is devoted to the description of the slider deformation in the out-of-plane direction, while the second has a close connection with the interaction between the carbon and the gold atoms. From each of the MD configurations, we have computed for each carbon atom $l$ of the slider two microscopic quantities: the strain ${S_l}^t = {z_l}^t - \langle Z \rangle_l$, defined as the deformation with respect to the average $\langle Z \rangle_l$ of the Z coordinate (labeling the out-of-plane direction), for all the configurations sampled in all the simulations, and the distance from the carbon atom to the closest gold atom of the substrate, namely ${\delta_l}^t = \min_{j \in Au} |{\mathbf{r}_{lj}}^t|$, with $\mathbf{r}_{lj}$ the vector distance between the two atoms.
However, defining the strain and the C-Au distance on an atomistic scale would have created a metric with $\sim$ 3000 degrees of freedom, far too many. For this reason, the metric has been defined on a two-dimensional mesh of 44 points with triangular symmetry, shown in Figure 4.8, on the right. The mesh of points is defined coherently with the direction of drag: the red arrow in Figure 4.8 (right) shows the drag direction on the mesh. In order to superimpose the mesh to the configuration given by the positions of the carbon atoms of the flake in the correct way, we have first aligned the centers of mass of both the flake and the mesh. Subsequently, the configuration and the mesh are rotated in such a way that the drag directions coincide. In this way, we have been able to find, for each of the points $p$ of the mesh, the atoms $l$ in their proximity. For each point $p$ of the mesh, we compute a gaussian average, weighted with the distance from the point $p$ to the position of the carbon atom $l$. For an observable $O$:

$$\bar{O}_p = \frac{\sum_l \mathcal{N}(\mathbf{x}_l, \mathbf{x}_p, \sigma) O_l}{\sum_l \mathcal{N}(\mathbf{x}_l, \mathbf{x}_p, \sigma)} , \tag{4.2}$$

where $O_l$ the value of a generic quantity of the metric for the atom carbon $l$, and the gaussian weight is the following:

$$\mathcal{N}(\mathbf{x}_l, \mathbf{x}_p, \sigma) = \frac{1}{\sqrt{2\pi\sigma^2}} \exp\left[\frac{-(\mathbf{x}_l - \mathbf{x}_p)^2}{2\sigma^2}\right] . \tag{4.3}$$

The distance $\mathbf{x}_l - \mathbf{x}_p$ is computed in-plane (not for the Z coordinate), while $\sigma$ is set at the distance between two nearest-neighbor points of the mesh.

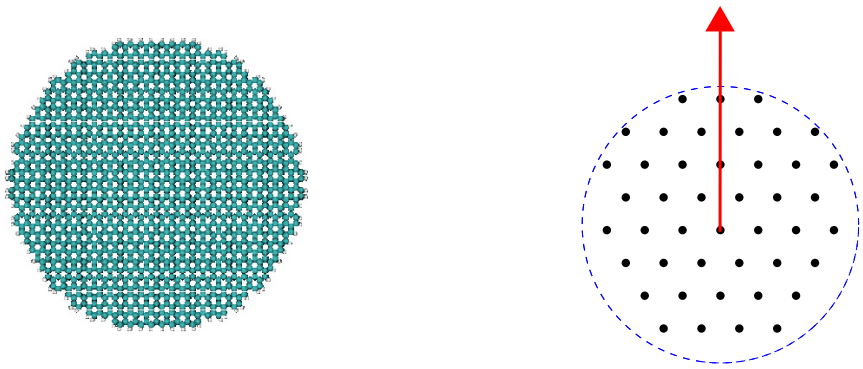

Figure 4.8: On the left, the graphene flake used as a slider. On the right, the mesh of 44 points with triangular symmetry that has been used to create a coarse-grained metric. Considering a point of the mesh, for each carbon atom in its neighborhood we have exploited a gaussian average of the value of every quantity constituting the metric. The Gaussians are centered in the different points of the mesh and have a value of $\sigma$ equal to the distance between two points of the mesh.

Once the gaussian averages for each of the points of the metric have been computed, the distance between two configurations $s$ and $t$ has the following form:

$$d_{st} = \left[\sum_{p=1}^{44} \left(\bar{S}_p^s - \bar{S}_p^t\right)\right]^2 + \left[\sum_{p=1}^{44} \left(\bar{\delta}_p^s - \bar{\delta}_p^t\right)\right]^2 , \tag{4.4}$$

where $\bar{S}_p$ and $\bar{\delta}_p$ are the gaussian averages of the out-of-plane strain and the carbon-gold distance, as defined in Equation 4.2, one value for each of the 44 points of the mesh.
In conclusion, this first coarse-graining has allowed us to pass from $\sim 3000$ degrees of freedom for each configuration, to a much more manageable metric, defined by the 44 values of the strain in Z direction, together with the 44 values of the distance from the closest gold atom, one for each point of the mesh.

### 4.2.2 Clustering analysis

As previously stated, we analyzed 350 independent simulations of 6 ns each, $dt = 0.001$ ps. We used just a subset of the whole data set in order to find the phase space clusters. In fact, in order for PAk algorithm to work, the quantities analyzed have to be uncorrelated. If they are too correlated, such as when the clusters are formed between configurations close in time, the algorithm is affected by large systematic errors. For this reason, decimation has been a key issue in our analysis, and in the end we have kept one configuration out every 400 ns. Such a dramatic decimation, healthy as it is, required a huge statistics, and many different simulations. The data

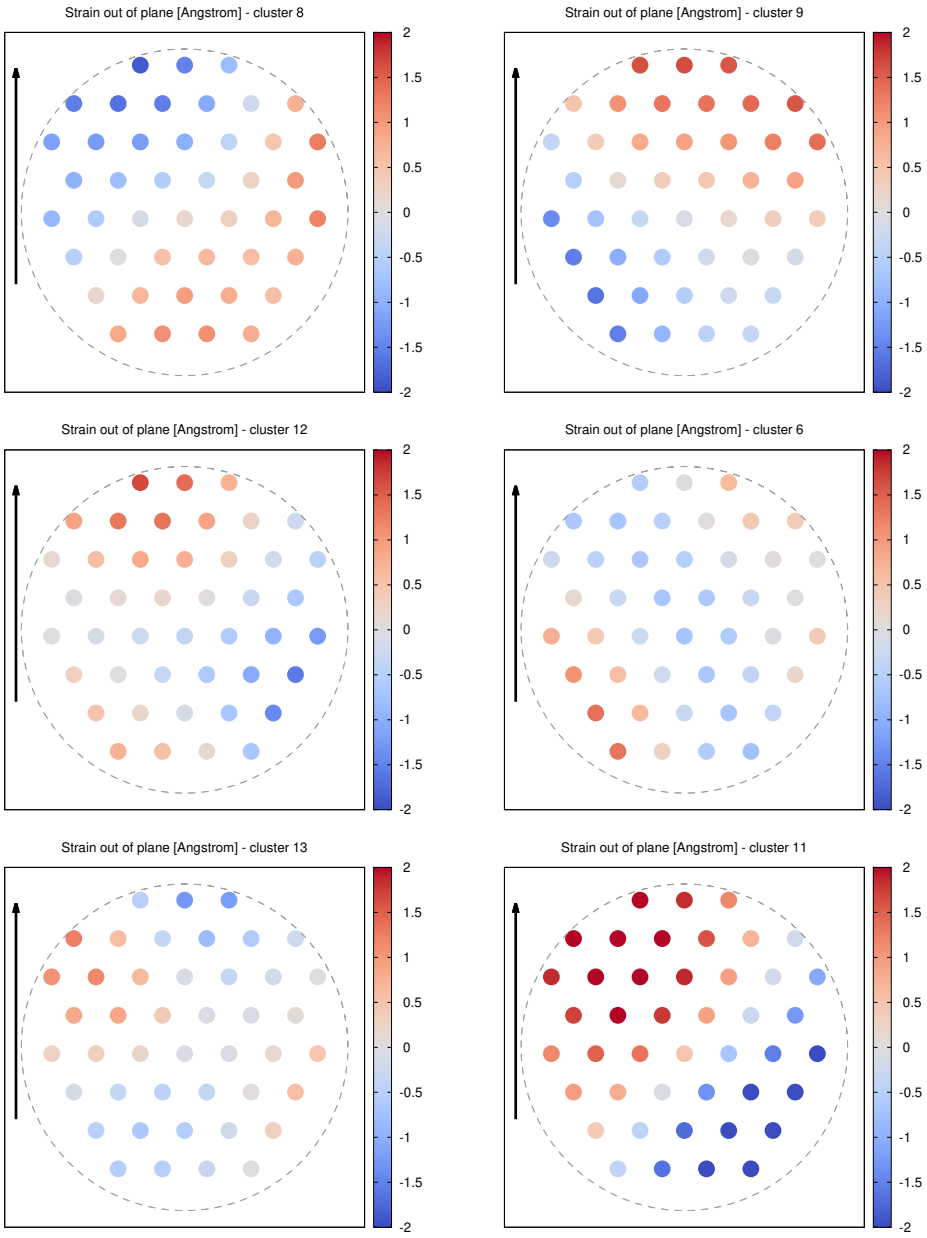


Figure 4.9: Profile of the out-of-plane strain, for the centers of the most populated clusters. The arrow pointing up is indicating the drag direction of the tip. The strain in the Z direction identifies macroscopic movements of the graphene island.

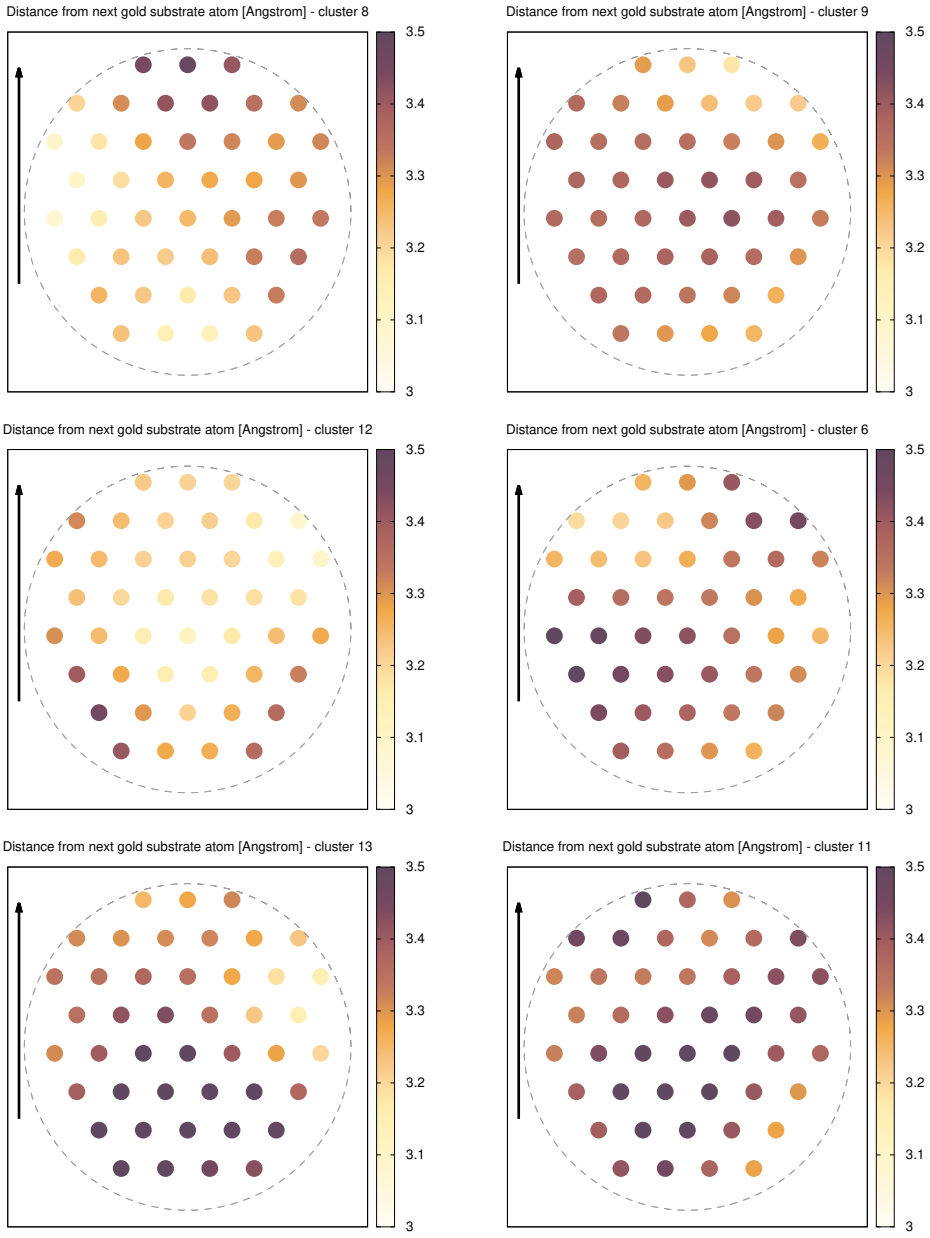


Figure 4.10: Profile of the distance from nearest gold atom, for the centers of the most populated clusters. The arrow pointing up is indicating the drag direction of the tip. With respect to the out-of-plain strain profile in Figure 4.9, this quantity displays patterns with variations on a more local scale on the mesh.

points that have not been used for the definition of the clusters due to the decimation have been reassigned to the closest cluster, using the metric defined above.
For the clustering analysis we have employed the DPA (see Section 2.2.4) clustering algorithm for the identification of the microstates. Thanks to the ability of PAk to recognize the minima of the free energy, we have obtained $\sim 10$ clusters.
We describe the states identified by the clustering algorithm. Figure 4.9 shows the profile of the out-of-plane strain for the centers of the most populated clusters. It is important to notice that all these states show macroscopic patterns of corrugation over the 44 points of the mesh. This means that the microstates identified by the method are not related to movements concentrated on a small number of atoms (if that would be the case, every point of the mesh would assume a completely different value for the quantity studied), but to global changes in the island corrugation. These corrugations, exhibiting a bimodal front-back or left-right dynamics, as well as more complicated patterns on the mesh, reflect the main symmetries of the graphene flake. The other quantity included in the mesh is the distance from the nearest gold atom. Figure 4.10 shows its value on the 44 points of the mesh, for the centers of the most populated clusters. These profiles show more local variations on the mesh with respect to the corrugation profiles in Figure 4.9. However, from a visual inspection of the MD trajectories, one can see that the slip events are frequently correlated with the depinning of some of the borders part of the island, preceding the subsequent slipping of the graphene island. We conclude that the distance from nearest gold atom reflects this phenomena, leading the way to the sliding. The value of the parameter $\sigma$ in the Lennard-Jones interaction for the C-Au and H-Au interaction has been set to 2.74 Å. However, this figure shows values always larger than $\sigma$, because the gold surface is rough with a non-flat profile in the $z$ direction. This means that the real contact between the graphene flake and the substrate takes places in small areas of the slider, while the rest of the island is suspended. This is the reason why the average value of the distance from the nearest gold atom for each point of the mesh is always larger than $\sigma$.

### 4.2.3 Transition Matrix evaluation

Once the algorithm has assigned a cluster index to all the configurations of the decimated sample, the core-set analysis is performed. PAk provides the density (or, analogously, the free-energy) for all the points in the dataset. It is then possible to define a threshold for the free-energy, and include in every cluster $i$ just the data that differ in free-energy from the cluster center (minimum of the free-energy) less than the threshold value. In this way, the microstates are more reliable, since they contain just points around the minimum. The points that have been disregarded are later reassigned to the last core set visited, following the same procedure introduced in the previous chapter. In this way it is possible to avoid counting a lot of recrossings around the saddle-points of the free-energy, and to eliminate a big bias in the evaluation of the time scales of the dynamics.
As shown before in Figure 4.3, slip events are rapid and dramatic. From the simulations we noticed that slips are characterized by a rotation of the island, able to depin the slider from the surface and to give it the possibility to slip. These abrupt events push the island to rearrange in a new place far from the one visited before the slip event, and thus change completely its configuration. While "sticks" are long and easy to sample, "slips" are fast and poorly sampled. For this reason we have introduced an additional artificial microstate, that we will name "slip state": this allows to include a fundamental dynamical quantity as the center of mass velocity in the description of the microstates. Once the island experiences a slip event, in the dynamics between microstates, it enters the slip state. We assume that, once the system exits the slip state, it loses memory of the configuration visited before.
Once all the configurations have been assigned to a microstate, it is possible to build-up the

transition matrix, counting the jumps between clusters. Once normalized, the matrix $\Pi_{\alpha\beta}$ gives us the probability of the transition from cluster $\alpha$ to cluster $\beta$. Timescales can be found from $t_i = -\tau/\log(\lambda_i)$, where $\tau$ is the lag time between two successive configurations, and $\lambda_i$ are the eigenvalues of the transition matrix. Figure 4.11, at the top, shows the 4 slowest finite time scales as a function of the time lag $\tau$. For the finite time scales we find $\tau_2 \sim 800$ ps and $\tau_3 \sim 500$ ps. There is a gap between the first finite eigenvalue and the successive ones. On the bottom of Figure 4.11 we show the timescales for the chosen lag time $\tau = 150$ ps.

### 4.2.4 Observables

We analyze the $g_i$ functions (see Equation 3.3) of some relevant physical observables of this frictional system, in order to characterize the long-lived states we have identified. We stress that, as in the previous cases, the $g_i$ for $i \geq 1$ describe excitations on top of the steady state, and are defined regardless of a normalization constant and up to a sign. The study of the excited states highlights the slowest, therefore most important, deviations with respect to the steady-state distribution, associated with the slow relaxation times highlighted by our analysis.

#### In-plane strain

Even though not present in the definition of the metric, we can still study the deformation that the graphene is experiencing in the XY direction. These deformations are a consequence of the out of plane corrugation, that we are going to show later. In Figure 4.12, from the top to the bottom, we show the four excitations $g_i$, $i \geq 1$. The colored arrows represent the direction of the deformation, while the large black arrow shows the drag direction.
The steady-state probability is not shown. Indeed, as expected from the fact that the strain is computed regarding the average of all the configurations of the data set, the steady-state distribution must assume very small values that are very close to zero.
Interesting patterns appear looking at the excitations $g_i$. The first correction $g_1$ exhibits a dipole mode, in which the island is expanding with an evident symmetry axis that we have highlighted with a light green dashed line. This line is oriented 30°anticlockwise with respect to the drag direction (pointing up), and it identifies one of the main symmetry diagonals of the graphene flake. $g_2$ shows also a dipole compression, with a symmetry underlined by the dark-green dashed line rotated by 60°with respect to the one in $g_1$, and it corresponds to another symmetry diagonal of the slider. $g_3$ introduces a more complicated deformation: this time a quadrupole appears, with both an up-down and a right-left shear. The symmetry directions are both the one present in $g_1$ and the one present in $g_2$. Finally, $g_4$ shows an intricate deformation, with an expansion in the front, and a compression in the tail. The entire mode, is rotated 30°clockwise with respect to the drag direction.

#### Out-of-plane strain

Figure 4.13 show the difference from the average configuration in the Z direction. This strain is included in the metric. From the top to the bottom, we show: the steady state probability distribution and the corrections $g_i$, $i \geq 1$. We describe this quantity by a color map. Again, for every plot, the large black arrow shows the drag direction.
The excitations $g_i$, $i \geq 1$, must be compared with the ones for XY direction in Figure 4.12. The dipole expansion in $g_1$ is correlated with a left-right movement with respect to the drag direction (pointing up). One can imagine this mode as if the island was pivoting in order to proceed, lifting one “leg”, while leaving the other attached to the substrate. A similar movement is present in

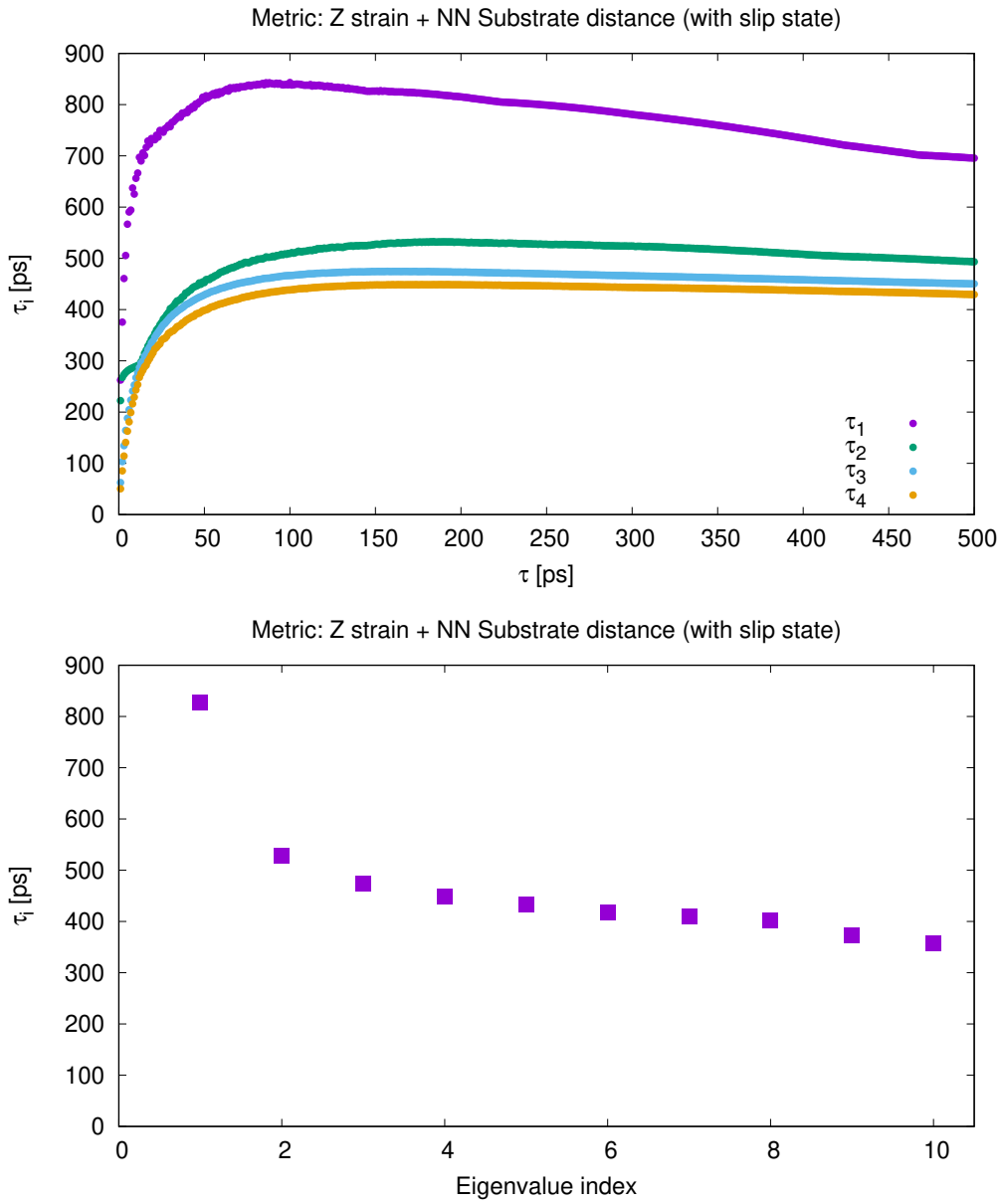


Figure 4.11: On the left, the first four excitation times as a function of the lag time $\tau$: a gap is present between the first and the other four time scales. On the right, the complete time-scale spectrum for the chosen lag time $\tau = 150$ ps.

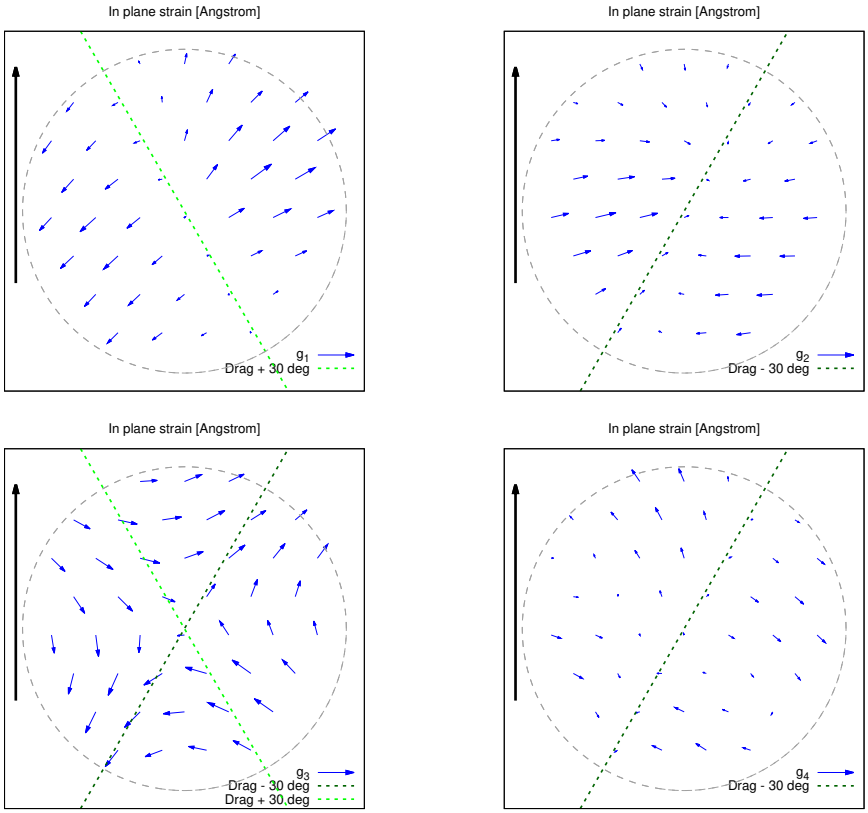


Figure 4.12: In-plane strain deformations, gaussian average over the points of the mesh shown in Figure 4.8. The steady-state is shown. Below, the first four excited-state corrections are shown. The arrow pointing up is indicating the drag direction of the tip, while the dashed light and dark-green lines underline the symmetry direction along which the strain deformation take place. Symmetries are the one typical of graphene.

$g_2$, for the Z coordinate; this time, however, the direction of the deformation perpendicular to the substrate coincides with the one in Figure 4.12 for $g_2$. The deformation $g_3$ exhibits again a dipolar behavior as $g_2$. Finally, the intricate movement described by $g_4$ is correlated to a depletion in the central/front part of the island, together with a detachment in the left and right lateral parts, and in the tail.

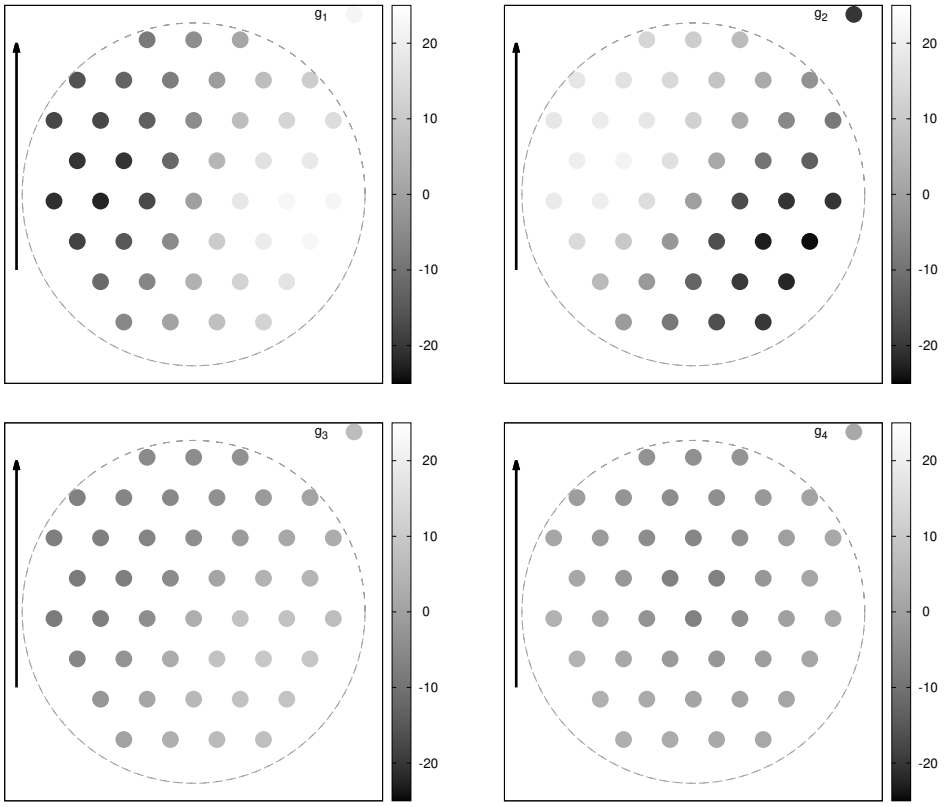


Figure 4.13: Out-of-plane strain deformations, gaussian average over the points of the mesh shown in Figure 4.8. The first four excited-state corrections to the steady-state are shown. The arrow pointing up is indicating the drag direction of the tip.

### Distance from nearest gold atom

We then consider the distance from the carbon atom to the closest gold atom of the substrate, another quantity included in the metric. This quantity gives us information regarding the interaction between the slider and the substrate. Differently from the strain, this quantity has not been computed from a difference to a reference configuration, but as an absolute value. From the top to the bottom, in Figure 4.14 we show the steady state probability distribution and the corrections $g_i$, $i \geq 1$. We describe this quantity with the same convention of Figure 4.13. For every plot, the large black arrow shows the drag direction.
The steady-state probability reflects the behavior of a finite island: the borders, less constrained from the harmonic interaction, are free to pin to the substrate and remain trapped. The center of the island, on the contrary, interacts less with the substrate and is more bound to the rest of the

flake. Note that the front border of the island is more attached to the substrate, as it is the one that encounters all the gold asperities in the first place. Finally, it is important to highlight that the range of the values of the carbon-gold distance in Figure 4.14, for the steady-state, exhibits variations of 1% maximum.
The corrections $g_i$ show more local variations for this quantity with respect to the ones regarding the strain. Probably this is due to the fact that the variance of this quantity is smaller with respect to the out-of-plane strain. For this reason, the strain plays the prevalent role in the metric. Anyway, in all the $g_i$ we can identify some areas, normally small and delimited, in which the island detaches from the substrate, hinting to a probable successive slip.

### 4.2.5 Conclusions and comments

We have shown in this chapter how a method developed for the study of a 1D Frenkel-Kontorova model is able to describe a realistic system made by a graphene island sliding on a rough gold substrate. This realistic system is clearly much more complicated than the one of our early analyses. For this reason, some expedients have been used.
In fact, the metric has not been defined using the raw positions of the atoms, but with two fundamental frictional quantities such as the strain and the distance between the graphene atoms and the substrate. The choice of these quantities is natural in a frictional environment. Moreover, the identification of a mesh to give a first coarse-graining has been dictated by the need to reduce the number of the degrees of freedom, but it could allow a first generalization of the description also in future applications.
It is always fundamental to describe a frictional dynamics in terms of slips, the crucial events in frictional sliding. However, the impossibility to include the velocity of the center of mass directly in the metric, together with the realization of the seismic behavior of our system, has lead us to the definition of an additional "motion state". The dynamics arrives in that state if a slip event occurs; once the system exits the slip state, it will have lost any memory of the configuration visited before. Another possible way would have been considering the slip or stick state as a further label to the $\sim 10$ states found from the clustering analysis, but this choice would have doubled the number of the microstates.
We have obtained roughly 10 states able to describe the motion of the island in terms of vibrations and oscillations, needed to navigate in the non-periodic gold landscape. We have discovered that the variations in the out-of-plane corrugation of the flake follow the symmetries of the graphene, and we have described how this off-plane excitation affect the in-plane disposition of the carbon atoms. We have been able to uncover the time scales of the movements concerning the island; the flake we have simulated has proven to be large enough to experience a macroscopic, non-local motion with low frequency, but not too large. With a really large island, in fact, the slow modes would have been characterized by far longer times, and our simulations would have been too short. A key issue has been the decimation of the data, caused by the inherent difficulty of sampling the phase space in the case of a non-periodic substrate like the one here simulated.
Warning the reader on the difficulties one may encounter in the analysis of a realistic model with our method, we describe how to overcome the problems it may encounter, and we suggest the use of the procedure developed for further investigations.

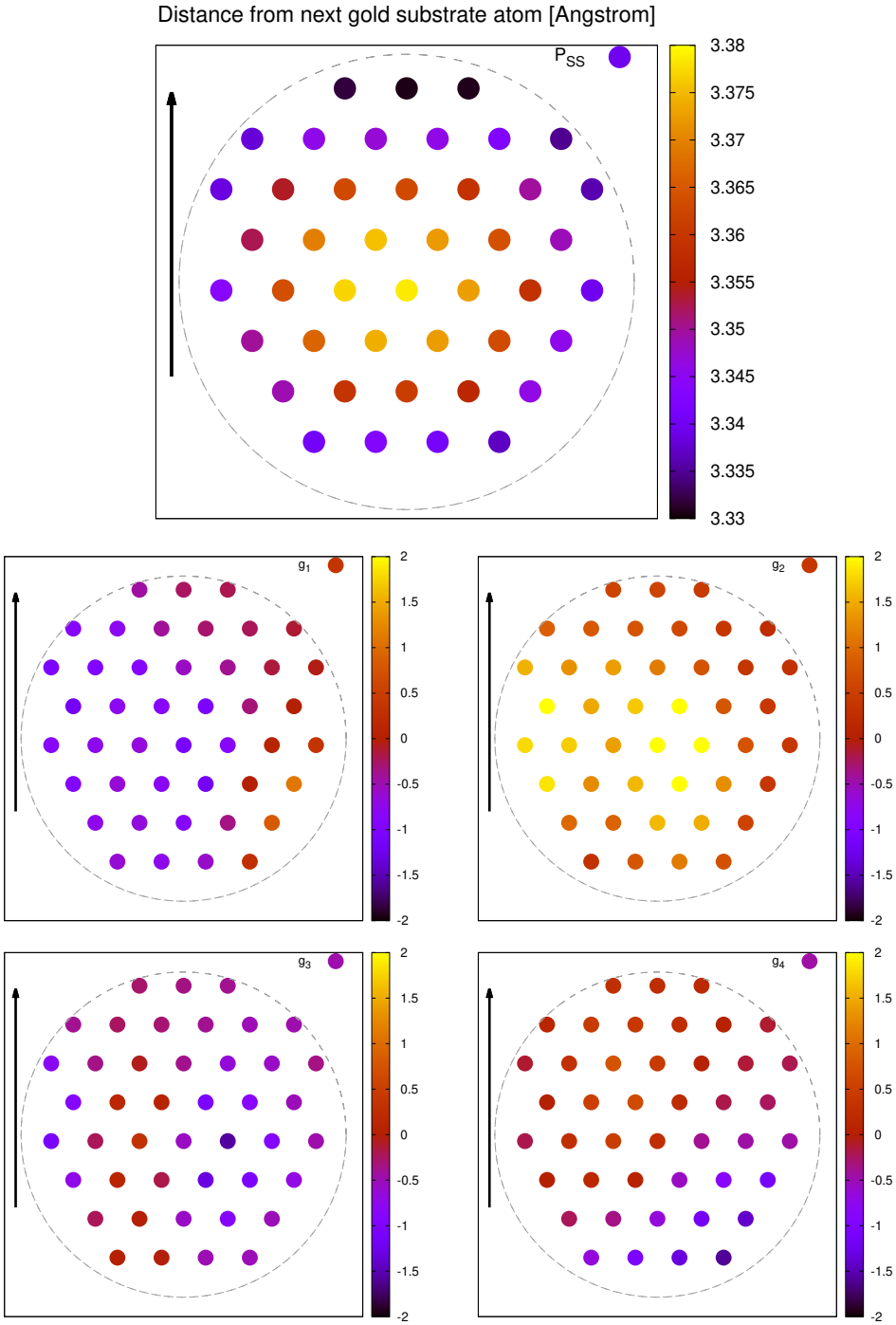


Figure 4.14: Distance from next gold substrate, gaussian average over the points of the mesh shown in Figure 4.8. On top, the steady-state is shown. Below, the first four excited-state corrections are shown. The arrow pointing up is indicating the drag direction of the tip.

# Conclusions

I have presented, discussed, and developed a statistically-based method for the study of the microscopic dynamics of frictional systems. It derives from the classical MSM, but with fundamental differences.
First, it analyzes non-equilibrium systems for which detailed balance does not hold. The resulting non-symmetric-ness of the probability transition matrix is fortunately known to be relatively weak. Second, the driving typical of frictional sliding implies a continuously growing phase space - making the required clustering in phase space additionally problematic. In this thesis work, this second difficulty was addressed with different strategies for the sliding on a periodic or a non-periodic substrate. In the first case, describing a 1D and mostly 2D Frenkel-Kontorova island sliding on a periodic potential, I adopted a metric in which the positions of the particles have been considered modulo 2 substrate lattice spacings, taking advantage of the substrate periodicity. In the second, and more realistic case represented by the sliding of a 2D graphene island on a randomly roughened gold surface I have identified a slip event as the point in which the system loses memory of the preceding dynamics.
A fundamental and to a large extent arbitrary choice for all the different applications of MSM of sliding friction described by the MSM method developed in this thesis has been the definition of the phase space metric. The metric defines the distance of two configurations in phase space, crucial to measure the similarity between them. One must strive to use the less prejudiced metric possible: for periodic systems, this choice is satisfied with the description of the configurations in terms of particle positions. For the non-periodic system of the graphene slider on a rough substrate of gold, a similar choice is impossible. Here, the metric includes the coordinates of the atoms via frictional quantities like the corrugation of the flake or the distance between gold and carbon atoms. In principle, the extended phase space including particle velocities as well as positions should also be considered. Simply in order to avoid the resulting phase space doubling, this was provisionally avoided by isolating slip events, where velocity is temporarily very large, in a separate artificial category.
A key role in our method is represented by the phase space coarse-graining algorithm. The first version of MSM of sliding friction employed DP clustering [47], with a large number of microstates and the necessity of a further reduction of their number using special techniques like PCCA+. I used instead the more recent *unsupervised* and *non-parametric* PAk method [46], which is able to recognize the main minima of free energy. It has improved and speeded up the analysis, helping the automatic recognition of a manageably small number of relevant Markov states.
The same method has been able to describe correctly the 1D and 2D FK model systems, as well as the realistic graphene flake sliding on the rough gold surface.
Finally, the main outcome of this thesis is to provide, starting from a well-sampled steady-state sliding simulation, a relatively unbiased and quantitative description of the slowest excitations – in the form of transition matrix eigenstates and eigenvectors – which represent the slowest and dominant phenomena dominating the steady-state frictional evolution. Based on these ingredients,

the time evolution of diverse physical quantities – of which we describe only a few – will be feasible *a posteriori*.

# Bibliography


[1] LAMMPS molecular dynamics simulator, 1995.

[2] G. D. Archard. Back scattering of electrons. *Journal of Applied Physics*, 32(8):1505–1509, 1961.

[3] J. F. Archard and Thomas Edward Allibone. Elastic deformation and the laws of friction. *Proceedings of the Royal Society of London. Series A. Mathematical and Physical Sciences*, 243(1233):190–205, 1957.

[4] G. Binnig, C. F. Quate, and Ch. Gerber. Atomic force microscope. *Phys. Rev. Lett.*, 56:930–933, Mar 1986.

[5] Frank Philip Bowden and David Tabor. *The friction and lubrication of solids*. Oxford : Clarendon Press, 1950. Vol. 1 reprinted from corrected sheets.

[6] Oleg M. Braun and Yuri Kivshar. *The Frenkel-Kontorova Model*. Springer-Verlag Berlin Heidelberg, 2004.

[7] Donald W Brenner, Olga A Shenderova, Judith A Harrison, Steven J Stuart, Boris Ni, and Susan B Sinnott. A second-generation reactive empirical bond order (REBO) potential energy expression for hydrocarbons. *Journal of Physics: Condensed Matter*, 14(4):783–802, jan 2002.

[8] G.A. Tomlinson B.Sc. Cvi. a molecular theory of friction. *The London, Edinburgh, and Dublin Philosophical Magazine and Journal of Science*, 7(46):905–939, 1929.

[9] R. Burridge and L. Knopoff. Model and theoretical seismicity. *Bulletin of the Seismological Society of America*, 57(3):341–371, 06 1967.

[10] Muller V.M Derjaguin, B.V and Yu.P Toporov. Effect of contact deformations on the adhesion of particles. *Journal of Colloid and Interface Science*, 53:314–326, 1975.

[11] Maria d'Errico, Elena Facco, Alessandro Laio, and Alex Rodriguez. Automatic topography of high-dimensional data sets by non-parametric density peak clustering. *arXiv e-prints*, page arXiv:1802.10549, Feb 2018.

[12] Peter Deuflhard and Marcus Weber. Robust perron cluster analysis in conformation dynamics. *Linear Algebra and its Applications*, 398:161 – 184, 2005. Special Issue on Matrices and Mathematical Biology.

[13] Ali Erdemir and Jean-Michel Martin, editors. *Superlubricity*. Elsevier Science B.V., 2007.

[14] E. Facco, M. d'Errico, A. Rodriguez, and A. Laio. Estimating the intrinsic dimension of datasets by a minimal neighborhood information. *Scientific Reports*, 7:2045–2322, 2017.

[15] Karl Pearson F.R.S. Liii. on lines and planes of closest fit to systems of points in space. *The London, Edinburgh, and Dublin Philosophical Magazine and Journal of Science*, 2(11):559–572, 1901.

[16] Peter Grassberger and Itamar Procaccia. Characterization of strange attractors. *Phys. Rev. Lett.*, 50:346–349, Jan 1983.

[17] J. A. Greenwood, J. B. P. Williamson, and Frank Philip Bowden. Contact of nominally flat surfaces. *Proceedings of the Royal Society of London. Series A. Mathematical and Physical Sciences*, 295(1442):300–319, 1966.

[18] R. Guerra, U. Tartaglino, A. Vanossi, and E. Tosatti. Ballistic nanofriction. *Nature Materials*, 9(634), 2010.

[19] B. Gutenberg and C. F. Richter. Earthquake magnitude, intensity, energy, and acceleration. *Bulletin of the Seismological Society of America*, 32(3):163–191, 1942.

[20] B. Gutenberg and C.F. Richter. Earthquake magnitude, intensity, energy, and acceleration. *Bulletin of the Seismological Society of America*, 46:105–146, 1956.

[21] Heinrich Hertz. Ueber die berührung fester elastischer körper. *Journal für die reine und angewandte Mathematik (Crelle's Journal)*, 1882:156–171, 1882.

[22] Jacob N. Israelachvili. Adhesion forces between surfaces in liquids and condensable vapours. *Surface Science Reports*, 14(3):109 – 159, 1992.

[23] Jacob N. Israelichvili, Patricia M. MCGuiggan, and Andrew M. Homola. Dynamic properties of molecularly thin liquid films. *Science*, 240(4849):189–191, 1988.

[24] Kenneth Langstreth Johnson, Kevin Kendall, A. D. Roberts, and David Tabor. Surface energy and the contact of elastic solids. *Proceedings of the Royal Society of London. A. Mathematical and Physical Sciences*, 324(1558):301–313, 1971.

[25] J. C. Kaplan and J. A. Yorke. Functional differential equations and approximations of fixed points. *Lecture Notes in Mathematics, Springer, Berlin*, 730, 1979.

[26] Fabian Knoch and Thomas Speck. Cycle representatives for the coarse-graining of systems driven into a non-equilibrium steady state. *New Journal of Physics*, 17(11):115004, nov 2015.

[27] T. Kontorova and J. Frenkel. On the theory of plastic deformation and twinning. *Izv. Akad. Nauk, Ser. Fiz.*, 1:137–149, 1939.

[28] J. Krim and A. Widom. Damping of a crystal oscillator by an adsorbed monolayer and its relation to interfacial viscosity. *Phys. Rev. B*, 38:12184–12189, Dec 1988.

[29] M. Kuwabara, D. R. Clarke, and D. A. Smith. Anomalous superperiodicity in scanning tunneling microscope images of graphite. *Applied Physics Letters*, 56(24):2396–2398, 1990.

[30] R.S. Bradley M.A. Lxxix. the cohesive force between solid surfaces and the surface energy of solids. *The London, Edinburgh, and Dublin Philosophical Magazine and Journal of Science*, 13(86):853–862, 1932.

[31] J. B. MacQueen. Some methods for classification and analysis of multivariate observations. In L. M. Le Cam and J. Neyman, editors, *Proc. of the fifth Berkeley Symposium on Mathematical Statistics and Probability*, volume 1, pages 281–297. University of California Press, 1967.

[32] J. B. MacQueen. *Groups in Data: An Introduction to Cluster Analysis*, volume 344. Wiley-Interscience, 2009.

[33] D. Mandelli, A. Vanossi, M. Invernizzi, S. Paronuzzi, N. Manini, and E. Tosatti. Superlubric-pinned transition in sliding incommensurate colloidal monolayers. *Phys. Rev. B*, 92:134306, Oct 2015.

[34] Daniel Maugis. Adhesion of spheres: The jkr-dmt transition using a dugdale model. *Journal of Colloid and Interface Science*, 150(1):243 – 269, 1992.

[35] E Meyer, T Gyalog, R M Overney, and K Dransfeld. *Nanoscience: Friction and Rheology on the Nanometer Scale*. WORLD SCIENTIFIC, 1998.

[36] Martin H. Müser, Wolf B. Dapp, Romain Bugnicourt, Philippe Sainsot, Nicolas Lesaffre, Ton A. Lubrecht, Bo N. J. Persson, Kathryn Harris, Alexander Bennett, Kyle Schulze, Sean Rohde, Peter Ifju, W. Gregory Sawyer, Thomas Angelini, Hossein Ashtari Esfahani, Mahmoud Kadkhodaei, Saleh Akbarzadeh, Jiunn-Jong Wu, Georg Vorlaufer, András Vernes, Soheil Solhjoo, Antonis I. Vakis, Robert L. Jackson, Yang Xu, Jeffrey Streator, Amir Rostami, Daniele Dini, Simon Medina, Giuseppe Carbone, Francesco Bottiglione, Luciano Afferrante, Joseph Monti, Lars Pastewka, Mark O. Robbins, and James A. Greenwood. Meeting the contact-mechanics challenge. *Tribology Letters*, 65(4):118, Aug 2017.

[37] Vijay S. Pande, Kyle Beauchamp, and Gregory R. Bowman. Everything you wanted to know about markov state models but were afraid to ask. *Methods*, 52(1):99 – 105, 2010. Protein Folding.

[38] F. Pellegrini, François P. Landes, A. Laio, S. Prestipino, and E. Tosatti. Markov state modeling of sliding friction. *Phys. Rev. E*, 94:053001, Nov 2016.

[39] B. N. J. Persson. Elastoplastic contact between randomly rough surfaces. *Phys. Rev. Lett.*, 87:116101, Aug 2001.

[40] B. N. J. Persson. On the fractal dimension of rough surfaces. *Tribology Letters*, 54(1):99–106, Apr 2014.

[41] Bo Persson. *Sliding Friction*. Springer-Verlag Berlin Heidelberg, 2000.

[42] M Peyrard and S Aubry. Critical behaviour at the transition by breaking of analyticity in the discrete frenkel-kontorova model. *Journal of Physics C: Solid State Physics*, 16(9):1593–1608, mar 1983.

[43] Steve Plimpton. Fast parallel algorithms for short-range molecular dynamics. *Journal of Computational Physics*, 117(1):1 – 19, 1995.

[44] L. Prandtl. Ein gedankenmodell zur kinetischen theorie der festen körper. *ZAMM - Journal of Applied Mathematics and Mechanics / Zeitschrift für Angewandte Mathematik und Mechanik*, 8(2):85–106, 1928.

[45] Jan-Hendrik Prinz, Hao Wu, Marco Sarich, Bettina Keller, Martin Senne, Martin Held, John D. Chodera, Christof Schütte, and Frank Noé. Markov models of molecular kinetics: Generation and validation. *The Journal of Chemical Physics*, 134(17):174105, 2011.

[46] A. Rodriguez, M. d'Errico, E. Facco, and A. Laio. Computing the free energy without collective variables. *Journal of Chemical Theory and Computation*, 0(0):null, 0. PMID: 29401379.

[47] A. Rodriguez and A. Laio. Clustering by fast search and find of density peaks. *Science*, 344(6191):1492–1496, 2014.

[48] Daniel Sheppard, Rye Terrell, and Graeme Henkelman. Optimization methods for finding minimum energy paths. *The Journal of Chemical Physics*, 128(13):134106, 2008.

[49] Steven J. Stuart, Alan B. Tutein, and Judith A. Harrison. A reactive potential for hydrocarbons with intermolecular interactions. *The Journal of Chemical Physics*, 112(14):6472–6486, 2000.

[50] M. Teruzzi, F. Pellegrini, A. Laio, and E. Tosatti. A markov state modeling analysis of sliding dynamics of a 2d model. *The Journal of Chemical Physics*, 147(15):152721, 2017.

[51] Søren Toxvaerd and Jeppe C. Dyre. Communication: Shifted forces in molecular dynamics. *The Journal of Chemical Physics*, 134(8):081102, 2011.

[52] A Vanossi and O M Braun. Driven dynamics of simplified tribological models. *Journal of Physics: Condensed Matter*, 19(30):305017, jul 2007.

[53] A. Vanossi, J. Röder, A. R. Bishop, and V. Bortolani. Underdamped commensurate dynamics in a driven frenkel-kontorova–type model. *Phys. Rev. E*, 67:016605, Jan 2003.

[54] Andrea Vanossi, Nicola Manini, Michael Urbakh, Stefano Zapperi, and Erio Tosatti. *Colloquium*: Modeling friction: From nanoscale to mesoscale. *Rev. Mod. Phys.*, 85:529–552, Apr 2013.

[55] Han Wang and Christof Schütte. Building markov state models for periodically driven non-equilibrium systems. *Journal of Chemical Theory and Computation*, 11:1819–1831, Apr 2015.

[56] Marcus Weber and Susanna Kube. Robust perron cluster analysis for various applications in computational life science. In Michael R. Berthold, Robert C. Glen, Kay Diederichs, Oliver Kohlbacher, and Ingrid Fischer, editors, *Computational Life Sciences*, pages 57–66. Springer Berlin Heidelberg, 2005.

[57] David J. Whitehouse, J. F. Archard, and David Tabor. The properties of random surfaces of significance in their contact. *Proceedings of the Royal Society of London. A. Mathematical and Physical Sciences*, 316(1524):97–121, 1970.